

**An extended variational atmospheric  
chemistry data assimilation system for  
combined space and air borne  
trace gas retrievals**

I n a u g u r a l – D i s s e r t a t i o n  
zur  
Erlangung des Doktorgrades  
der Mathematisch–Naturwissenschaftlichen Fakultät  
der Universität zu Köln

vorgelegt von  
Ketevan Kasradze  
aus Tbilisi

Köln 2016

Berichterstatter: PD Dr. H. Elbern  
Prof. Dr. A. Wahner

Tag der mündlichen Prüfung: 28.06.2016

## Abstract

A four-dimensional variational data assimilation system for stratospheric trace gas observations has been extended and evaluated to draw full advantage from stratospheric remote sounding data and upper troposphere lower stratosphere (UTLS) in-situ aircraft measurements. The UTLS is the transition layer between the stratosphere and the troposphere and is marked by strong spatial and temporal variability of dynamic structures and distribution of trace gases. Aircraft measurements, highly resolving the UTLS filamental structures, are of most interest for local studies. Although, the satellite instruments are delivering an unprecedented wealth of observations of a number of stratospheric trace gases with global coverage, they are scattered and have a limited resolution in space or time. Combining these measurements and applying advanced data assimilation techniques to compare benefits from satellite and air borne data, and to analyse the chemical composition of the tropopause and lower stratosphere, was the issue of this work. For this purpose, a model grid refinement and full revision of the chemical mechanism were performed. The resolution of the horizontal grid points was increased from about 240 km to 150 km, resulting in 23 042 grid points per model level. The vertical resolution was increased with twelve additional layers, especially in the UTLS region. Hence, the vertical separation between grid levels is now less than 1 km below 22 km altitude. The chemistry module was extended and revised to better represent chemical processes in the UTLS region. All reaction rates were updated according to the recommendations of the NASA's Jet Propulsion Laboratory. In total, a number of 197 photolysis, gas phase, and heterogeneous reactions of 51 stratospheric trace gases is considered by the chemistry module now. The meteorological fields are computed online by the global forecast model GME of German Weather Service. A comprehensive set of case studies has been conducted in order to test and evaluate the extended system. Retrievals of various stratospheric trace gases derived from measurements of the Earth Observing System Microwave Limb Sounder, as well as retrievals of aircraft measurements have been assimilated. The analyses show a perfect performance with respect to the assimilated ozone observations. For assimilation of water observations in UTLS additional preconditioning issue is desirable. Comparison with independent observations from satellite instruments and radiosondes demonstrates a very good performance of the extended assimilation system.

## Kurzzusammenfassung

Ein System zur Assimilation stratosphärischer Spurengasmessungen basierend auf der vierdimensionalen variationellen Methode wurde erweitert und validiert. Dies wurde durchgeführt um die Vorteile stratosphärischer Fernerkundungsdaten und in-situ Flugzeugmessungen in der oberen Troposphäre und der unteren Stratosphäre (UTLS) zu vereinen. Die UTLS ist die Übergangsschicht zwischen der Stratosphäre und der Troposphäre und wird durch starke räumliche und zeitliche Variabilität der dynamischen Strukturen gekennzeichnet. Flugzeugmessungen können die filamentäre Strukturen in der UTLS auflösen und sind für lokale Studien von besonderem Interesse. Obwohl Satelliteninstrumente eine große Anzahl an Beobachtungen von Spurengasen in der gesamten Stratosphäre liefern, haben sie nur begrenzte Auflösung in Raum oder Zeit. Dieser Beobachtungen zu kombinieren und erweiterte Datenassimilationstechniken anzuwenden, um die chemische Zusammensetzung der Tropopause und der unteren Stratosphäre zu analysieren, ist das Hauptziel dieser Arbeit. Zu diesem Zweck wurde das Modellgitter verfeinert und der chemische Mechanismus vollständig überarbeitet. Die horizontale Auflösung wurde von etwa 240 km auf 150 km erhöht und resultiert in 23 042 Gitterpunkten pro Modellebene. Die vertikale Auflösung wurde um zusätzliche zwölf Schichten erhöht, insbesondere in der UTLS Region. Die vertikale Ausdehnung einzelner Schichten ist dadurch kleiner als 1 km unterhalb von 22 km Höhe. Das neue Chemiemodul berücksichtigt 197 Photolyse-, Gasphasen- und heterogene Reaktionen zwischen 51 stratosphärischen Spurengasen. Die meteorologischen Felder werden mit Hilfe des globalen Wettervorhersagemodells GME des Deutschen Wetterdienstes direkt erzeugt. Die Leistung des neu erweiterten vierdimensionalen variationellen Datenassimilationsystems wurde mit Fallstudien validiert. Dazu wurden Spurengasprofile, abgeleitet aus Messungen des "Earth Observing System Microwave Limb Sounder" sowie Beobachtungen von Flugzeugmessungen wurden assimiliert. Die Analysen zeigen eine perfekte Übereinstimmung mit assimilierten Ozonbeobachtungen. Für die assimilation von Wasserbeobachtungen in der UTLS eine zusätzliche Präkonditionierung vorzuziehen. Der Vergleich mit unabhängigen Beobachtungen von Satelliteninstrumenten und Radiosonden demonstriert eine sehr gute Leistung des erweiterten Assimilationsystems.

---

## Contents

---

<b>1</b>	<b>Introduction</b>	<b>1</b>
<b>2</b>	<b>Data assimilation</b>	<b>5</b>
2.1	Bayes' theorem . . . . .	5
2.2	Maximum likelihood and minimum variance . . . . .	6
2.3	Four-dimensional variational data assimilation . . . . .	7
2.3.1	Adjoint model technique . . . . .	9
<b>3</b>	<b>The SACADA assimilation system</b>	<b>11</b>
3.1	The SACADA model . . . . .	12
3.2	Chemistry transport module . . . . .	13
3.3	The adjoint model . . . . .	15
3.4	Meteorological module, grid configuration and parallelization . .	16
<b>4</b>	<b>Background error covariance modeling</b>	<b>21</b>
4.1	Incremental formulation of the cost function . . . . .	22
4.2	Correlation modelling with diffusion approach . . . . .	23
4.3	Current setup . . . . .	24
<b>5</b>	<b>Observational Basis</b>	<b>27</b>
5.1	CRISTA-NF . . . . .	27

---

5.2	MLS . . . . .	29
5.3	MIPAS-IMK . . . . .	30
5.4	HALOE . . . . .	31
5.5	Atmospheric soundings . . . . .	32
5.6	Observation Operator . . . . .	32
<b>6</b>	<b>Campaign Simulations</b>	<b>35</b>
6.1	SCOUT-O3 Tropical Aircraft Campaign . . . . .	35
6.2	SCOUT-AMMA Campaign . . . . .	37
6.2.1	West African Monsoon . . . . .	38
6.3	System set-up . . . . .	40
6.4	General results with $\chi^2$ -tests . . . . .	42
6.5	The Campaign Analysis . . . . .	46
6.5.1	Introduction to $H_2O$ , $O_3$ and $HNO_3$ . . . . .	46
6.5.2	The SCOUT-O3 Campaign . . . . .	47
6.5.3	The SCOUT-AMMA Campaign . . . . .	57
<b>7</b>	<b>Summary and Conclusions</b>	<b>69</b>
<b>A</b>	<b>Tables</b>	<b>73</b>
A.1	Vertical grid parameters . . . . .	73
A.2	Reaction equations . . . . .	76
	<b>Acknowledgements</b>	<b>91</b>

---

## List of Figures

---

3.1	Icosahedral grid vs. latitude-longitude grid . . . . .	16
3.2	Geometry of grid cells in the icosahedral grid . . . . .	17
3.3	Pressure and height of SACADA model layers . . . . .	19
3.4	Domain decomposition and parallel speed-up . . . . .	19
5.1	CRISTA-NF on board of Geophysica . . . . .	28
5.2	The limb sounding technique by CRISTA-NF . . . . .	28
5.3	EOS MLS on AURA . . . . .	29
5.4	The limb sounding technique by MLS . . . . .	30
5.5	The limb sounding technique by MIPAS . . . . .	31
5.6	Atmospheric sounding . . . . .	32
6.1	SCOUT-O3 Tropical Aircraft Campaign route . . . . .	36
6.2	SCOUT-AMMA Campaign route . . . . .	38
6.3	West African Monsoon . . . . .	39
6.4	The cost function evolution, case SCOUT-O3-1 . . . . .	42
6.5	The cost function evolution, case SCOUT-AMMA-3 . . . . .	43
6.6	The cost function evolution, case SCOUT-AMMA-2 . . . . .	44
6.7	SCOUT-O3-2 mean CRISTA-NF $H_2O$ profiles . . . . .	48
6.8	SCOUT-O3-2 mean MLS $H_2O$ profiles . . . . .	49

6.9	SCOUT-O3-2 mean MLS $O_3$ profiles . . . . .	50
6.10	SCOUT-O3-2 mean MLS $HNO_3$ profiles . . . . .	51
6.11	SCOUT-O3-2 mean HALOE $H_2O$ profiles . . . . .	52
6.12	SCOUT-O3-2 mean HALOE $O_3$ profiles . . . . .	52
6.13	SCOUT-O3-1 mean MIPAS-IMK $H_2O$ profiles . . . . .	53
6.14	North-south cross-sections of the zonal wind $u$ component. . . . .	54
6.15	MLS $H_2O$ analysis and control run for 4 November 2005 . . . . .	55
6.16	CRISTA-NF $H_2O$ analysis increment and observations for 4 November 2005 . . . . .	55
6.17	MLS $O_3$ analysis and observations for 4 November 2005 . . . . .	56
6.18	SCOUT-AMMA-3 CRISTA-NF $H_2O$ Profiles along the flight route . . . . .	57
6.19	SCOUT-AMMA-3 CRISTA-NF $O_3$ Profiles along the flight route . . . . .	58
6.20	SCOUT-AMMA-2 mean CRISTA-NF $H_2O$ profiles . . . . .	59
6.21	SCOUT-AMMA-3 mean CRISTA-NF $O_3$ profiles . . . . .	60
6.22	SCOUT-AMMA-2 mean MLS $H_2O$ profiles . . . . .	61
6.23	SCOUT-AMMA-3 mean MLS $O_3$ profiles . . . . .	62
6.24	SCOUT-AMMA-3 mean MLS $HNO_3$ profiles . . . . .	63
6.25	SCOUT-AMMA-3 mean CRISTA-NF $HNO_3$ profiles . . . . .	64
6.26	Zonal wind for 13 August 2006 . . . . .	65
6.27	CRISTA-NF $H_2O$ analysis increment and observations for 13 August 2006 . . . . .	65
6.28	MLS $H_2O$ analysis increment and observations for 13 August 2006 . . . . .	66
6.29	$H_2O$ analysis for 13 August 2006 . . . . .	66
6.30	SCOUT-AMMA-2 CRISTA-NF $H_2O$ profiles from 29 July 2006 . . . . .	67
6.31	SCOUT-AMMA-2 CRISTA-NF $H_2O$ profiles from 1 August 2006 . . . . .	68

---

## List of Tables

---

5.1	List of the radiosonde stations used in this work . . . . .	33
6.1	SCOUT-O3 Campaign flights . . . . .	37
6.2	SCOUT-AMMA Campaign flights . . . . .	38
6.3	BECM parameter settings. . . . .	40
6.4	The system set-ups for different test cases. . . . .	40
A.1	Coefficients defining the vertical grid . . . . .	73
A.2	Photolysis reactions included in the model CHEM51 . . . . .	76
A.3	Gas phase reactions included in the model CHEM51 . . . . .	77
A.4	Heterogeneous reactions included in the model CHEM51 . . . . .	81



# CHAPTER 1

---

## Introduction

---

Chemical weather forecasting (CWF) - a new field of atmospheric modelling - quickly developing and growing (*Lawrence et al.* [2005]). Many experimental studies (*Rosenfeld* [2000]; *Lohmann and Feichter* [2005]; *Ramanathan and Feng* [2009]) and numerical research simulations (*Jacobson* [2002]; *Grell et al.* [2004]) show that atmospheric processes (meteorological weather, including the precipitation, thunderstorms, radiation budget) depend on concentrations of chemical components in the atmosphere. CWF is closely related to the numerical weather prediction (NWP). The provision of all initial state conditions for model is crucial, in order to obtain a skillful numerical forecast (*Elbern et al.* [2000]). For this purpose, NWP uses sets of sparse and spatially scattered weather observations to derive an *objective analysis* or *data assimilation* of the atmospheric state on model grids (*Daley* [1993]). According to *Talagrand* [1997], the term *data assimilation* means "using all the available information, to determine as accurately as possible the state of the atmospheric (or oceanic) flow." Thus, numerical model can promote valuable information to the analysis process, as it contains the fundamental physical laws of the atmospheric flow.

Stratospheric processes and their role in climate became more important for understanding the earth system research in recent past. The discovery of the ozone hole in the 1980s (*Solomon* [1988]) and its impact on human health (*McMichael and Woodruff* [2005]) led to additional interest in studying the interaction complexity between chemistry, radiation, and dynamics within the

stratosphere. Further, the stratosphere holds the signature of anthropogenic forcing through the processes related to ozone depletion and increased greenhouse gas concentration (*Dall'Amico et al.* [2010]). In recent years, there has been increasing evidence that the stratosphere can influence tropospheric climate from the tropopause down to the surface (*Baldwin and Dunkerton* [1999]; *Thompson and Solomon* [2002]).

Until the eighties only sparse observational data was available in stratosphere. With the advent of space borne remote sounding devices, information about stratospheric trace gases can be retrieved from emitted, scattered, or transmitted radiation, which is recorded by these instruments. Presently, these instruments are delivering an unprecedented wealth of observations of a number of stratospheric trace gases with global coverage. Among them is the Earth Observing System (EOS) Microwave Limb Sounder (MLS), an instrument on the NASA's EOS Aura satellite, launched in July 2004 (*Waters et al.* [2004]). In March 2002 the European research satellite ENVISAT was launched into a polar orbit carrying the Michelson Interferometer for Passive Atmospheric Sounding (MIPAS) aboard (*Fischer et al.* [2008]). Since January 2005, MIPAS is providing measurements at a reduced spectral resolution (*von Clarmann et al.* [2009]). On board of the Upper Atmosphere Research Satellite (UARS) the Halogen Occultation Experiment (HALOE) was providing a long term records of important stratospheric constituents in period from October 1991 to November 2005 (*Nazaryan et al.* [2005]).

The Upper Troposphere Lower Stratosphere (UTLS) is the transition layer between the stratosphere and the troposphere and is important for the trace gas exchange (*Holton et al.* [1995]). The UTLS area is marked by a strong spatial and temporal variability of the dynamic structures, often organized as filaments (*Mahlman* [1997]). This variability is controlled by transport and chemical transformation processes of trace gas distribution in this region (*Riese et al.* [2012]). In particular the modeling of water vapor in the UTLS is problematic, due to extremely strong gradient of the water vapor concentration there (*Dee and Da Silva* [2003]). Despite all, UTLS region is still sparsely covered by in situ measurements and not well resolved by satellite observations (*Randel and Jensen* [2013]).

The Cryogenic Infrared Spectrometers and Telescope for the Atmosphere -New Frontiers (CRISTA-NF) is an instrument developed in cooperation by Institute of Energy and Climate Research - Stratosphere, Research Centre Julich (IEK-7) and University of Wuppertal. It is based on the satellite instrument CRISTA developed for studies of small-scale structures in atmospheric trace gas distributions. CRISTA participated in two Space Shuttle flights in November 1994 and August 1997 (*Offermann et al.* [1999]). Later, the center telescope of

---

CRISTA was adapted for use in the high-flying Russian research aircraft M55 Geophysica (*Stefanutti et al.* [1999]) and was termed CRISTA-NF (*Schroeder et al.* [2009]). Whereas the satellite observations are scattered and have a limited resolution in space or time, the aircraft measurements, highly resolving and well suited for UTLS filamental structures, are of most interest for local studies. Two measurement campaigns, with CRISTA-NF on board of M55 Geophysica, took place within the remote sensing experiments: SCOUT-O3 and SCOUT-AMMA, over the periods November-December 2005 and July-August 2006 (*Hoffmann et al.* [2009]; *Weigel et al.* [2010]; *Cairo et al.* [2010]). SCOUT-O3 was a measurement campaign in Darwin to study the transport of trace gases with high spatial resolution through the Tropical Tropopause Layer (TTL) (*Hoffmann et al.* [2009]). SCOUT-AMMA was a measurement campaign in west Africa with main objective to better document specific dynamical and chemical processes and weather systems at various key stages of the monsoon season in TTL (*Janicot et al.* [2008]).

The state of the art aircraft instrument is the Gimballed Limb Observer for Radiance Imaging of the Atmosphere (GLORIA) (*Riese et al.* [2014]). While CRISTA-NF looks from the starboard side of the aircraft in a limb viewing mode, GLORIA is designed to provide information by two- and three-dimensional observations with higher spatial resolution.

The observations, by nature, are scattered in space and time, while most applications require spatially and temporally uniform and consistent fields of atmospheric constituents. Among these applications are operational weather forecasting (*Geer et al.* [2006]), ozone forecasting (*Eskes et al.* [2004]), process studies (*Hoffmann and Riese* [2004]), and initialization of climate models. Applying the advanced data assimilation techniques (*Kalnay* [2003]), draws full advantage from stratospheric remote sounding data and UTLS in situ measurements.

The constituent data assimilation is less mature than meteorological data assimilation (*Lahoz and Errera* [2010]). Similar to NWP, stratospheric CWF is primarily an initial value problem, although the sources and sinks of chemical constituents have to be considered. Chemical equation systems are stiff, as a consequence of reaction rates, that vary by several orders of magnitude. This leads to strong error correlations between the species and can cause error covariance matrices to become singular (*Lahoz et al.* [2007]). Thus, sophisticated numerical solvers, called stiff solvers, have to be used. The dimensionality of stratospheric CWF models is much higher than that of the NWP models. Whereas the NWP models use under a dozen variables, the CWF model can have up to 100 different species, *i.e.*, variables per grid point. This can result in univariate background error covariance matrix of size  $10^{10}$ , where the correct

parametrisation has to be applied (*Elbern et al.* [2010])

Synoptic Analysis of Chemical constituents by Advanced Data Assimilation (SACADA) is a four-dimensional variational (4D-Var) assimilation system developed for estimation of transport and chemical transformation of atmospheric trace gases in stratosphere (*Elbern et al.* [2010]). A key issue of this work was to adapt the SACADA assimilation system for the assimilation of high resolution aircraft measurements. Model grid refinement, full revision and extension of chemical mechanism was therefore performed.

The main objectives of this thesis addresses the following questions:

1. What is the added value of assimilation of aircraft data compared to satellite data in UTLS region?
2. How performs data assimilation to the analysis and day prediction improvement?
3. Is the resolution of SACADA assimilation system sufficient to assimilate aircraft data?

This thesis is organized as follows: The theory of chemical data assimilation is presented in chapter 2. The SACADA assimilation system, with its main components is described in chapter 3. The chapter 4 include theory and current setup of the BECM. A comprehensive set of case studies has been accomplished to evaluate and test the SACADA assimilation system. Profiles of various stratospheric trace gases derived from EOS MLS spectra as well as profiles of aircraft measurements from CRISTA-NF have been assimilated. Observational data from the HALOE and MIPAS-IMK satellite instruments and radiosondes served as an independent control data sets. Chapter 5 provides an overview of these instruments and the respective data products. The results are presented in Chapter 6. A summary of the present work as well as the final conclusions are given in Chapter 7.

## CHAPTER 2

---

### Data assimilation

---

The main goal of data assimilation is coupling of the observed information with our theoretical knowledge as given by models, to obtain most probable system state at a given time. In meteorology, for instance, it is important to have an optimal state estimation of the atmosphere and evolution for improved forecasts. Since probability theory is one of the guiding basis for the data assimilation, a short description is presented here.

### 2.1 Bayes' theorem

Assume that a probability density function (PDF)  $p(x)$ ,  $p : \mathbb{R}^n \rightarrow \mathbb{R}$  of the discrete approximation of the atmospheric state  $x$  is available, called *a priori* probability. In addition information provided by the observations  $y \in \mathbb{R}^p$  are given with the error characteristics. Thus, it is possible to formulate a PDF  $p(y|x)$ , which describes the probability of taking  $y$  measurements under a given atmospheric state  $x$ . Then the *a posteriori* PDF  $p(x|y)$  can be derived by Bayes' theorem as follows:

$$p(x|y) = \frac{p(y|x)p(x)}{\int p(y|x)p(x)dx}. \quad (2.1.1)$$

## 2.2 Maximum likelihood and minimum variance

Consider a case of two independent observations  $y_1$  and  $y_2$ . Their errors are assumed to be normally distributed with standard deviations  $\sigma_1$  and  $\sigma_2$ , respectively. Define  $x^a$  as the analysis of the most likely state of  $x$  under condition of the given observations. Then the probability distribution to measure  $y_1$  under condition of a given true state  $x$  is written as

$$p(y_1|x) = \frac{1}{\sqrt{2\pi}\sigma_1} \exp \left\{ -\frac{(y_1 - x)^2}{2\sigma_1^2} \right\}. \quad (2.2.1)$$

Further, the likelihood of a true state  $x$  under condition of the given observations  $y_1$  and  $y_2$  with standard deviations  $\sigma_1$  and  $\sigma_2$  are given by

$$L(x|y_1) = p(y_1|x) = \frac{1}{\sqrt{2\pi}\sigma_1} \exp \left\{ -\frac{(y_1 - x)^2}{2\sigma_1^2} \right\}$$

$$L(x|y_2) = p(y_2|x) = \frac{1}{\sqrt{2\pi}\sigma_2} \exp \left\{ -\frac{(y_2 - x)^2}{2\sigma_2^2} \right\},$$

respectively.

Hence, the most likely state of  $x$  under conditions of the given independent observations  $y_1$  and  $y_2$  is the maximum of the joint probability:

$$\max_x L(x|y_1, y_2) = p(y_1|x)p(y_2|x) =$$

$$\frac{1}{2\pi\sigma_1\sigma_2} \exp \left\{ -\frac{(y_1 - x)^2}{2\sigma_1^2} - \frac{(y_2 - x)^2}{2\sigma_2^2} \right\}, \quad (2.2.2)$$

which is similar to the maximum of the negative logarithm

$$\max_x \ln L(x|y_1, y_2) = \max_x \{const. - J(x)\}. \quad (2.2.3)$$

Thereby,

$$J(x) = \frac{1}{2} \left[ \frac{(x - y_1)^2}{\sigma_1^2} + \frac{(x - y_2)^2}{\sigma_2^2} \right]$$

$$= \frac{1}{2} \begin{bmatrix} x - y_1 \\ x - y_2 \end{bmatrix}^T \begin{bmatrix} \sigma_1^2 & 0 \\ 0 & \sigma_2^2 \end{bmatrix}^{-1} \begin{bmatrix} x - y_1 \\ x - y_2 \end{bmatrix} \quad (2.2.4)$$

is the *cost function*. Hence, the maximum likelihood is obtained if the cost function (2.2.4) is minimized. The minimum of the cost function is called the best linear unbiased estimate (**BLUE**).

## 2.3 Four-dimensional variational data assimilation

Four-dimensional variational data assimilation (4D-Var) allows to use observations distributed not only in space but also in time. The main goal of the 4D-Var is to optimise a state of the atmosphere  $x_0$  for the time  $t_0$  (*first guess*), so that the model analysis (*forecast*) started with this state  $M(x_0)$  for time interval  $(t_0, t_N)$  is as close as possible to all observations  $(y_1, \dots, y_p)$  scattered in this time interval and to the background (*a-priori*) information  $x^b$ . *A-priori* information can be the result of a previous analysis, climatological statistics, a model forecast or some combination of those.

Generalising (2.2.4) the cost function for this problem is written as follows

$$\begin{aligned} J(x_0) &= J^b + J^o = \\ &= \frac{1}{2}[x_0 - x^b]^T \mathbf{B}^{-1}[x_0 - x^b] + \\ &\quad \frac{1}{2} \sum_{i=0}^p [H(M_i(x_0)) - y_i]^T \mathbf{R}^{-1}[H(M_i(x_0)) - y_i]. \end{aligned} \quad (2.3.1)$$

Here  $R$  (a matrix of size  $p \times p$ ) and  $B$  (a matrix of size  $n \times n$ ) are the observation and background error covariance matrices, respectively and  $H$  (a matrix of size  $p \times n$ ) is the projection operator that maps the state vector from the  $m$ -dimensional model space on the  $p$ -dimensional observation space.  $M_i$  is the *model operator* generating the state  $x_i$  at time step  $t_i$  as a function of  $x_0$ .

The first term of the cost function (2.3.1) quantifies the distance between the background state and the first guess at the beginning of the time interval. The second term describes a sum of the distances between each observation  $y_i$  and the corresponding model state  $H(M_i(x_0))$  for the moment of observation.

Efficient minimisation algorithms like quasi-Newton or Conjugate-Gradient methods require the gradient of the cost function with respect to the control variables  $\mathbf{x}_0$  in order to find the minimum of  $J$ . The gradient of the cost function background part  $J^b$  is obtained by

$$\nabla_{\mathbf{x}_0} J^b = \mathbf{B}^{-1} [\mathbf{x}_0 - \mathbf{x}^b]. \quad (2.3.2)$$

On the contrary, the gradient of the observational cost function part  $J^o$  with respect to the initial model values is more difficult to calculate. However, it is easy to express the gradient of  $J^o$  with respect to the model variables at the time  $t_i$ , namely

$$\nabla_{\mathbf{x}_i} J^o = \mathbf{H}'^T \mathbf{R}^{-1} [H(\mathbf{x}_i) - \mathbf{y}_i]. \quad (2.3.3)$$

The calculation of  $\nabla_{\mathbf{x}_0} J^o$  is computationally the most demanding task of 4D-Var. Since the number of control variables in atmospheric models is of the order  $10^6$ – $10^7$ , the only feasible strategy to accomplish this calculation is given by utilising the adjoint model operator.

Let  $\langle \cdot, \cdot \rangle$  be the canonical scalar product. Then, the variation of a scalar function  $f : \mathbb{R}^n \rightarrow \mathbb{R}$  in response to a small variation  $\delta \mathbf{x}$  of  $\mathbf{x}$  can be approximated to the first order by

$$\delta f \approx \langle \nabla_{\mathbf{x}} f, \delta \mathbf{x} \rangle.$$

Due to the linearity of the scalar product, the variation of  $J^o$  is given by

$$\delta J^o \approx \sum_{i=0}^N \langle \nabla_{\mathbf{x}_i} J^o, \delta \mathbf{x}_i \rangle, \quad (2.3.4)$$

$$\text{where } \delta \mathbf{x}_i := M_i(\mathbf{x}_0 + \delta \mathbf{x}_0) - M_i(\mathbf{x}_0) \approx \mathbf{M}'_i \delta \mathbf{x}_0.$$

In other words,  $\delta \mathbf{x}_i$  is linked to the variation of the initial model values  $\delta \mathbf{x}_0$  by the tangent linear model  $\mathbf{M}'$ , which is the Jacobian of the model operator  $M$ . Using (2.3.4), the variation of the cost function can be expressed as

$$\delta J^o \approx \sum_{i=0}^N \langle \nabla_{\mathbf{x}_i} J^o, \mathbf{M}'_i \delta \mathbf{x}_0 \rangle = \sum_{i=0}^N \langle \mathbf{M}^*_i \nabla_{\mathbf{x}_i} J^o, \delta \mathbf{x}_0 \rangle. \quad (2.3.5)$$

$\mathbf{M}^*$  is the *adjoint model operator*, which is the transpose of the tangent linear  $\mathbf{M}'$  (see *Talagrand and Courtier [1987]* for a detailed discussion).

By combining (2.3.5) and (2.3.3), the gradient of  $J^o$  with respect to the initial model values  $\mathbf{x}_0$  can be determined as

$$\nabla_{\mathbf{x}_0} J^o = \sum_{i=0}^N \mathbf{M}^*_i \nabla_{\mathbf{x}_i} J^o = \sum_{i=0}^N \mathbf{M}^*_i \mathbf{H}'^T \mathbf{R}^{-1} [H(\mathbf{x}_i) - \mathbf{y}_i].$$

Hence, the complete gradient of the cost function with respect to the control variables  $\mathbf{x}_0$  can be written as

$$\nabla_{\mathbf{x}_0} J = \mathbf{B}^{-1} [\mathbf{x}_0 - \mathbf{x}^b] + \sum_{i=0}^N \mathbf{M}^*_i \mathbf{H}'^T \mathbf{R}^{-1} [H(\mathbf{x}_i) - \mathbf{y}_i]. \quad (2.3.6)$$

### 2.3.1 Adjoint model technique

A numerical model integration over a time interval  $[t_0, t_i]$  is subdivided into a number of time-steps:

$$\mathbf{x}_i = M_{i,i-1} \circ \cdots \circ M_{2,1} \circ M_{1,0}(\mathbf{x}_0).$$

Accordingly, the tangent linear  $\mathbf{M}'_i$  of this sequence of model operators is given by

$$\mathbf{M}'_i = \mathbf{M}'_{i,i-1} \cdots \mathbf{M}'_{2,1} \mathbf{M}'_{1,0}.$$

Since the model is non-linear, each of the linearized operators  $\mathbf{M}'_{l,l-1}$  explicitly depends on the current atmospheric state  $\mathbf{x}_{l-1}$ . In order to obtain the adjoint model operator by forming the transpose of the tangent linear, the sequence of operators is reversed:

$$\mathbf{M}^*_i = \mathbf{M}^*_{1,0} \cdots \mathbf{M}^*_{i-1,i-2} \mathbf{M}^*_{i,i-1}.$$

Thus, the adjoint model operator  $\mathbf{M}^*_i$  propagates the gradient of the cost function with respect to  $\mathbf{x}_i$  backward in time, to deliver the gradient of the cost function with respect to  $\mathbf{x}_0$ . Taking into account that each adjoint operator  $\mathbf{M}^*_{l,l-1}$  depends on  $\mathbf{x}_{l-1}$ , the sequence of atmospheric states must be available in reverse order for each time-step. To this end, all intermediate model states  $\mathbf{x}_l$  must be stored for  $l = 0, \dots, i$  during the forward integration of the model  $M$ . Alternatively, they have to be recomputed during the course of adjoint integration.

The adjoint model can be created from the computer code implementing the model  $M$ . By examining the whole program unit in reverse order, the adjoint code can be constructed statement by statement. A detailed description of this technique is given in *Giering and Kaminski* [1998]. Obviously, this approach is error-prone for comprehensive atmospheric models, with thousands of code lines. However, the hard coding work can be alleviated by partly automated using of adjoint compilers like TAMC (*Giering* [1999]) or *Tapenade* (*Hascoët and Pascual* [2004]).



## CHAPTER 3

---

### The SACADA assimilation system

---

SACADA, Synoptic Analysis of Chemical constituents by Advanced Data Assimilation, is a four-dimensional variational assimilation system developed for the estimation of transport and chemical transformation of atmospheric trace gases in the stratosphere (*Elbern et al.* [2010]). The version developed in this study is designed to analyze two aircraft-based measurement campaigns, SCOUT-O3 and AMMA, over the periods November-December 2005 and July-August 2006, respectively (*Hoffmann et al.* [2009], *Weigel et al.* [2010]; see chapter 6 for more details).

A key issue of this work was to adapt the SACADA assimilation system for the assimilation of high resolution aircraft measurements. Therefore, a model grid refinement and an extension of the chemical mechanism are undertaken. This chapter gives an overview of the main components of the SACADA system, such as the model operator  $M$ , including the chemistry transport module for solving a system of chemical reactions and its adjoint. The meteorological module, the grid configuration and the parallelization technique are adopted from the global numerical weather prediction model (GME) of the German Weather Service (*Majewski et al.* [2001a]).

### 3.1 The SACADA model

Within SADACA the atmospheric state is described by a system of partial differential equations (PDEs), where the temperature  $T$ , pressure  $p$ , the horizontal wind field  $\mathbf{v}$ , the density of the air parcel  $\rho$ , the mixing ratio of water in its various phases  $\mathbf{q}$  and the mixing ratios  $\mathbf{c}$  of trace gases are given by (see e.g. *Kalnay [2003]*)

$$\frac{d\mathbf{v}}{dt} = -\alpha\nabla p - \nabla\phi + \mathbf{F} - 2\boldsymbol{\Omega} \times \mathbf{v} \quad (3.1.1a)$$

$$\frac{\partial\rho}{\partial t} = -\nabla(\mathbf{v}\rho) \quad (3.1.1b)$$

$$\frac{\partial\mathbf{q}}{\partial t} = -\mathbf{v}\nabla\mathbf{q} + (\mathbf{E} - \mathbf{C}) \quad (3.1.1c)$$

$$\frac{\partial\mathbf{c}}{\partial t} = -\mathbf{v}\nabla\mathbf{c} + (\mathbf{P} - \mathbf{L}) \quad (3.1.1d)$$

$$Q = C_p \frac{dT}{dt} - \alpha \frac{dp}{dt}. \quad (3.1.1e)$$

Here,  $\phi$  is the geopotential,  $\alpha$  is the specific volume of air (the inverse of the density  $\rho$ ),  $\boldsymbol{\Omega}$  is the angular velocity of the Earth and  $\mathbf{F}$  is the frictional force. Equation (3.1.1a) represents the conservation of momentum, equation (3.1.1b) denotes the conservation of mass. The equation (3.1.1c) describes change of water vapor mixing ratio in time ( $t$ ) with  $\mathbf{E}$  and  $\mathbf{C}$  denoting the rate of change due to liquid, solid and gas phase transitions. Equation (3.1.1e) represents conservation of energy with the rate of heating  $Q$ . Equation (3.1.1d) is solved by the chemistry transport module of the SACADA model, later called SACADA-CTM, using the precomputed meteorological fields.  $\mathbf{P}$  and  $\mathbf{L}$  are representing for the chemical production and loss, respectively. Equations (3.1.1c) and (3.1.1e) are solved by the German Weather Service's global forecast model GME, which serves as meteorological driver. GME is coupled online with SACADA, thus, both models share the same grid resolution.

SACADA has to comply with several requirements, such as to be efficient in order to deliver analyses in near real-time. Another requirement concerns the model error, which should be kept as small as possible, as in 4D-var  $M$  is considered to be perfect. The benefit of having the meteorological model included in assimilation system is that interpolation errors of the meteorological fields such as wind and temperature on the model grid can be avoided, as in this case both modules are using the same grid. SACADA is the first 4D-var stratospheric constituent data assimilation model that combines a comprehensive stratospheric chemistry module and a meteorological model.

The icosahedral grid adopted from GME is one of the essential benefits in the SACADA system. The main advantage of the icosahedral-hexagonal grid, in comparison to traditional grid structures like latitude-longitude grids, is a rather small variability of the area of grid cells, as the well-known pole-problem of the latitude-longitude grid does not exist while using the GME grid (*Kalnay [2003]*).

## 3.2 Chemistry transport module

In the framework of this study, the chemistry transport module of SACADA assimilation system was improved. The chemistry mechanism was revised and all reaction rates were updated according to Jet Propulsion Laboratory (JPL) recommendations. Thus, a novel global chemistry transport model (CTM) with its adjoint version is now the kernel of SACADA system. The new chemistry mechanism and its adjoint was tested according to *Chao and Chang [1992]*. In this section the principal features of the chemistry mechanism are described.

The SACADA-CTM solves equation (3.1.1d). An operator splitting approach (*McRae et al. [1982]*) is used to obtain the discrete approximate solution of this partial differential equation. The PDE is splitted into three sub-problems, written in the local coordinate system of the icosahedral grid (*Schwinger [2006]*), such as

$$\left(\frac{\partial \mathbf{c}}{\partial t}\right)^h = -\frac{u}{R_E} \frac{\partial \mathbf{c}}{\partial \eta} - \frac{v}{R_E} \frac{\partial \mathbf{c}}{\partial \chi}, \quad (3.2.1a)$$

$$\left(\frac{\partial \mathbf{c}}{\partial t}\right)^v = -w \frac{\partial \mathbf{c}}{\partial p}, \quad (3.2.1b)$$

$$\left(\frac{\partial \mathbf{c}}{\partial t}\right)^c = (\mathbf{P} - \mathbf{L}). \quad (3.2.1c)$$

These equations describe the temporal evolution in the volume mixing ratio due to horizontal advection (3.2.1a), vertical advection (3.2.1b) and chemical production and loss (3.2.1c), denoted by the superscripts h, v, and c, respectively.

Different numerical schemes are used to discretise and solve each of these equations. As the chemical differential equations are stiff, the implicit scheme with an adaptive step size control is used for solving them. Thus, the concentrations on time-step  $t_{n+1}$  are obtained by

$$\mathbf{c}(t_{n+1}) = [M^c(t_n) \circ M^v(t_n) \circ M^h(t_n)] \mathbf{c}(t_{n-1}). \quad (3.2.2)$$

Here,  $M^c$ ,  $M^v$  and  $M^h$  are discrete operators that solve (3.2.1a) – (3.2.1c). In order to calculate concentrations at time-step  $t_{n+1}$  from time-step  $t_{n-1}$ , the meteorological information on time-step  $t_n$  is used. Hence, equation (4.10) describes a forward time stepping using twice the meteorological time step, where the meteorological data are at the center of the time interval. An advantage of this kind of approach is the reduction of levels, where the field of chemical constituents have to be stored, for using them in adjoint computations.

### Chemistry scheme and solver

The chemical reaction mechanism of SACADA-CTM was revised and extended. All reaction rates were updated according to the recommendations of the JPL (*Sander et al.* [2011]). The current SACADA-CTM includes a set of 49 photolysis reactions, 138 gas phase reactions and 10 heterogeneous reactions on surfaces of Polar Stratospheric Cloud (PSC) particles and in sulphate aerosol droplets. The reaction equations together with their rate constants are listed in Tables A.2, A.3 and A.4.

**The kinetic preprocessor (KPP)** is a software tool that assists the computer simulation of chemical kinetic systems (*Sandu et al.* [2003]). KPP is used to construct a module solving equation (3.2.1c) for each grid cell. The chemical reaction mechanism of SACADA is formulated in the special KPP language and the KPP generated source code in **Fortran**, with some additional modifications, is implemented in SACADA assimilation system.

The numerical solution of equation (3.2.1c) is obtained by *a second order Rosenbrock method* (*Verwer et al.* [1997]). It is a two stage linear-implicit scheme. For an arbitrary autonomous differential equation  $d\mathbf{x}/dt = f(\mathbf{x})$  with  $f : \mathbb{R}^m \rightarrow \mathbb{R}^m$  the Rosenbrock method reads as:

$$\mathbf{x}(t + \tau) = \mathbf{x}(t) + \frac{3}{2}\tau\mathbf{k}_1 + \frac{1}{2}\tau\mathbf{k}_2, \quad (3.2.3)$$

and the coefficients  $\mathbf{k}_1$  and  $\mathbf{k}_2$  are obtained from

$$\begin{aligned} (\mathbf{I} - \gamma\tau\mathbf{J})\mathbf{k}_1 &= f(\mathbf{x}(t)) \\ (\mathbf{I} - \gamma\tau\mathbf{J})\mathbf{k}_2 &= f(\mathbf{x}(t) + \tau\mathbf{k}_1) - 2\mathbf{k}_1, \end{aligned} \quad (3.2.4)$$

where  $\gamma = 1 + 1/\sqrt{2}$  and  $\tau$  is the step length,  $\mathbf{I}$  and  $\mathbf{J}$  are identity and Jacobian matrices, respectively. (*Verwer et al.* [1997], *Sander et al.* [2003]).

**The Tropospheric Ultraviolet-Visible** (TUV) Radiation Model is a radiation transfer model developed at the Atmospheric Chemistry Division of US National Center for Atmospheric Research (NCAR), which calculates spectral irradiances, spectral actinic fluxes, and photo-dissociation rates for the wavelength range between 120 and 735 nm. The TUV Version 4.2 is adapted to the SACADA model in order to build a look-up table of photo-dissociation frequencies for the stratospheric SACADA assimilation system (*Schwinger* [2006]). The look-up table contains photolysis rates  $\mathbf{J}(z, c_o, \phi)$  for different values of the zenith angle  $\phi$ , the overhead ozone column  $c_o$ , dependent on the altitude  $z$  as defined by the vertical SACADA model grid. Note that  $c_o$  is defined as a factor, which describes an enhancement or reduction of a standard ozone column. In the framework of this work the TUV SACADA model is revised, all cross section input data is updated according to the recommendations issued by the JPL and the new look-up table is built for a refined SACADA model grid.

### 3.3 The adjoint model

To calculate the gradient of the cost function with respect to the initial concentrations  $\nabla_{c_o} J$  the adjoint of the model operator  $M^*$  is needed (see Equation 2.3.6). The transpose of the tangent-linear (or Jacobian) of the operators  $M^h$  is obtained by forming the tangent-linear of each individual line of code and transposing it, as described by *Giering and Kaminski* [1998]. The adjoint of  $M^c$  is provided by KPP using the adjoint of the Rosenbrock numerical scheme (*Sandu et al.* [2005]). As the operator  $M^v$  is linear, the Jacobian

$$\frac{\partial M^v}{\partial \mathbf{c}} = [\mathbf{I} + 2\Delta t \mathbf{A}]^{-1}$$

is the operator itself and hence, the adjoint is the simple transpose

$$\mathbf{M}^{v*} = [\mathbf{I} + 2\Delta t \mathbf{A}]^{-T} .$$

The values for the recomputation of the required variables for  $\mathbf{M}^{c*}$  and  $\mathbf{M}^{h*}$  are saved to disk at each time step. Thereby, the volume mixing ratios are applied *before* the respective model operator.

During the adjoint model integration, the gradient of the observational cost function part is added to the adjoint variable  $\tilde{\mathbf{c}}^*(t_{n+1})$ . Thereby observations  $\mathbf{y}_{n+1}$  within the time interval  $[t_n, t_{n+2}]$  are taken into account. Then  $\tilde{\mathbf{c}}^*(t_{n+1})$

is propagated backward in time by means of the adjoint model:

$$\begin{aligned} \mathbf{c}^*(t_{n+1}) &= \tilde{\mathbf{c}}^*(t_{n+1}) + \mathbf{H}^T \mathbf{R}^{-1} [\mathbf{y}_{n+1} - \mathbf{H}\mathbf{c}(t_{n+1})] \\ \mathbf{c}^*(t_{n-1}) &= [\mathbf{M}^{h*} \circ \mathbf{M}^{v*} \circ \mathbf{M}^{c*}] \mathbf{c}^*(t_{n+1}) \end{aligned} \quad (3.3.1)$$

Finally, at  $n - 1 = 0$ , the gradient of  $J^o$  with respect to the initial volume mixing ratios  $\mathbf{c}(t_0)$  is obtained:

$$\nabla_{\mathbf{c}_0} J^o = \mathbf{c}^*(t_0).$$

### 3.4 Meteorological module, grid configuration and parallelization

The German Weather Service global forecast model GME, which is the first operational meteorological model utilizing an icosahedral grid structure, was made available (model version 1.22) and serves as the meteorological driver module in the SACADA assimilation system. Since the new parts of the SACADA model, which are developed in the framework of this study, include improvement of the icosahedral GME grid, the principal features of GME is presented in this section. For a more detailed description of the GME model, the reader is referred to *Majewski et al.* [2001*b*].

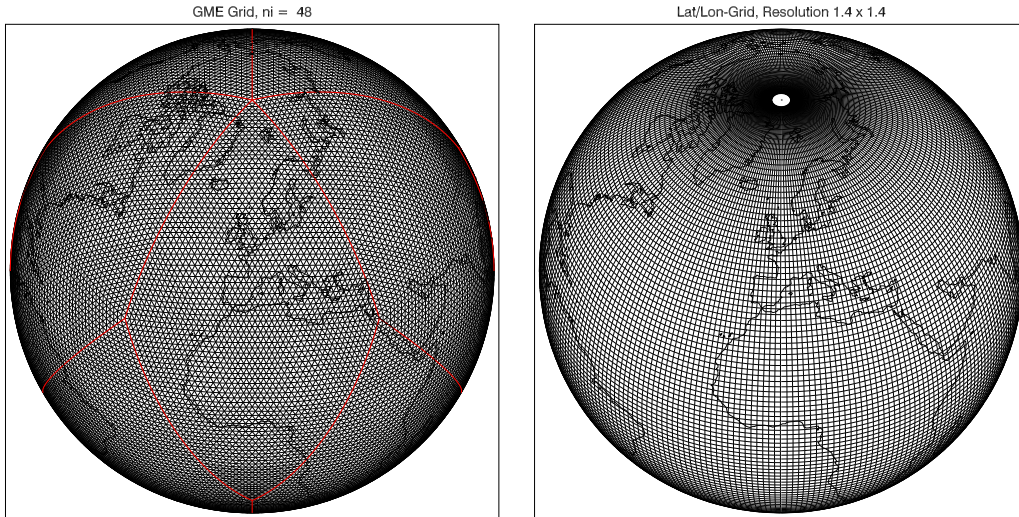


**Figure 3.1:** Icosahedral grid with a resolution of  $n_i = 48$  (left). The distance between neighboring grid points is about 147 km. The boundaries of diamonds (see text) are marked by red lines. A conventional latitude-longitude grid with a resolution of  $1.4^\circ \times 1.4^\circ$  for comparison (right).

To generate the icosahedral-hexagonal grid, a regular icosahedron, the highest Platonic body with 20 equilateral triangles, is constructed inside the sphere such that two of its twelve vertices coincide with the North Pole (NP) and South Pole (SP), respectively. The resulting sections of great circles (*or* sides of the triangles), are equally subdivided into a number of  $n_i$  intervals each. Thus, each of the triangles are divided in  $n_i^2$  sub-triangles. As shown in the upper graphic of Figure 3.1, the constructed grid is almost isotropic. Each grid point has six nearest neighbors with the exception of twelve points located at the vertices of the original icosahedron (called *special points* hereafter), which have only five direct neighbors. The area of representativeness for a grid cell is a hexagon and pentagon at the twelve special points, respectively (see Figure 3.2).

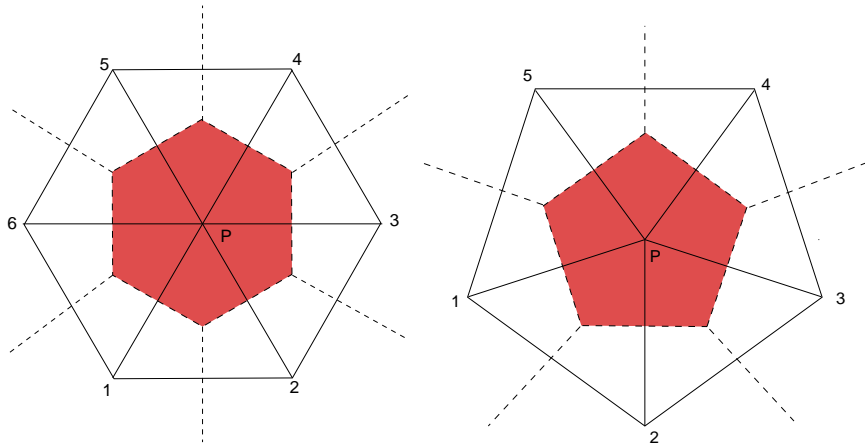


**Figure 3.2:** The icosahedral grid cells geometry. The area of representativeness assigned to each grid cell is a hexagon or a pentagon at the twelve special points, respectively.

This approach of the grid structure results in a mesh with virtually constant mesh size all over the globe. Thereby the minimum and maximum separation between neighboring grid points  $\Delta_{\min}$  and  $\Delta_{\max}$  varies about 20% only. For the SACADA system in this study it has been decided that  $n_i = 48$  gives a sufficient resolution, resulting in 23 042 grid points per level. The minimum and maximum distances are  $\Delta_{\min} = 147$  km and  $\Delta_{\max} = 176$  km, and the average area of representativeness is about 24 000 km<sup>2</sup>. A comparable traditional latitude-longitude grid (lower graphic of Figure 3.1), that is a grid with the same area represented by one grid cell at the equator (where the resolution is coarsest), requires a grid spacing of  $1.4^\circ \times 1.4^\circ$ . This results in 33 024 grid points per level, which is about 40% more than the icosahedral grid. To obtain a rectangular data structure for the icosahedral grid, two adjacent spherical triangles are combined to form a *diamond*, partitioning the grid into ten lo-

gically rectangular sub-grid domains as marked by the thick red lines in the upper panel of Figure 3.1.

For discretisation in vertical direction the GME uses a hybrid  $\sigma$ -pressure coordinate system and an advection scheme that is proposed by *Simmons and Burridge* [1981]. The pressure for each level is given by a set of two parameters

$$\begin{aligned} p_{f,k} &= a_{f,k} + b_{f,k} p_s & \text{for } k = l_s, \dots, l_e \\ p_k &= a_k + b_k p_s & \text{for } k = l_s, \dots, l_e + 1, \end{aligned} \quad (3.4.1)$$

where  $p_{f,k}$  is the pressure at the center of each layer,  $p_k$  the pressure at the layer boundaries and  $p_s$  is the standard sea level surface pressure (1013.25 hPa) and heights have been computed from pressure according to the U.S. Standard Atmosphere from 1976. The coefficients  $a_k$ ,  $b_k$  and  $a_{f,k}$ ,  $b_{f,k}$  determine the vertical structure of the grid. A staggered Charney-Phillips grid is used with the geopotential and the vertical wind specified at the boundaries of layers.

As the main objective of this work is the assimilation of high resolution aircraft data, the number of model layers is increased from 32 to 54 for the SACADA assimilation system compared to the operational GME (version 1.22).

The top level pressure is reduced from 10.0 hPa to 0.1 hPa. The coefficients for the vertical grid are listed in Appendix A, Table A.1. The resulting pressure values, together with the corresponding heights are shown in Figure 3.3.

Thus, in this study the layer thickness is less than 1 km up to 22 km altitude. In the altitude range between 22 to 50 kilometer the layer thickness is about 2 km, and it increases up to 8 km above 50 kilometer altitude. The chemistry in SACADA system is applied above 6 km altitude, it is a gray marked area in Figure 3.3, while the GME is applied to all vertical range.

In order to speed-up and optimize the model run on parallel computers a diamond-wise domain decomposition is used, as shown in Figure 3.4. Each processor works on one segment of each diamond. This is a simple but effective strategy to achieve a good load distribution between processors. Each domain has a *halo* of two rows and columns of grid points that have to be exchanged between processors. For this purpose the MPICH library is used (*Gropp et al.* [1996]), which implements the Message Passing Interface (MPI) standard.

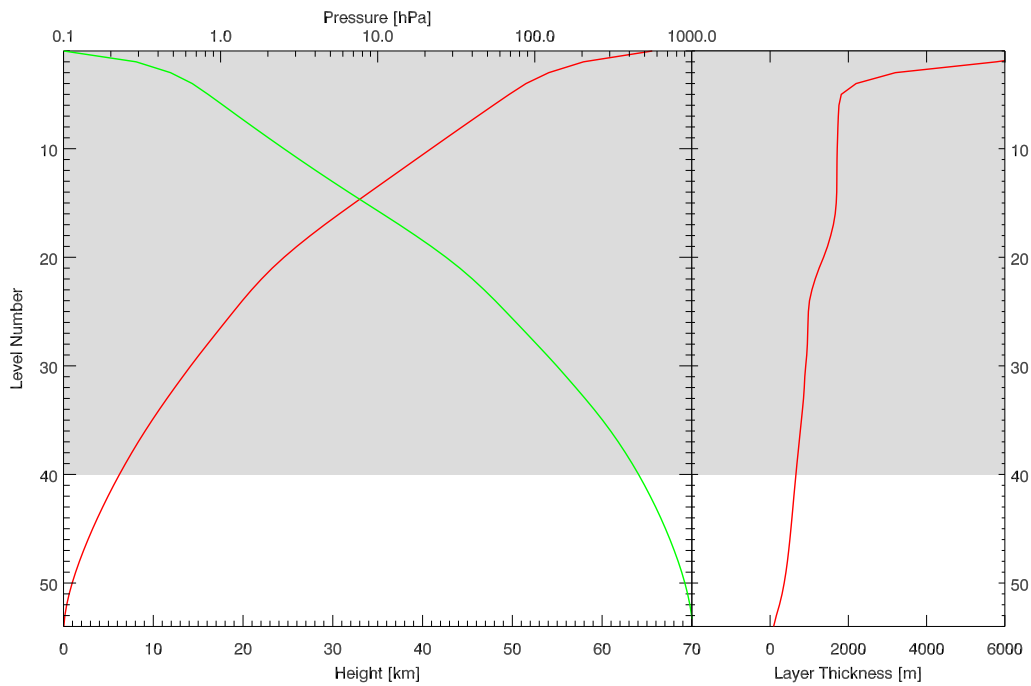


**Figure 3.3:** Pressure (top scale, green line) and height (bottom scale, red line) of SACADA model layers. On the right hand side the resulting layer thickness is shown. Values are valid for standard sea level surface pressure (1013.25 hPa) and heights have been computed from pressure according to the U.S. Standard Atmosphere from 1976. Chemistry computations and consequently the assimilation of trace gas observations is restricted to the grey shaded region in the work presented here.

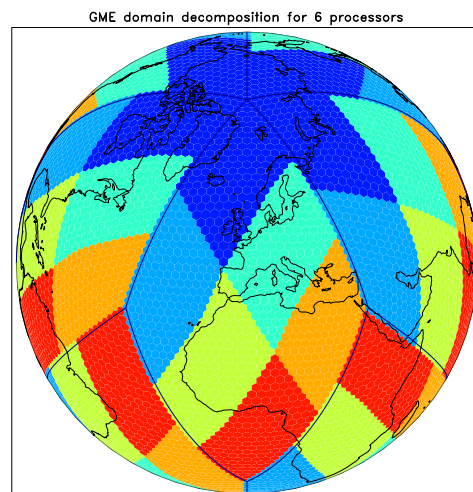


**Figure 3.4:** Domain decomposition for six processors. Each color indicates a region that is assigned to one processor (Schwinger [2006]).



## CHAPTER 4

---

### Background error covariance modeling

---

A major task in the development of a variational data assimilation system is the estimation and representation of the background error covariances (*Weaver and Courtier* [2001]). In equation (2.3.1) each single observation and the model values are weighted by observation and background error covariances. The correct choice of background error covariances is important, in order to have properly weighted parts of the cost function to obtain a BLUE. In the case of a diagonal background error covariance matrix (BECM) the analysis of 4D-Var would have a singular peaks at the observation locations. This can be an exemption of atmospheric state, due to some meteorological events, but rarely expected for atmospheric chemical constituents. Hence, the BECM non-diagonal entries are essential, as they ensure the mixing properties of the atmospheric chemical constituents.

The idea of straightforward implementation of BECM is obsolete due to two facts. First, the size of the BECM is practically unhandleable. In the SACADA assimilation system with its  $54 \times 23042$ , the resulting dimension for one model variable is  $N \approx 5 \times 10^5$ . The corresponding univariate BECM would be of size  $(N^2 + N)/2 \approx 10^{11}$ . To store the BECM for 51 different chemical species approximately 80 Terabytes of memory is needed. This is not viable even with today's high computational resources. Second, the entries of the BECM is statistical information, which are difficult to obtain.

Thus, the BECM elements cannot be calculated exactly or stored explicitly in matrix form. Therefore, it is necessary to have a proper parametrisation

including the main characteristics of the BECM. The SACADA assimilation system BECM parametrisation rely on the diffusion approach proposed by *Weaver and Courtier* [2001]. The main idea here is use of the diffusion approach for correlation modelling.

## 4.1 Incremental formulation of the cost function

Preconditioning is the main purpose of square root calculation. Since matrix  $\mathbf{B}$  is non-singular, the control variables are substituted in a new vector

$$\mathbf{v}_0 := \mathbf{B}^{-1/2} \delta \mathbf{x}_0 \quad \text{with} \quad \delta \mathbf{x}_0 := \mathbf{x}_0 - \mathbf{x}^b. \quad (4.1.1)$$

The square root of the background error covariance matrix is taken to be any square root decomposition of  $\mathbf{B}$  such that  $\mathbf{B} = \mathbf{B}^{1/2} \mathbf{B}^{T/2}$  holds (*Weaver and Courtier* [2001]). Hence, the relation of  $\mathbf{x}_0$  to the new incremental variable is given by

$$\mathbf{x}_0 = \mathbf{B}^{1/2} \mathbf{v}_0 + \mathbf{x}^b. \quad (4.1.2)$$

The cost function remains invariant under this transformation, i. e.  $J(\mathbf{x}_0) = J(\mathbf{v}_0)$ , while the gradient of the background cost portion is simplified to

$$\nabla_{\mathbf{v}_0} J^b = \nabla_{\mathbf{v}_0} \left[ \frac{1}{2} \mathbf{v}_0^T \mathbf{v}_0 \right] = \mathbf{v}_0. \quad (4.1.3)$$

The construction of the gradient of the cost functions observational part with respect to the new vector of control variable (4.1.1) is done in the same way as in Section 2.3, taking into account that by definition  $\mathbf{v}_0$  represents a small variation around zero, with  $\mathbf{v}_0 = 0$  corresponding to  $\mathbf{x}_0 = \mathbf{x}^b$ :

$$\begin{aligned} \delta J^o &= \langle \nabla_{\mathbf{x}_0} J^o, \delta \mathbf{x}_0 \rangle = \langle \nabla_{\mathbf{x}_0} J^o, \mathbf{B}^{1/2} \mathbf{v}_0 \rangle \\ &= \langle \mathbf{B}^{T/2} \nabla_{\mathbf{x}_0} J^o, \mathbf{v}_0 \rangle. \end{aligned}$$

Thus, the gradient of  $J^o$  with respect to  $\mathbf{v}_0$  is obtained by multiplying the gradient of  $J^o$  with respect to  $\mathbf{x}_0$  from the left by the transposed square root of  $\mathbf{B}$ :

$$\nabla_{\mathbf{v}_0} J^o = \mathbf{B}^{T/2} \nabla_{\mathbf{x}_0} J^o. \quad (4.1.4)$$

Since  $\mathbf{v}_0$  is the vector of control variables and the gradient of  $J^b(\mathbf{v}_0)$  at the same time, there is no need to recalculate  $\nabla_{\mathbf{v}_0} J^b$  by means of (4.1.1) for each iteration, because  $\mathbf{v}_0$  is the output of the minimisation algorithm at the

preceeding iteration. Furthermore, a real world assimilation system will start the iterative process of minimising  $J$  by choosing  $\mathbf{x}_0 = \mathbf{x}^b$  as a first guess atmospheric state, resulting in  $\mathbf{v}_0 = 0$  at the first iteration. Consequently, the transformation (4.1.1), and hence  $\mathbf{B}^{-1/2}$ , is never needed to be known explicitly. The initial values for the next forward run are obtained from

$$\mathbf{x}_0 = \mathbf{B}^{1/2}\mathbf{v}_0 + \mathbf{x}^b. \quad (4.1.5)$$

Here,  $\mathbf{v}_0$  is the updated control variable computed by the minimisation algorithm.

## 4.2 Correlation modelling with diffusion approach

The error covariance matrix  $\mathbf{B}$  can be decomposed into a correlation matrix

$$\mathbf{C} = \begin{pmatrix} 1 & \rho_{1,2} & \cdots & \rho_{1,n} \\ \rho_{1,2} & 1 & \cdots & \rho_{2,n} \\ \vdots & \vdots & \ddots & \vdots \\ \rho_{1,n} & \rho_{2,n} & \cdots & 1 \end{pmatrix},$$

containing the error correlations  $\rho_{i,j} = E[(\epsilon_i - E[\epsilon_i])(\epsilon_j - E[\epsilon_j])]/\sigma_i\sigma_j$ , and diagonal matrices  $\mathbf{\Sigma} = \text{diag}(\sigma_1, \dots, \sigma_n)$  containing the standard deviations such that,

$$\mathbf{B} = \mathbf{\Sigma} \mathbf{C} \mathbf{\Sigma}. \quad (4.2.1)$$

Thus, the construction of an error covariance matrix can be splitted into two separate tasks: The estimation of the variances  $\sigma$  for each control variable and the specification of error correlations between them.

The incremental formulation requires square root decomposition of  $\mathbf{B}$

$$\mathbf{B} = \mathbf{B}^{1/2} \mathbf{B}^{T/2} = \mathbf{\Sigma} \mathbf{C}^{1/2} \mathbf{C}^{T/2} \mathbf{\Sigma}$$

Since a direct implementation of  $\mathbf{C}$  is not feasible, construction of a *correlation operator*, which replaces the matrix-vector multiplication, is needed. Following *Weaver and Courtier* [2001], the main principle and pattern of the diffusion approach is described in the next. They show that the matrix-vector multiplication  $\mathbf{\Sigma} \mathbf{C}^{1/2}x$  can be replaced by the application of a *diffusion operator*  $\mathbf{L}(x)$ , under the assumption that the spatial correlations are Gaussian distributed. Here,  $\mathbf{L}$  calculates the solution of a two-dimensional diffusion equation

$$\frac{\partial \psi}{\partial t} - \kappa \nabla^2 \psi = 0 \quad (4.2.2)$$

on the sphere  $S^2 := \{(x, y, z) : \sqrt{x^2 + y^2 + z^2} = a\}$  with radius  $a$ . The solution  $\psi(\lambda, \phi, t)$  at time  $t$  is given by a convolution of  $\psi(\lambda, \phi, 0)$  with a *quasi-Gaussian* function  $f(\theta, \kappa t)$ , which depends on the angular separation  $\theta$  between two points  $(\lambda, \phi)$  and  $(\lambda', \phi')$  on the sphere (see *Weaver and Courtier* [2001] for a comprehensive discussion). The term *quasi-Gaussian* refers to the fact that  $f(\theta, \kappa t)$  closely approximates a Gaussian function provided that the involved length-scale is small compared to the radius of the sphere ( $L \ll a$ ), which is the case for scales relevant in atmospheric modelling. Under this condition the correlation length-scale can be approximated by

$$L^2 \approx 2\kappa t, \quad (4.2.3)$$

with diffusion coefficient  $\kappa$  and  $t$  being the diffusion time.

Caused by a connection between model dynamics and background error covariances, the background error indicates strong correlation between air parcels of the same air mass (*Riishøjgaard* [1998]). The potential vorticity (PV)

$$P = (\nabla \times \mathbf{v} + 2\boldsymbol{\Omega}) \cdot \nabla\theta = \boldsymbol{\zeta} \cdot \nabla\theta, \quad (4.2.4)$$

is used to identify different air masses. Here,  $\theta$  is the potential temperature and  $\boldsymbol{\zeta}$  the vector of absolute vorticity (see *Pichler* [1997]).

The diffusion approach described above can be generalised to account for anisotropic and inhomogeneous background error correlations. Following *Weaver and Courtier* [2001], this is accomplished by introducing a symmetric coordinate stretching tensor  $\mathbf{S}$  in the horizontal two-dimensional diffusion equation

$$\frac{\partial\psi}{\partial t} - \kappa_h \operatorname{div}(\mathbf{S} \operatorname{grad}_h \psi) = 0. \quad (4.2.5)$$

The tensor  $\mathbf{S}$  is composed of a diagonal tensor  $\tilde{\mathbf{S}}$  containing stretching factors  $\tilde{s}_1$  and  $\tilde{s}_2$  and a rotation tensor  $\mathbf{T}$ , with a rotation angle  $\alpha$ , which rotates the local coordinate system such that the stretching can be applied along the flow

$$\mathbf{S} = \mathbf{T}(\alpha)\tilde{\mathbf{S}}\mathbf{T}^T(\alpha) = \begin{pmatrix} \cos \alpha & \sin \alpha \\ -\sin \alpha & \cos \alpha \end{pmatrix} \begin{pmatrix} \tilde{s}_1 & 0 \\ 0 & \tilde{s}_2 \end{pmatrix} \begin{pmatrix} \cos \alpha & -\sin \alpha \\ \sin \alpha & \cos \alpha \end{pmatrix}. \quad (4.2.6)$$

### 4.3 Current setup

Two background error covariance parameterisations, an isotropic and a generalised scheme based on Equation (4.2.5), have been developed for the SACADA

system. For a more detailed description, the reader is referred to *Elbern et al.* [2010]. The kernel of the schemes is the diffusion operator

$$\mathbf{L} = \left\{ \left\{ \mathbf{I} - \kappa_v \Delta t \mathbf{D}_v \right\}^{-1} \left\{ \mathbf{I} + \kappa_h \Delta t \mathbf{D}_h \right\} \right\}^M \quad (4.3.1)$$

The random method described by *Weaver and Courtier* [2001] is used for the calculation of the normalisation factors for the anisotropic scheme. The rotation angle  $\alpha$  is calculated at each grid point as the angle between the gradient of the potential vorticity and the north-direction of the local coordinate system. Hence, according to (4.2.6),  $\mathbf{T}^T \nabla_h \psi$  is the gradient of an arbitrary scalar field  $\psi$  transformed into a  $(\tilde{\eta}, \tilde{\chi})$  coordinate system, where the  $\tilde{\chi}$ -axis is aligned to the direction of the PV-gradient. Consequently, the stretching factors  $\tilde{s}_1$  and  $\tilde{s}_2$  specify the stretching or shrinking of coordinates  $(\tilde{\eta}, \tilde{\chi})$  in the direction perpendicular and parallel to the PV-gradient, respectively. In the current version of the SACADA system, the full stretching is applied for PV-gradients greater than  $0.2(\nabla P)_{\max}$ , where  $(\nabla P)_{\max}$  is the maximum PV-gradient at the corresponding model level. Below this value there is a linear decrease of stretching factors. Finally, at locations where the PV-gradient equals zero, no coordinate stretching is applied.



## CHAPTER 5

---

### Observational Basis

---

Data assimilation adds value to the observations by filling in the spatio-temporal gaps in observations. Thus, the availability of observations is a key issue of data assimilation. This chapter contains instrument and their data product description assimilated and/or validated by SACADA assimilation system in the framework of this study.

#### 5.1 CRISTA-NF

The Cryogenic Infrared Spectrometers and Telescope for the Atmosphere (CRISTA) is an instrument developed by the University of Wuppertal for studies of small-scale structures in atmospheric trace gas distributions from space. After successful measurements during two Space Shuttle flights in November 1994 and August 1997 it was decided to use the same measurement technique for a new infrared sensor which is particularly suitable for deployment on board the high-flying research plane. In cooperation with the research centre Juelich (IEK-7), the centre telescope of CRISTA was adapted for use in the high-flying Russian research aircraft M55 Geophysica, and became the new airborne instrument CRISTA-New Frontiers (CRISTA-NF)(see Figure 5.1).

*“CRISTA-NF has been developed to close the resolution gap between satellite- and in-situ measurements and to provide atmospheric field data with high spatial resolution in the upper troposphere and lower stratosphere region.” (Hoff-*

*mann et al. [2009])*



**Figure 5.1:** CRISTA-NF on board of the high-flying research aircraft M55 Geophysica. Source: <http://www.atmos.physik.uni-wuppertal.de> .

CRISTA-NF looks from the starboard side of the aircraft in a limb viewing mode. Mid-infrared spectra ( $4\text{-}15\ \mu\text{m}$ ) are measured by two spectrometers at varying tangent heights (see Figure 5.2). Based on inverse methods the abundance of trace gases and their spatial distribution in the upper and lower stratospheres can be derived from the emission measurements (*Schroeder et al. [2009]*).

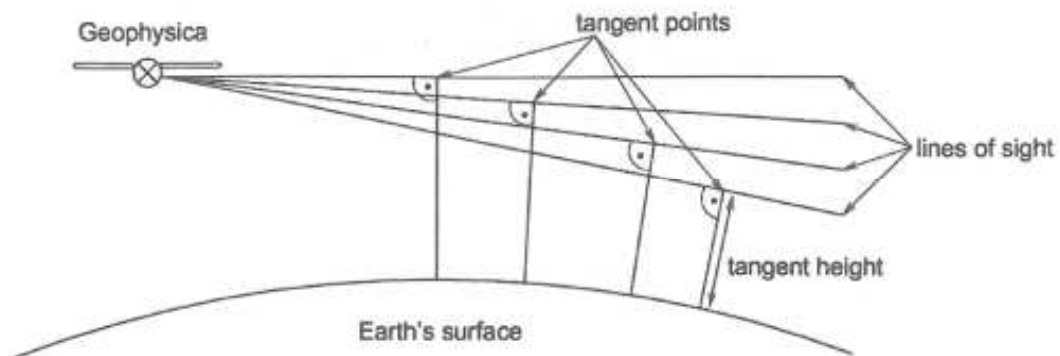


**Figure 5.2:** Illustration of the limb sounding technique by CRISTA-NF. By *Schroeder et al. [2009]*.

The measurements of CRISTA-NF (abbreviated CNF hereafter) cover the altitude range 5-20 km, with a vertical sampling and field of view of about 250

m. The distance of vertical scans along the flight track is below 15 km. Retrievals can estimate temperature, water vapour ( $H_2O$ ), ozone ( $O_3$ ), nitric acid ( $HNO_3$ ), peroxyacetyl nitrate (PAN), carbon tetrachloride ( $CCl_4$ ) and aerosol extinction.

Two campaigns took place within the remote sensing experiment: SCOUT-O3 and SCOUT-AMMA, over the periods November-December 2005 and July-August 2006, respectively (*Hoffmann et al.* [2009], *Weigel et al.* [2010], *Cairo et al.* [2010]). These campaigns were studied in this work and are described in Chapter 6.

## 5.2 MLS

The Earth Observing System (EOS) Microwave Limb Sounder (MLS) is one of four instruments on the NASA's EOS Aura satellite (see Figure 5.3), launched on July 15th 2004. The MLS sensor measures naturally-occurring microwave thermal emission from the limb (edge) of Earth's atmosphere viewing forward along the Aura spacecraft flight direction, scanning its view from the ground to  $\sim 90$  km every  $\sim 25$  seconds.

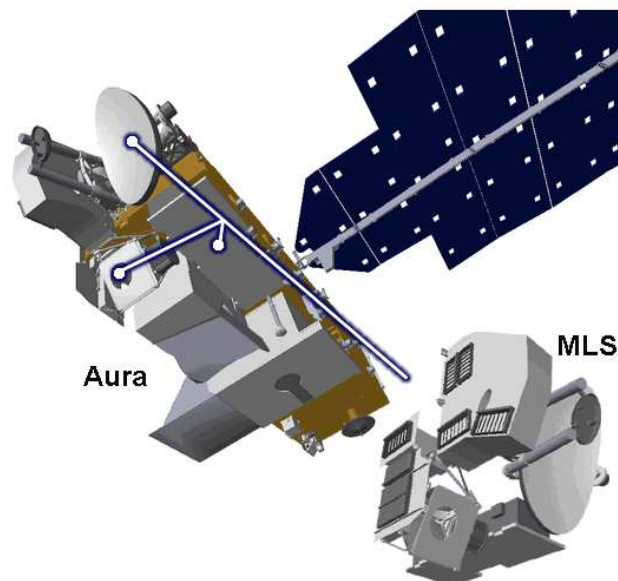


**Figure 5.3:** EOS MLS on AURA. Source: <http://mls.jpl.nasa.gov/index-eos-mls.php>.

MLS is a collaboration between the United States and the United Kingdom. The California Institute of Technology Jet Propulsion Laboratory (JPL) has overall responsibility for its development and implementation. The Institute

of Atmospheric and Environmental Science of the University of Edinburgh has responsibility for aspects of data processing algorithm development, data validation, and scientific studies (*Waters et al.* [2004]).

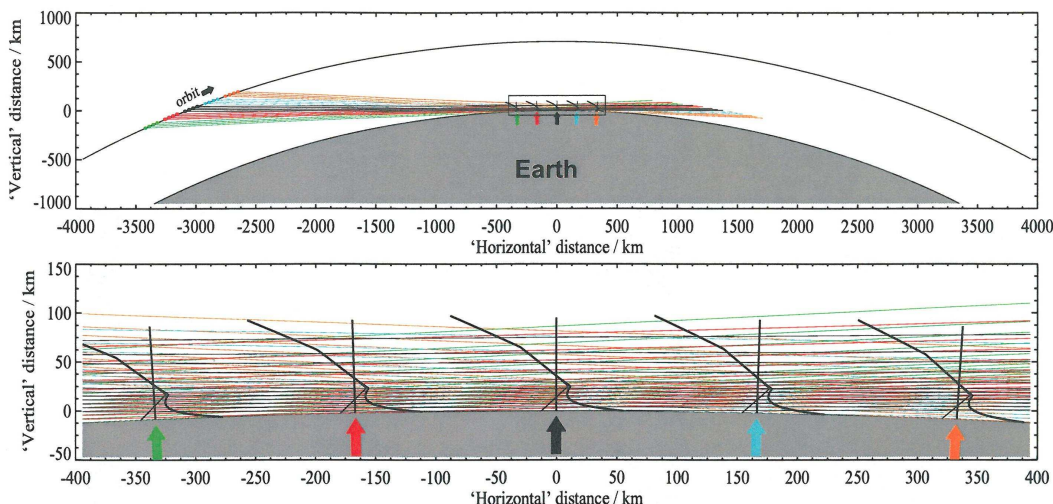


**Figure 5.4:** Illustration of the limb sounding technique by MLS. From *Waters et al.* [2004]

The EOS MLS measures water vapor ( $H_2O$ ), ozone ( $O_3$ ), carbon monoxide ( $CO$ ), hydroxyl radical ( $OH$ ), nitric acid ( $HNO_3$ ), nitrous oxide ( $N_2O$ ), hydrogen peroxy radical ( $HO_2$ ), hydrochloric acid ( $HCl$ ), chlorine monoxide ( $ClO$ ), hydrogen cyanide ( $HCN$ ), methyl cyanide ( $CH_3CN$ ), hypobromite ( $BrO$ ), sulfur dioxide ( $SO_2$ ), temperature ( $T$ ) and geopotential height. For detailed description of this data products user can refer to *Waters et al.* [2004].

### 5.3 MIPAS-IMK

The Michelson Interferometer for Passive Atmospheric Sounding (MIPAS) is a Fourier transform spectrometer for the detection of limb emission spectra in the middle and upper atmosphere. It is allocated on board of European Space Agency (ESA) satellite ENVISAT launched on 1 March 2002. Two different data products are derived from MIPAS spectra. These are the trace gas profiles operationally delivered by ESA and the *retrievals* produced by the Institute of Meteorology and Climate Research (IMK) at the Karlsruhe Research Centre, referred to as MPI in this text. In this study only the MPI data from MIPAS were used for validation.

The MIPAS measures a series of spectra, wavelength range from 4.15 microns to 14.6 microns, from different tangent heights at altitudes of between 6 and

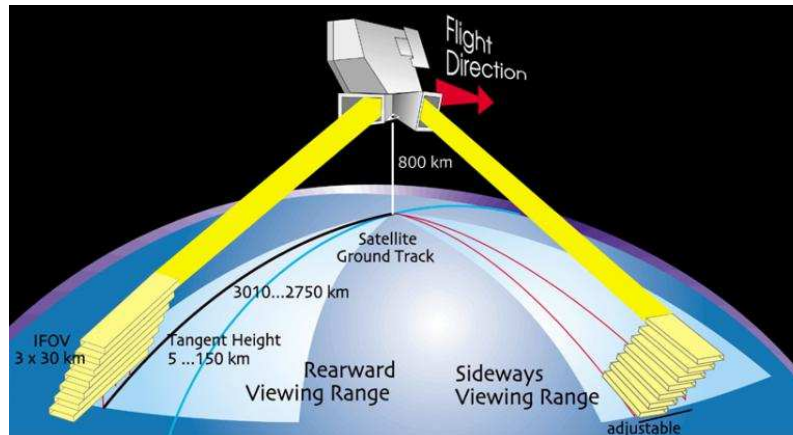


**Figure 5.5:** Illustration of the limb sounding technique by MIPAS. Source: <https://earth.esa.int/handbooks/mipas/CNTR.html>

68 km (see Figure 5.5). A typical elevation scan starts at about 50 km tangent height and descends in 3 km steps to 8 km, with the field of view of about 3 km in elevation by 30 km in azimuth. The MPI data contain profiles of  $O_3$ ,  $NO_2$ ,  $CH_4$ ,  $HNO_3$ ,  $H_2O$ ,  $N_2O$ ,  $HNO_4$ ,  $ClONO_2$ ,  $N_2O_5$ ,  $ClO$ ,  $NO$ , CFC-11 and CFC-12.

The MIPAS instrument switched off on March 26th 2004 due to a problem with moving retro-reflectors. Since then, the MIPAS instrument has been operated at reduced spectral resolution for tests in August and in December 2004. Since January 2005, MIPAS is providing measurements at a reduced spectral resolution (*Fischer et al.* [2008], *von Clarmann et al.* [2009]). Thus, the retrieval data from MIPAS are used only for validation in this study.

## 5.4 HALOE

The Halogen Occultation Experiment (HALOE) provides a long term record of important stratospheric constituents. HALOE was in operation from October 1991 to November 2005. On board of the Upper Atmosphere Research Satellite (UARS), it performed solar occultation measurements at sunrise and sunset in the infrared wavelength region. Profiles of  $O_3$ ,  $HCl$ ,  $CH_4$ ,  $H_2O$ ,  $NO$ ,  $NO_2$ ,  $HF$ , temperature and aerosol extinction have been derived routinely. During nominal operation, about 30 occultation events per day have been recorded. The latitude of tangent point location changes slowly from day to day, covering

a range of 80°N to 80°S within approximately one month. The latest data product release (version 19, abbreviated HLO hereafter) has been obtained from the NASA Langley Research Center in Hampton, Virginia.

The retrievals from HALOE are well validated stratospheric remote sounding data (see e.g. *Nazaryan et al.* [2005]). This data was used also for validation in SCOUT-O3 case study.

## 5.5 Atmospheric soundings

A radiosonde is a battery-powered telemetry instrument package carried into the atmosphere usually by a weather balloon. They measure mainly the following variables: pressure, altitude, temperature, relative humidity, geographical position, wind speed and wind direction. These measurements are transmitted by radio to a ground receiver. The balloons are only sent up twice per day, at times 00Z and 12Z. The measurement can be done up to  $\sim 35$ km altitude.

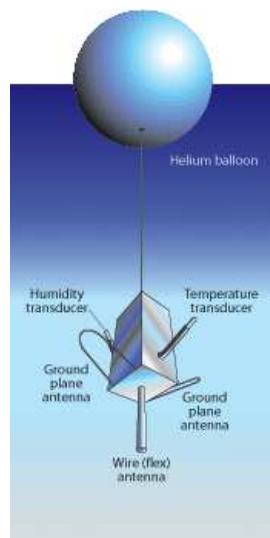


*Figure 5.6: Illustration of the Atmospheric soundings. After Hadley Center*

The sounding data provided by the data repository of the University of Wyoming, College of Engineering Department of Atmospheric Science were used for validation in the framework of this study. The list of the stations are seen in Table 5.1.

## 5.6 Observation Operator

In data assimilation the observation space differs from model space dimension. Commonly, the size of the model calculated control variables is very large while the dimension of the observation space is very small. Thus, in order to calculate

*Table 5.1: List of the radiosonde stations used in this work*

Number	Name	Hight [m]	Latitude	Longitude
60018	Guimar-Tenerife	105	28.47	-16.38
60656	DAOF Tindouf	439	27.70	-8.16
61024	DRZA Agadez	502	16.96	7.98
61052	DRRN Niamey-Aero	227	13.48	2.16
65503	DFFD Ouagadougou	306	12.35	-1.51

the cost function (see 2.3.1) or to compare the model results with observations the *projection operator* ( $H$ ) is necessary. Generally, each different kind of measurement needs its own mapping mainly due to a different measurement techniques and viewing geometry. In terms of data assimilation this projection operators is also called *Observation Operator* or simply *H-Operator*.

In the work presented here, mainly the measurements from *limb viewing* instruments were treated. In fact, the measurements which are assimilated in this study are not a direct measurements but the *retrievals*. The remote sounding instruments measure electromagnetic radiation emitted, scattered or transmitted by the earth's atmosphere. The information about trace gases are derived from the recorded spectra via different radiative transfer models ( $H_r$ ). Thus, if the true measured atmospheric state is  $y_t$  the *retrieval*  $y$  is derived by

$$\mathbf{y} = H_r(\mathbf{y}_t) + \boldsymbol{\epsilon}_r + \boldsymbol{\epsilon}_s ,$$

where  $\boldsymbol{\epsilon}_r$  is a measurement error and the  $\boldsymbol{\epsilon}_s$  is called as *systematic error*. The  $\boldsymbol{\epsilon}_r$  is also called as *random error* or *instrument noise* and considered to be Gaussian distributed. In contrast, the  $\boldsymbol{\epsilon}_s$  includes numerical errors, or errors from uncertain spectral data and can not be considered as Gaussian distributed. Therefore, including the  $\boldsymbol{\epsilon}_s$  in observation error covariance matrix of the assimilation system is not correct in terms of statistical assumptions underlying data assimilation theory. Hence, only a random component of the total retrieval error is taking in account by the assimilation. For the comprehensive information about satellite based measurements and retrieval procedures see, *e.g.*, Rodgers [2000].



## CHAPTER 6

---

### Campaign Simulations

---

Two measurement campaigns, with CRISTA-NF on board of M55 Geophysica, took place within the remote sensing experiments: SCOUT-O3 and SCOUT-AMMA, over the periods November-December 2005 and July-August 2006. SCOUT-O3 was a measurement campaign in Darwin to study the transport of trace gases with high spatial resolution through the Tropical Tropopause Layer (TTL). SCOUT-AMMA was a measurement campaign in west Africa with main objective to better document specific dynamical and chemical processes and weather systems at various key stages of the monsoon season in TTL. This two campaigns and the first assimilation results of the aircraft measurements by the improved SACADA assimilation system is described in this chapter.

### 6.1 SCOUT-O3 Tropical Aircraft Campaign

Stratospheric-Climate Links with Emphasis on the Upper Troposphere and Lower Stratosphere (SCOUT-O3) was an European Commission Integrated Project with 64 partner institutions and over 300 scientists from 19 countries. The project started in May 2004 and ran until August 2009. The aim of SCOUT-O3 was to provide predictions about the evolution of the coupled chemistry/climate system, with emphasis on ozone change in the lower stratosphere and the associated UV, as well as on climate impact. SCOUT-O3 has been structured into eight scientific activities. These are designed to provide

essential information which, when integrated, will help to predict ozone, climate and UV over the next decades. Substantial model improvements of the representation of key processes is the general goal of Activities 2 to 6. Activities 2 (Tropics), 3 (Extratropics), and 4 (UV-Radiation) focus on model improvement. Activity 6 (Chemistry-Transport-Modeling) is linked to Activities 2 to 4. Activity 5 (Chemistry and Particles) focuses on the fundamental understanding of chemical and microphysical processes and is needed by all other activities. The predictions is carried out using coupled chemistry climate models from Activity 1. Activity 7 provides a central database and ensures coordinated public relation work. (See [http://www.ozone-sec.ch.cam.ac.uk/scout\\_o3/](http://www.ozone-sec.ch.cam.ac.uk/scout_o3/) for more detail).



**Figure 6.1:** SCOUT-O3 Tropical Aircraft Campaign route. Forward transfer flights from Oberpfaffenhofen to Darwin. Source: <http://www.atmos.physik.uni-wuppertal.de>

The measurement campaign in Darwin under the framework of SCOUT-O3 took place in November/December 2005. Darwin ( $12^{\circ}\text{S}$ ,  $130^{\circ}\text{E}$ ) is the capital city of the Northern Territory of Australia and is located at the southern border of the so called “Tropical Warm Pool”. This region is considered to be one of the most important in troposphere-to-stratosphere transport (TST) (Fueglistaler *et al.* [2004]). The new remote sensing experiment CRISTA-NF has been developed to study the transport of trace gases with high spatial resolution through the tropical tropopause layer (TTL) (Hoffmann *et al.* [2009]). The instrument was mounted on the high-flying Russian research aircraft M55-Geophysica, which reaches flight altitudes up to 21 km (Stefanutti *et al.* [1999]). CRISTA-NF participated in ten M55-Geophysica flights shown in Figure 6.1. The campaign took place during the pre-monsoon season, which

**Table 6.1:** *SCOUT-O3 Campaign flights with available CRISTA-NF Level-2 data (Hoffmann et al. [2009]).*

Date of flight	Time (UTC)	Description
04.11.2005	06:02-08:07	T1 - Transfer flight Oberpfaffenhofen–Larnaca
04.11.2005	13:52-15:55	T2 - Transfer flight Larnaca–U-Taphao
13.12.2005	13:47-16:32	T9 - Transfer flight U-Taphao–Hyderabad

is characterised by a diurnal evolution of deep convective system, over the Tiwi Islands located north of Darwin, known as “Hector”. (*Keenan and Carbone [1992]*). The large-scale flow during the first half of the campaign was such that local flights sampled air masses downstream of the cold trap region over Indonesia. The campaign period also enclosed a Rossby wave breaking event transporting stratospheric air to the tropical middle troposphere and an equatorial Kelvin waves, modulating tropopause temperatures and hence the conditions for dehydration. More information about the SCOUT-O3 field campaign and its prevailing meteorological conditions can be found in *Brunner et al. [2009]* and *Hoffmann et al. [2009]*.

## 6.2 SCOUT-AMMA Campaign

AMMA is an international interdisciplinary project dealing with the West African Monsoon, its variability and its impacts on regional communities. Based on a French initiative, AMMA was built by an international scientific group and is currently funded by a large number of agencies, especially from France, UK, US and Africa. Scientists from more than 30 countries, representing more than 140 institutes are involved in AMMA. (see <http://www.amma-international.org>)

SCOUT-AMMA stratospheric aircraft, balloons and sondes campaign over West Africa took place between 26 July and 25 August 2006. This campaign was in frame of the concomitant African Monsoon Multidisciplinary Analyses (AMMA) special observing period and SCOUT-O3 African tropical activities (*Cairo et al. [2010]*).

Within this frame, the AMMA and the SCOUT-O3 European projects organized together the SCOUT-AMMA campaign, with main objective to better document specific dynamical and chemical processes and weather systems at various key stages of the monsoon season in Tropical Tropopause Layer (TTL) (*Janicot et al. [2008]*). During this campaign, five aircrafts, large number of sondes and stratospheric balloons performed measurements during the mon-

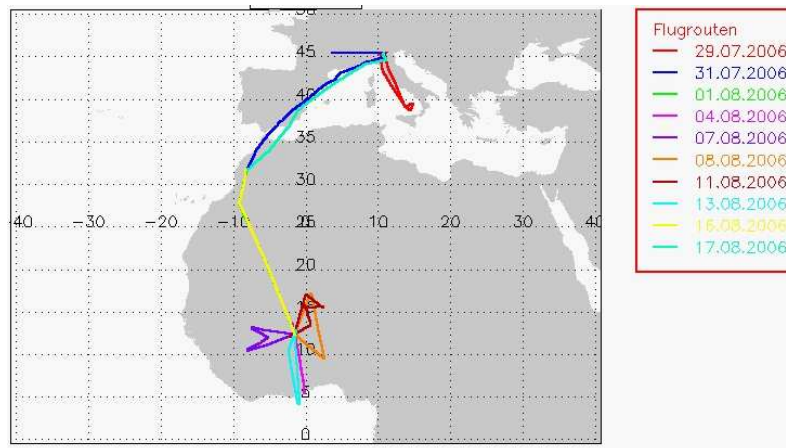


**Figure 6.2:** SCOUT-AMMA Campaign route. Source: <http://www.atmos.physik.uni-wuppertal.de>

**Table 6.2:** SCOUT-AMMA Campaign flights. Here Level-2 data are available only for dates 29.07., 31.07., 01.08., 13.08. and 17.08.2006 Weigel [2006].

Date of flight	Time (UTC)	Description
29.07.2006	05:50-09:32	Test flight over Italy
31.07.2006	09:15-13:15	Transfer flight Oberpfaffenhofen-Ouagadougou
01.08.2006	10:59-14:59	Transfer flight Marrakesh-Ouagadougou
04.08.2006	08:26-12:13	Local flight from Ouagadougou
07.08.2006	12:15-16:07	Local flight from Ouagadougou
08.08.2006	11:46-15:31	Local flight from Ouagadougou
11.08.2006	14:44-18:22	Local flight from Ouagadougou
13.08.2006	12:50-16:23	Local flight from Ouagadougou
16.08.2006	13:27-15:16	Transfer flight Ouagadougou-Marrakesh
17.08.2006	04:10-07:51	Transfer flight Marrakesh-Verona

soon season within high levels from the troposphere to the lower stratosphere.

The aircraft M55 Geophysica with CRISTA-NF instrument on-board carried out five local and four transfer flights between southern Europe and the Sahel and back (see Table 6.2, Figure 6.2). CRISTA-NF Level-2 data (Weigel *et al.* [2010]) of this flights were assimilated in this work.

### 6.2.1 West African Monsoon

Most of its annual rainfall in the Western part of the tropical African continent is during the boreal summer months from June to September. This rainy season is significant with the seasonal reversal of the winds in the lowest level of

the atmosphere and hence is called monsoon. In tropical countries the monsoon is the most important event of the seasonal cycle which has a significant impact on local agriculture and water resources (*Hall and Peyrillé* [2006], *Janicot et al.* [2008]).

As for all monsoons, the West African Monsoon (WAM) is involved in many interacting scales and physical processes shown in Figure 6.3. These processes occur due to a rapid warming of the continental surface in early summer relative to the adjacent ocean. Thus, the convective rainfall is essential for the setup of a monsoon circulation. More details of WAM development in *Hall and Peyrillé* [2006].

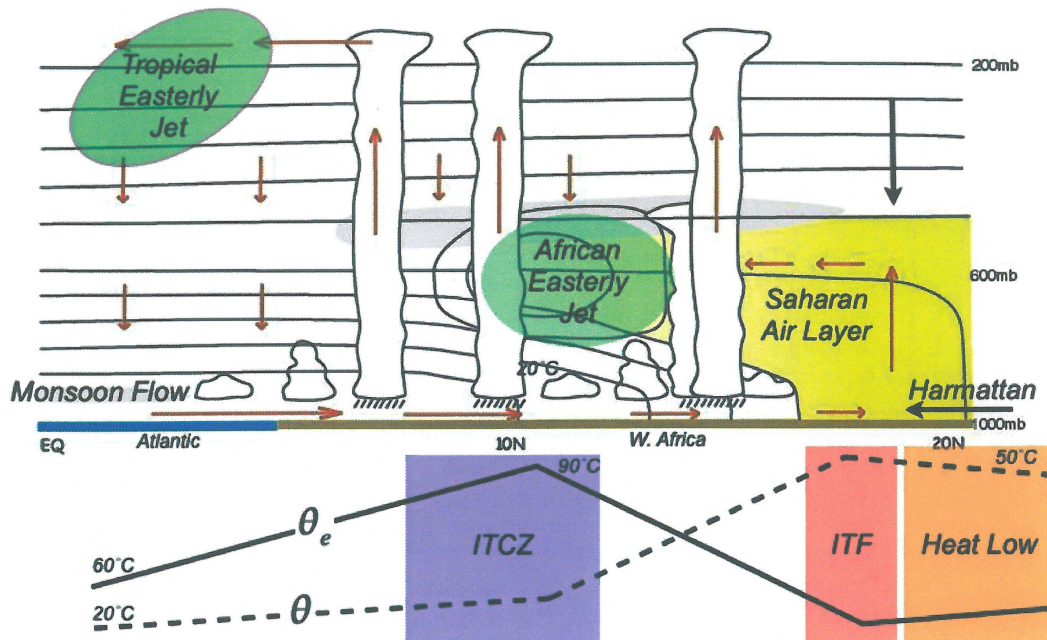


**Figure 6.3:** Schematic latitudinal section showing elements of fully developed West African Monsoon, with typical meridional profiles of uniform ( $\theta$ ) and equivalent ( $\theta_e$ ) potential temperature, inter-tropical front (ITF) and inter-tropical convergence zone (ITCZ). By *Hall and Peyrillé* [2006].

The WAM of the summer 2006 was a near-normal rainy season but with a large-scale rainfall excess north of 15°N. Compared to climatology, it was also characterized by 10-day delayed onset with convection becoming developed only after 10 July. This delay impacted the continental hydrology, vegetation dynamics, soil moisture and dust emissions. For more details reader can refer to *Janicot et al.* [2008].

### 6.3 System set-up

For the provision of the first initial values of the SACADA-runs the two-dimensional atmospheric model SOCRATES (*Brasseur et al.* [1995]) was used for the *first day* of each case study. The zonal mean volume mixing ratios of all stratospheric constituents included in the SACADA model with latitude/height distribution is the output of this 2D model. The SOCRATES output was mapped over the SACADA icosahedral grid and made a 48 hour model spin-up run to relax the chemical constituents towards their equilibrium state. These results were still relatively coarse for the assimilation of sparse, in comparison to the degree of freedom of the SACADA system and CRISTA-NF data. Thus, a *spin-up assimilation* of MLS data for the week before campaign periods was provided. The GME is initialised with ECMWF operational analysis (*Persson* [2001]) for each assimilation day.

The relative background error  $\epsilon_b$  and correlation length scales  $L_h$ ,  $L_v$  (*Elbern et al.* [2010]) for assimilation of MLS and CRISTA-NF data are listed in Table 6.3. The observation error covariance matrix  $\mathbf{R}$  has been assumed to be diagonal with the variances taken from the respective data products.

**Table 6.3:** BECM parameter settings for different kind of assimilated observation for both SCOUT-O3 and SCOUT-AMMA campaigns.

Configuration	$L_h$ (km)	$L_v$ (m)	$\epsilon_b$ (%)
MLS	450	800	40
CRISTA-NF	150	800	40

**Table 6.4:** The system set-ups for different test cases.

Tast cases	Assimilated species	Background $H_2O$
SCOUT-O3-1	$H_2O$	SACADA $H_2O$
SCOUT-O3-2	$H_2O, O_3, HNO_3, N_2O, NO_2, CH_4$	SACADA $H_2O$
SCOUT-AMMA-1	$H_2O$	ECMWF $H_2O$
SCOUT-AMMA-2	$H_2O$	SACADA $H_2O$
SCOUT-AMMA-3	$H_2O, O_3, HNO_3$	SACADA $H_2O$

Three different set-ups were tested for the SCOUT-AMMA campaign. For the test of the data assimilation system performance in first case (1) only  $H_2O$  observations, while in the second case (2) water together with other observed species ( $O_3, HNO_3$ ) were assimilated. The assimilation of only  $H_2O$  observations was performed with two different background information. In first case (1a) with  $H_2O$  ECMWF operational analysis and in the second (1b)

the  $H_2O$  field from the SACADA previous day analysis (in most cases it was the result of MLS  $H_2O$  assimilation), was used as a background information (see Table 6.4).

For the SCOUT-O3 campaign two different set-ups were tested. In the first case only  $H_2O$  observations and in the second case  $H_2O$ ,  $O_3$ ,  $N_2O$ ,  $HNO_3$ ,  $NO_2$ , and  $CH_4$  are assimilated. For the model comparison, the free model run (control run) was calculated over the period of the SCOUT-O3 campaign. The observations from MIPAS-IMK, HALOE and radiosondes were used only for validation purposes.

## 6.4 General results with $\chi^2$ -tests

The cost function evolution over the iterations for SCOUT-O3 and SCOUT-AMMA case studies with different set-ups are shown in Figures 6.4 – 6.6. In order to facilitate comparability over days the values of the cost function are divided by the number of available observations  $p$ . This kind of evaluation is also known as chi-squared test (or  $\chi^2$ -test) in statistics. In *Talagrand* [1998] is shown that in case of the *true* Background- and Observation error covariance matrices the expected value of the minimum of the cost function divided by  $p$  is 0.5.

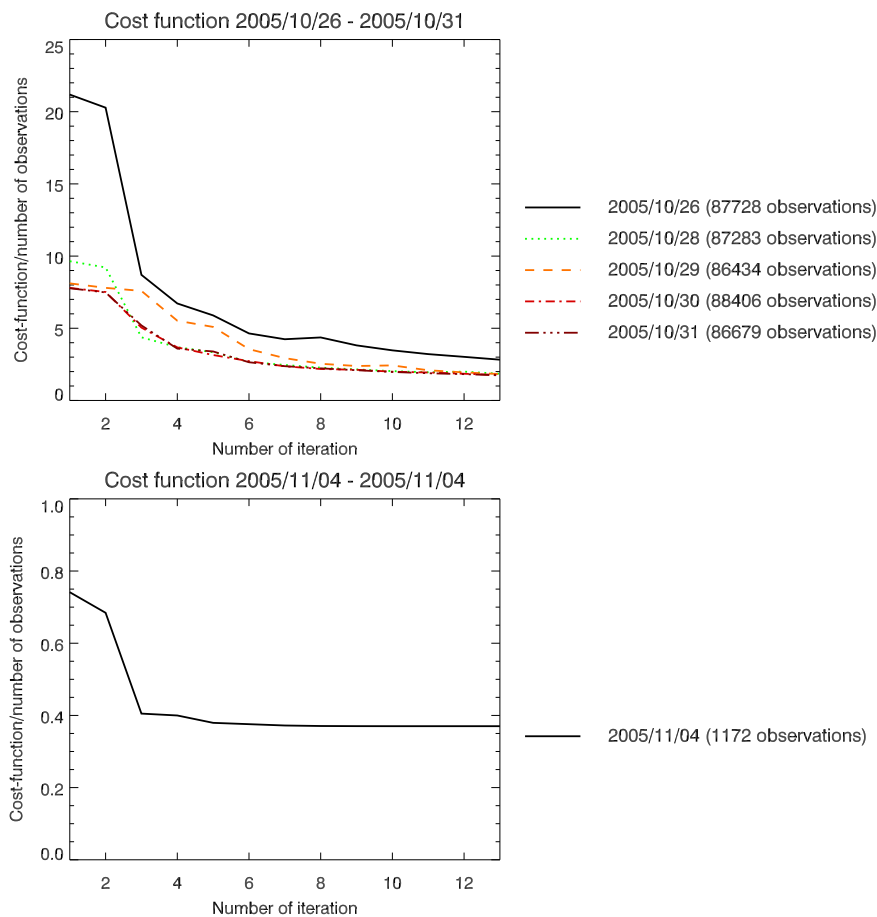


**Figure 6.4:** Evolution of the normalised cost function (cost divided by the number of observations) for configuration **SCOUT-O3-1**. Five days with assimilated MLS observations (top) and one day with assimilated CRISTA-NF observations (bottom). The x-axis gives the iteration count, and the number of observations available at a particular day is displayed at the right hand side of each plot.

The analysis cost function value  $\frac{J^a}{p}$  above the optimal value of 0.5 may indicate, among other possible causes, that the observation error margins are still too small compared to the background with its error margins, which has significantly lower costs. This is seen in the Figures 6.4 – 6.6 with the assimilated MLS observations. The convergence of  $\frac{J^a}{p}$  to the 0.5 after  $N = 12$  iterations proceed very slow there. It was tested, with more iterations further reduction of scaled cost function can be achieved. The computational time and effort should be kept reasonable. Thus, the  $N = 12$  of iterations is set to be sufficient.

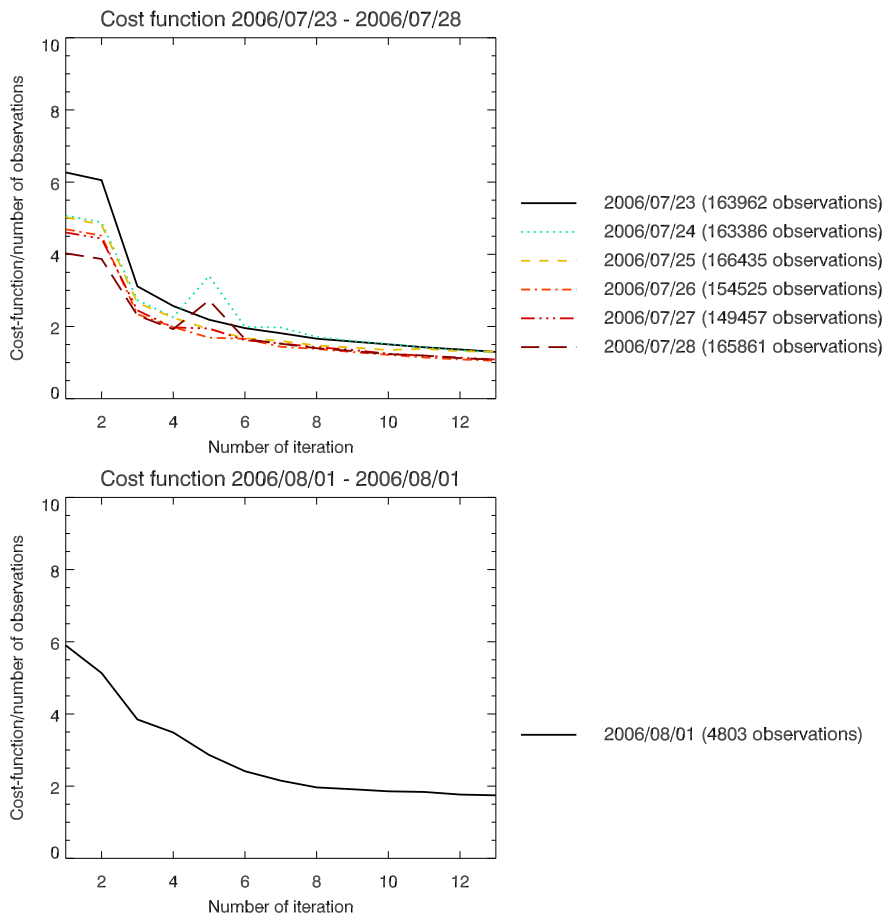


**Figure 6.5:** Evolution of the normalized cost function for configuration *SCOUT-AMMA-3*. Five days with assimilated MLS observations (top) and one day with assimilated CRISTA-NF observations (bottom). Plotting conventions as in Fig. 6.4.

On the upper panel of Figure 6.6 the costs of the assimilated MLS water observations with the SACADA previous day analysis as a background are shown.

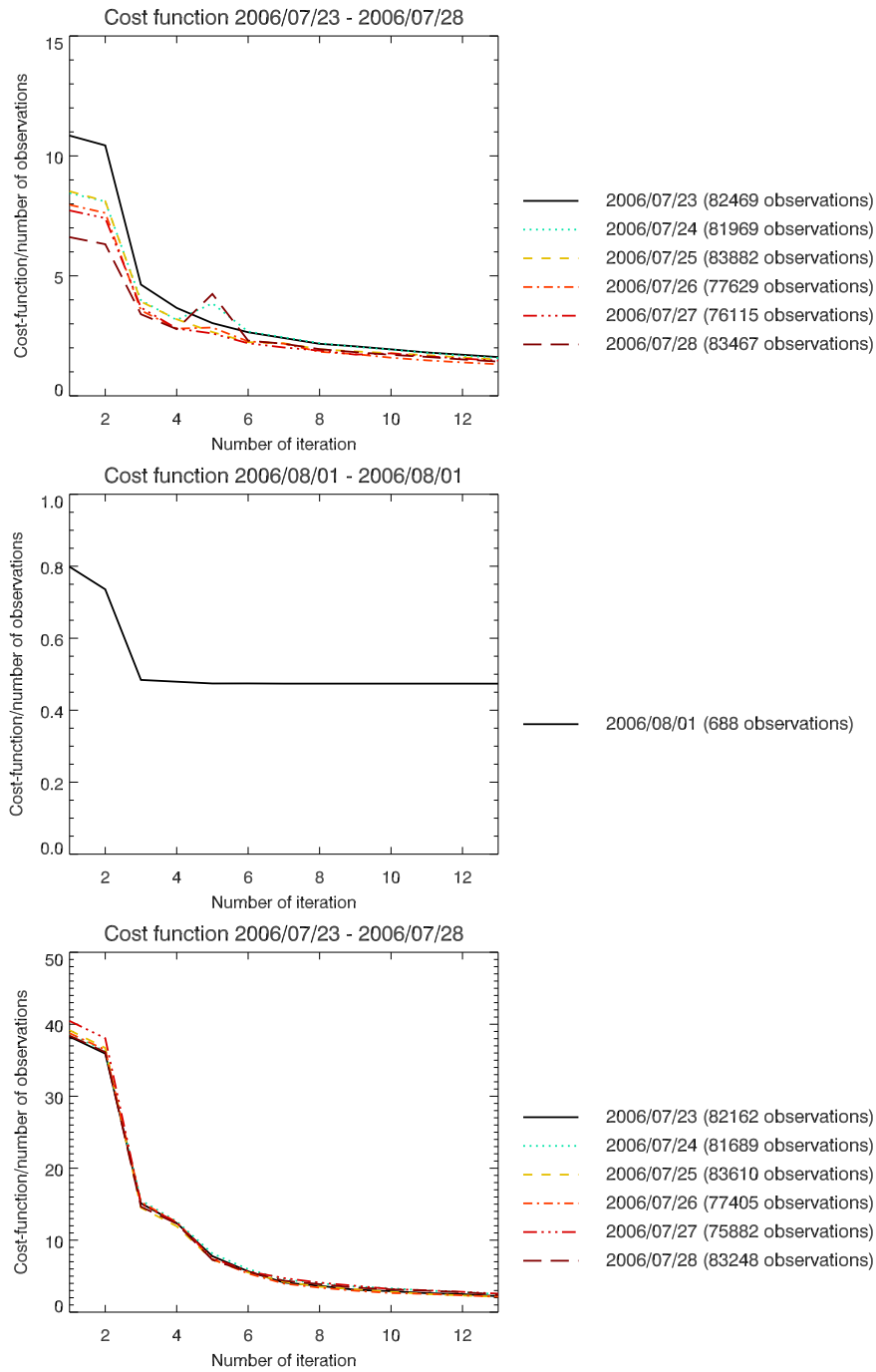


**Figure 6.6:** Evolution of the normalized cost function for configuration *SCOUT-AMMA-2* (top, middle) and *SCOUT-AMMA-1* (bottom). Five days with assimilated MLS  $H_2O$  observations (top, bottom) and one day with assimilated CRISTA-NF  $H_2O$  observations (middle). Plotting conventions as in Fig. 6.4.

It is seen that scaled costs on the *first* iteration reduces with progressing days assimilated. This value of the cost function measures the distance between the SACADA model forward run, which is actually the model forecast started with previous day analysis, and the observations weighted by the  $\mathbf{R}$  observation error covariance matrix. On the lower panel of Figure 6.6 the costs of the assimilated MLS water observations with the ECMWF  $H_2O$  operational analysis as a background is shown. The scaled costs on the *first* iteration do not vary significantly there.

Thus, it can be concluded that the  $H_2O$  analysis improves, with progressing days assimilated, compared to the ECMWF  $H_2O$  operational analysis. In the assimilated period of SCOUT-O3, October 27th is the day without observations. Therefor only model forward run is performed for this day.

## 6.5 The Campaign Analysis

### 6.5.1 Introduction to $H_2O$ , $O_3$ and $HNO_3$

**Water vapor** ( $H_2O$ ) is the most important natural greenhouse gas and plays an important role in the formation of clouds and chemistry of both troposphere and stratosphere (*World Meteorological Organization* [2006]). The main source of  $H_2O$  in the atmosphere is the evaporation at the earth surface. Due to dehydration by freezing of ice crystals few  $H_2O$  enters into the stratosphere (*Danielsen* [1982]).

The assimilation of the  $H_2O$  in the stratosphere has not as long a history as in the troposphere. This became more important because of its importance in the radiation budget. Also, it provides information on the atmospheric circulation, as it is a source of  $HO_x$  (involved in the catalytic destruction of the ozone) and is a constituent of the Polar stratospheric Clouds involved in polar ozone loss (*Dessler* [2000]). The water vapor mixing ratio varies by many orders of magnitude, from few percent (by mass) in the tropical lower troposphere to few parts per million (by mass or volume) in the stratosphere. In the stratosphere itself, the water vapor mixing ratio varies little, from  $\sim 2$  ppmv near the tropopause to  $\sim 8$  ppmv near the stratopause. The large variation by different altitudes makes difficult to specify a control variable suitable for use in the models that span this region (*Lahoz et al.* [2007]). This drastic change of  $H_2O$  concentration in the UTLS region leads to a strong vertical gradient, which is a challenge for data assimilation.

**Ozone** ( $O_3$ ) in the stratosphere is important for its well known shield function from harmful solar UV-B radiance for the earth's surface. In addition, it plays an important role for the temperature structure of the stratosphere and the circulation (*Seinfeld and Pandis* [2006]). Hence, an improvement in the accuracy of the ozone profiles can lead to more accurate temperature representation. Ozone is mainly originated in the lower tropical stratosphere. In the stratosphere, ozone has a life-time ranging from months (lower stratosphere) to less than 1 day (upper stratosphere) (*Dessler* [2000]). The stratosphere troposphere exchange of the  $O_3$  is still not well quantified (*Denman et al.* [2007]) and is a subject of scientific interest.

**Nitric acid** ( $HNO_3$ ) is a very water soluble, acidic gas. In the atmosphere it is formed by the conversion of nitrogen monoxide into nitrogen dioxide, and ultimately into nitric acid.  $HNO_3$  belongs to the  $NO_y$  (reactive odd nitrogen) species and plays a main role in the formation of Polar Stratospheric Clouds

(*Toon et al.* [1986]) and cirrus clouds. Similar to the  $O_3$ , the highest  $HNO_3$  mixing ratios are found in the lower stratosphere (*Murcray et al.* [1968]).

### 6.5.2 The SCOUT-O3 Campaign

Improvement of the SACADA assimilation system, by its horizontal and vertical grid refinement together with revision and extension of the chemistry mechanism, is done for study high resolution aircraft measurements. The mean profiles shown on Figures 6.7 – 6.10 representing the good model skill to assimilate the high resolution data. The profiles of different species zonally averaged over five latitude bands are presented in Figures 6.7 – 6.13. The profile data within the respective latitude ranges and the adjacent model layers are averaged to obtain the corresponding mean profile value. The averaged altitude intervals, from some hundred meters - up to 4 km (above 22 km altitude), are well comparable to the vertical resolution of CRISTA-NF and MLS measurements. The mean retrieved profiles are plotted together with mean error margins (red), the corresponding model analysis (blue) and the control run (black) data. The standard deviation of the averaged observation profiles are presented with gray shaded areas on the plots.

The mean  $H_2O$  analysis profiles for SCOUT-O3-2 show a good agreement with the CRISTA-NF data (Fig. 6.7). The small negative bias towards high mixing ratios in low altitudes (below 150 hPa) is mainly caused by a large error margins of the observations. This is also seen in the  $H_2O$  profiles of MLS (Fig. 6.8). Note, that some MLS profiles were sorted out because of data quality (*Nathaniel et al.* [2005]). The MLS tend to measure higher mixing ratios of  $H_2O$  (Fig. 6.8) in tropics below 250 hPa altitude compared to CRISTA-NF (Fig. 6.7) for the period of SCOUT-O3 campaign. The MIPAS-IMK (Fig. 6.13) measures lower water concentrations below 130hPa, especially in tropics, than the model analysis of assimilated MLS water shows. The HALOE profiles present only in altitude above 11 km. In this range SACADA analysis is in a very good agreement with not assimilated HALOE  $H_2O$  retrievals (Fig. 6.11).

The mean  $O_3$  analysis profiles for SCOUT-O3-2 show a perfect compliance with both, the assimilated MLS (Fig. 6.9) and not assimilated HALOE (Fig. 6.12) data. The very small negative bias is visible above 0.4 hPa, especially in tropics.

In Figure 6.10 the mean profile of assimilated  $HNO_3$  for SCOUT-O3-2 is shown. The analysis is in a good agreement with MLS profiles in altitude 210 - 2 hPa, except tropics where a negative bias of analysis is seen. The negative

bias is also above 2 hPa area, which is marked by large error bars of MLS, up to 60% of the concentrations, similar to the tropics. However, in most of the cases analysis is within the error range of the observations.

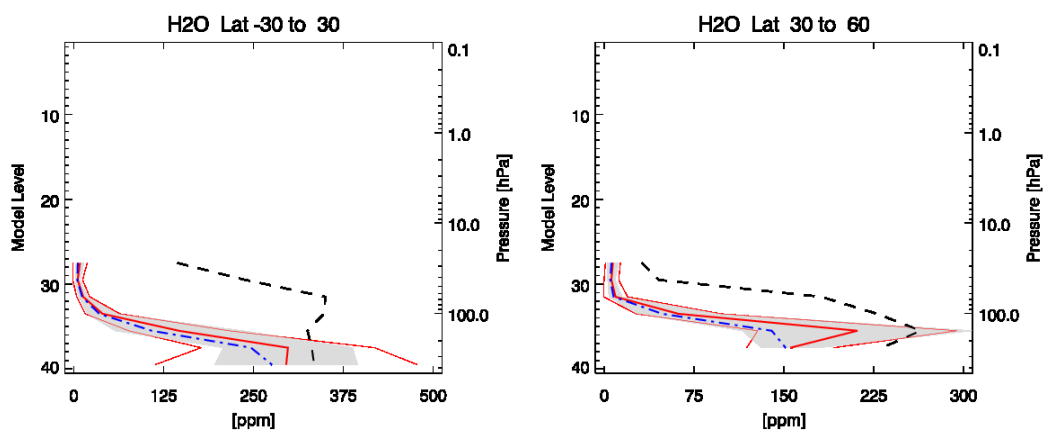


*Figure 6.7:*  $H_2O$  mean profiles from 4 November 2005 for configuration *SCOUT-O3-2*. *CRISTA-NF* (*CNF* on plots) retrieved profile values (assimilated) together with their error bars, separated by  $30^\circ$  latitude belts ( $60^\circ$  in tropics), are given in red, the control run values: black dashed line, the analysis values: dash-dotted blue line. The grey-shaded area indicates values within the standard deviation of observations. The profile values are given in ppm. The pressure on the right border gives only approximately values, the exact pressure values corresponding to model levels are listed in Table A.1.

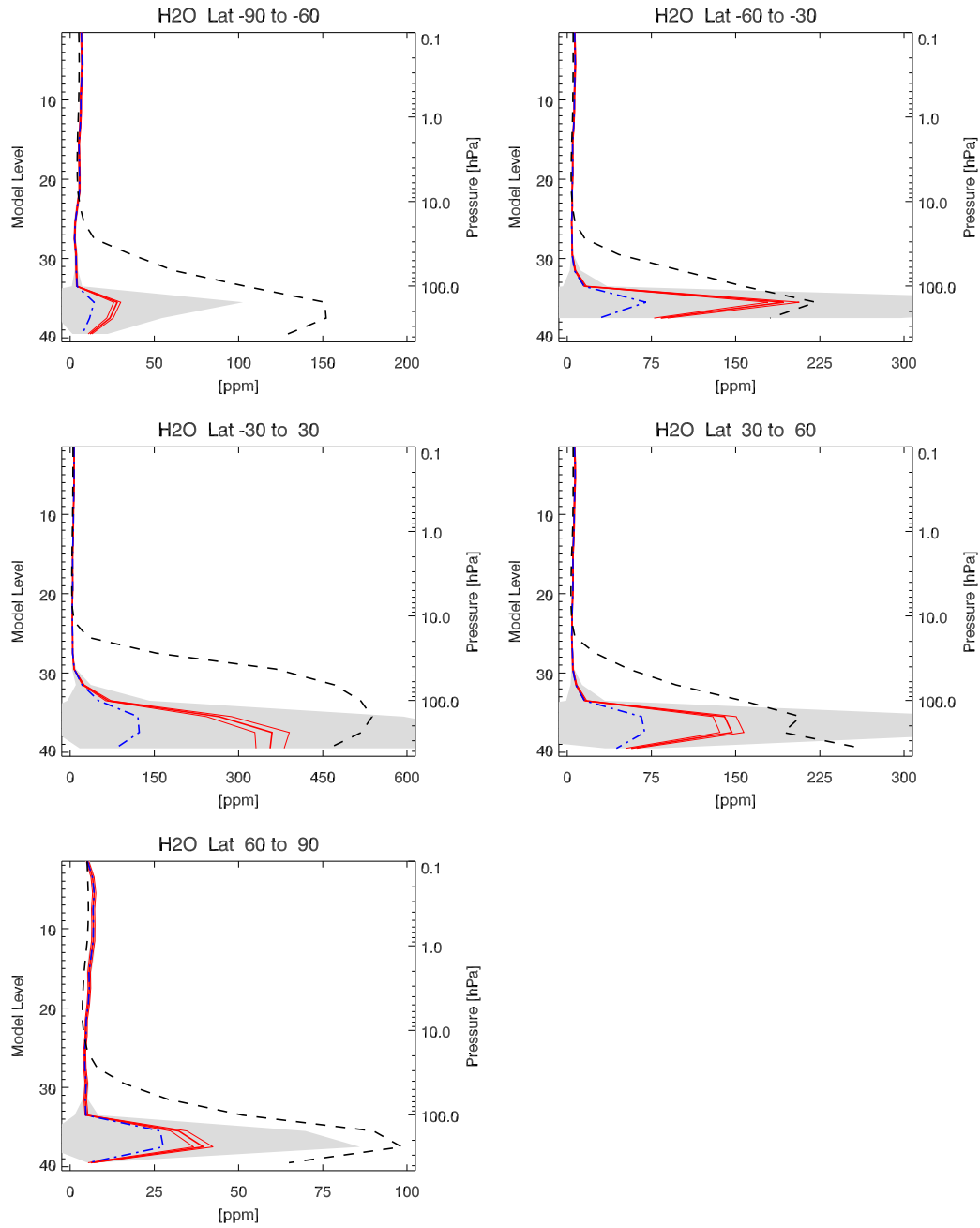


**Figure 6.8:**  $H_2O$  mean profiles from 4 November 2005 for configuration *SCOUT-O3-2*. MLS retrieved profile values (assimilated) together with its error bars are given in red, the control run values: black dashed line, the analysis values: dash-dotted blue line. Plotting conventions as in Fig. 6.7

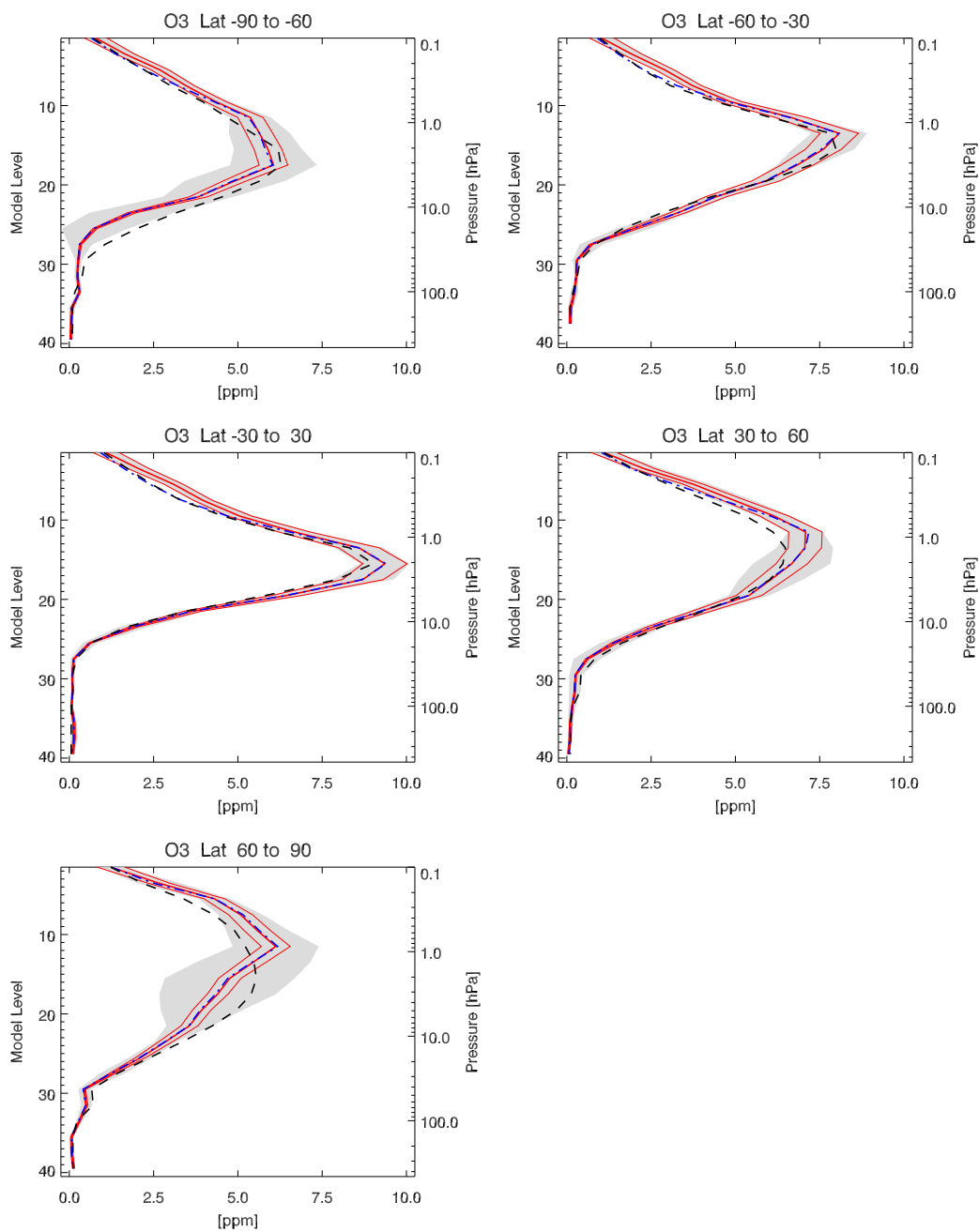


**Figure 6.9:** O<sub>3</sub> mean profiles from 4 November 2005 for configuration *SCOUT-O3-2*. MLS retrieved profile values (assimilated) together with its error bars are given in red, the control run values: black dashed line, the analysis values: dash-dotted blue line. Plotting conventions as in Fig. 6.7

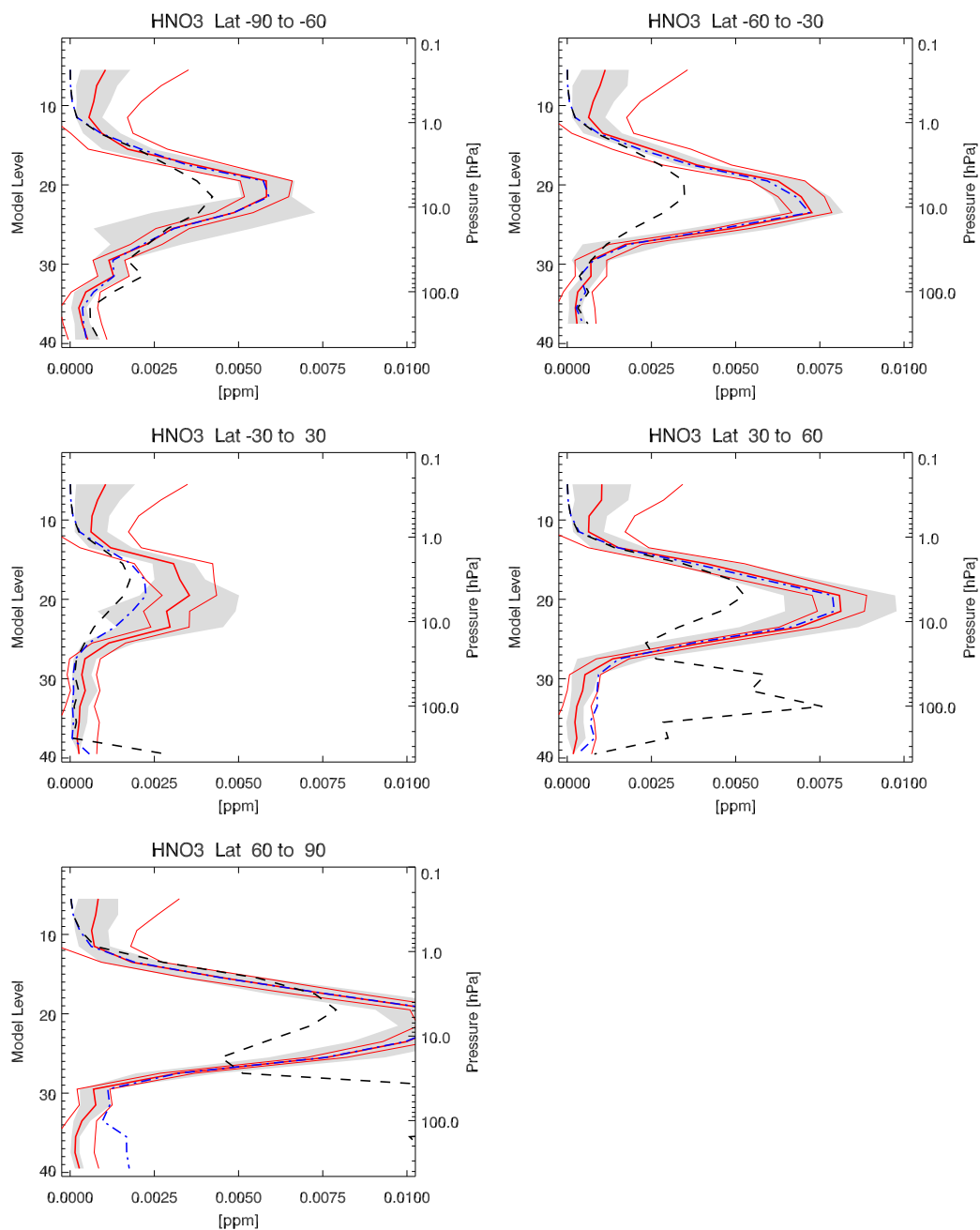


**Figure 6.10:**  $\text{HNO}_3$  mean profiles from 4 November 2005 for configuration *SCOUT-O3-2*. MLS retrieved profile values (assimilated) together with its error bars are given in red, the control run values: black dashed line, the analysis values: dash-dotted blue line. Plotting conventions as in Fig. 6.7

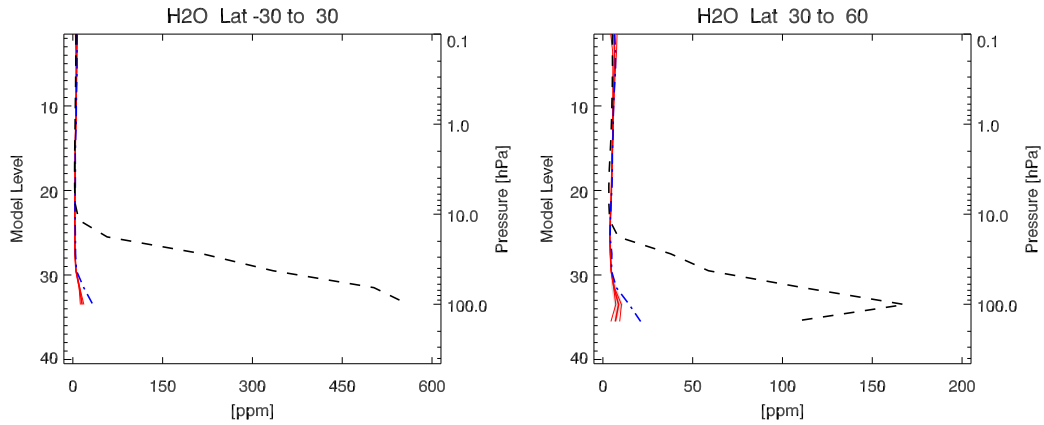


**Figure 6.11:**  $H_2O$  mean profiles from 4 November 2005 for configuration **SCOUT-O3-2**. HALOE retrieved profile values (not assimilated) together with their error bars are given in red, the control run values: black dashed line, the analysis values: dash-dotted blue line. Plotting conventions as in Fig. 6.7

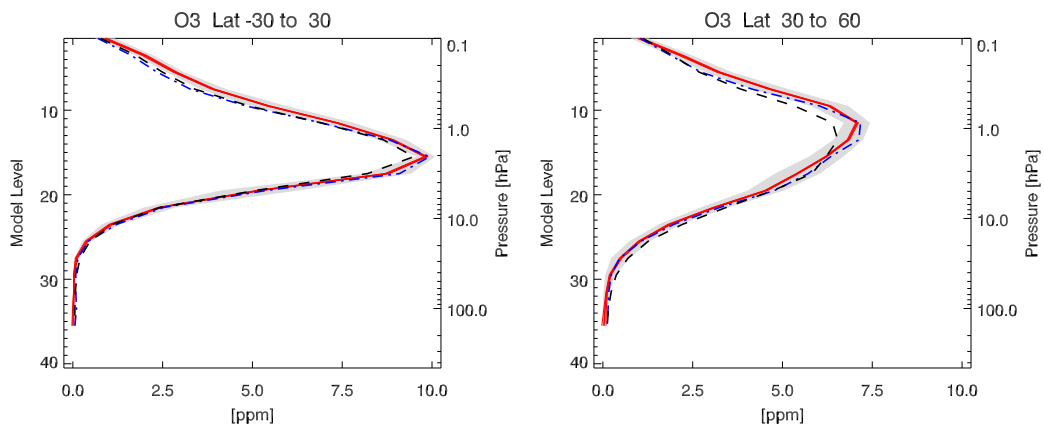


**Figure 6.12:**  $O_3$  mean profiles from 4 November 2005 for configuration **SCOUT-O3-2**. HALOE retrieved profile values (not assimilated) together with its error bars are given in red, the control run values: black dashed line, the analysis values: dash-dotted blue line. Plotting conventions as in Fig. 6.7

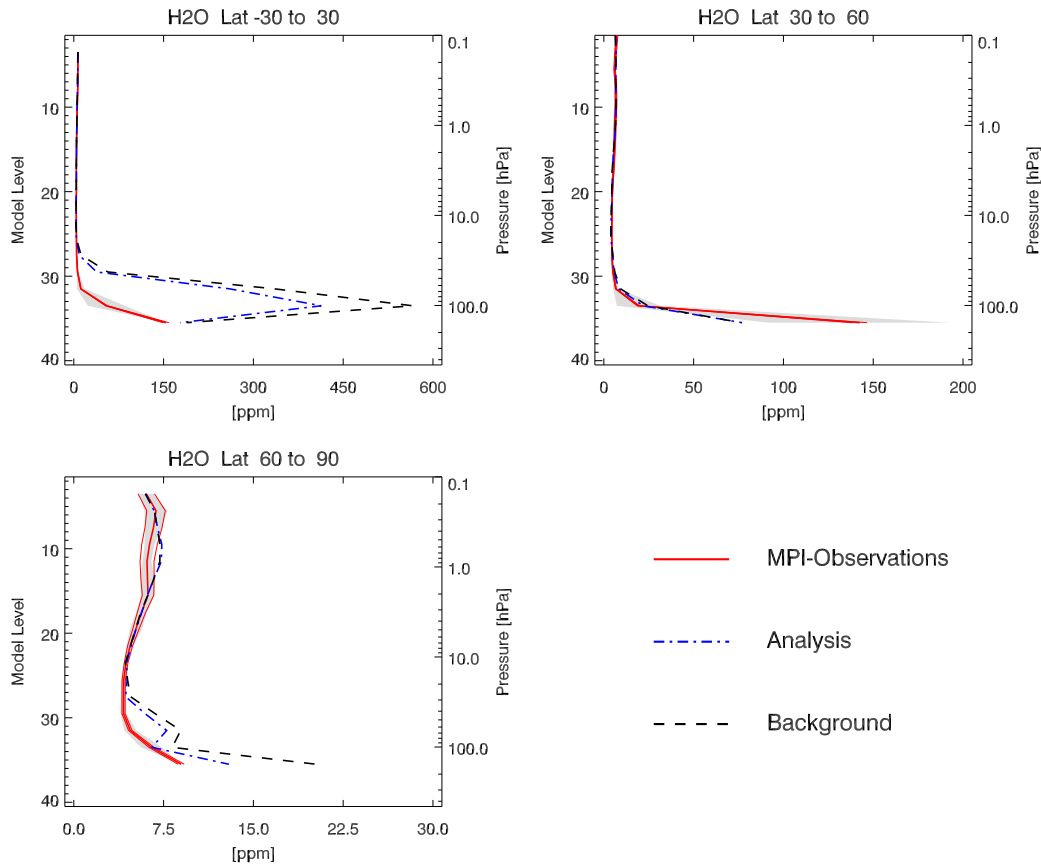


**Figure 6.13:**  $H_2O$  mean profiles from 6 November 2005 for configuration **SCOUT-O3-1**. MIPAS-IMK retrieved profile values (not assimilated) together with its error bars are given in red, the control run values: black dashed line, the analysis values: dash-dotted blue line. Plotting conventions as in Fig. 6.7

The north-south cross-sections of the zonal wind  $u$  component of the GME meteorological driver in SACADA is shown on the Figure 6.14. The zonal wind is taken at the longitude of Darwin (about  $131^\circ$  E) for 4th November and 13th December 2005, respectively. The wind structure is in a good agreement with the winds observed during the SCOUT-O3 campaign (*Brunner et al.* [2009]). Southern Hemisphere double jet structure is caused by a series of Rossby wave breaking events detected in November (Fig. 6.14, left). The strong stratospheric winds, up to  $80\text{m/s}$ , in high altitudes above 2 hPa (corresponding the model level 10) is typical for December (Fig. 6.14, right) and also detected by the Superconducting Submillimeter-Wave Limb-Emission Sounder (SMILES) in December 2009 (*Baron et al.* [2013]).

The assimilated water vapor at 138 hPa, case SCOUT-O3-2, from 4th November 2005 is compared to the control run at the same height level in Figure 6.15.

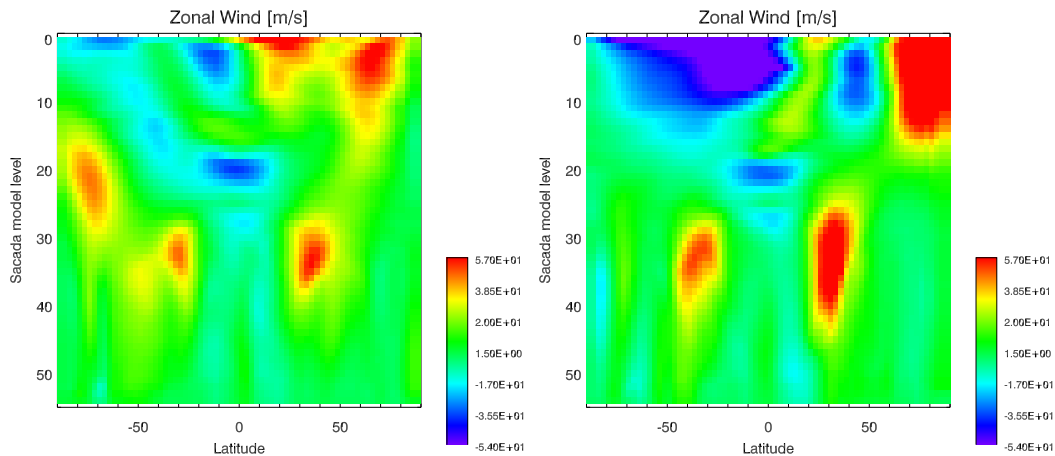


**Figure 6.14:** North-south cross-sections of the zonal wind  $u$  component at the longitude of Darwin ( $131^\circ E$ ) for 4th November (left) and 13th December 2005 (right).

This height level is the troposphere stratosphere transition region in tropics and belongs to the stratosphere in the pole areas (*Gottelman and de F. Forster* [2002], *Seinfeld and Pandis* [2006]). The benefit of the 4D-Var is clearly seen on the Figure. The high positive bias from CRISTA-NF observations, especially in tropics, of the control run (bottom) is also seen in left panel of Figure 6.7. On the left panel of Figure 6.16, in the model analysis the high convective activities are detected in the region north of Darwin. The analysis increment together with available observations on the model level 30, corresponding to 138 hPa is shown in Figure 6.16. The CRISTA-NF observations from 4 November 2005, first two transfer flights, are presented in the right panel of Figure 6.16. The measurements of the first flight, Oberpfaffenhofen to Larnaca, are taken between 06:02 and 8:07 UTC. The measurements of the second flight, Larnaca to Dubai, are taken between 13:52 and 15:55 UTC (*Hoffmann et al.* [2009]). The analysis increment is at 24:00 UTC (Fig. 6.16, left). Thus, in the time-span between observations and the analysis presented in the Figure some dynamical and chemical processes are visible, via changed shape of the increment. In the region over Italy the increment is more smoother and over Saudi Arabia is transported in North, North-East direction across sub-tropical jet stream. In the Figure 6.17 the  $O_3$  analysis (left) together with MLS  $O_3$  observations (right) on the model level 30, corresponding to 138 hPa is shown. The analysis perfectly matches the observations and shows fine structured  $O_3$  field.

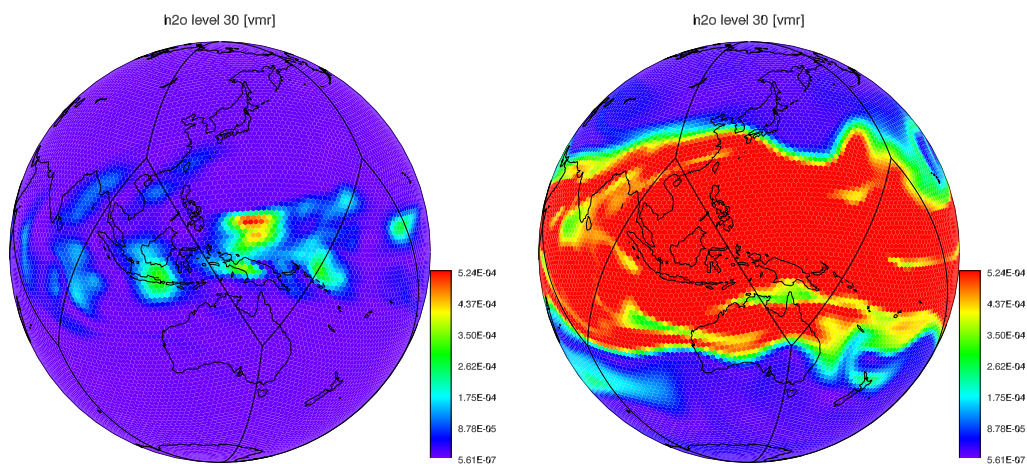


**Figure 6.15:** *SCOUT-O3-2* water vapor analysis (top) and control run (bottom) for 4 November 2005 at model level 30, corresponding to 138 hPa (about 14 km altitude). The high positive bias of the control run is also seen on Figure 6.7

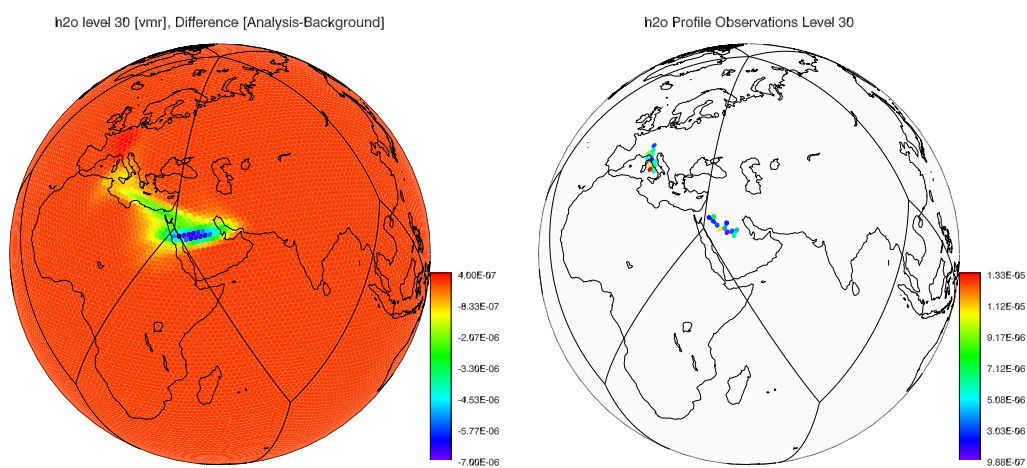


**Figure 6.16:** *SCOUT-O3-2* water vapor analysis increment (analysis-background, left) and *CRISTA-NF* H<sub>2</sub>O observations (right) for 4 November 2005 at model level 30, corresponding to 138 hPa (about 14 km altitude).

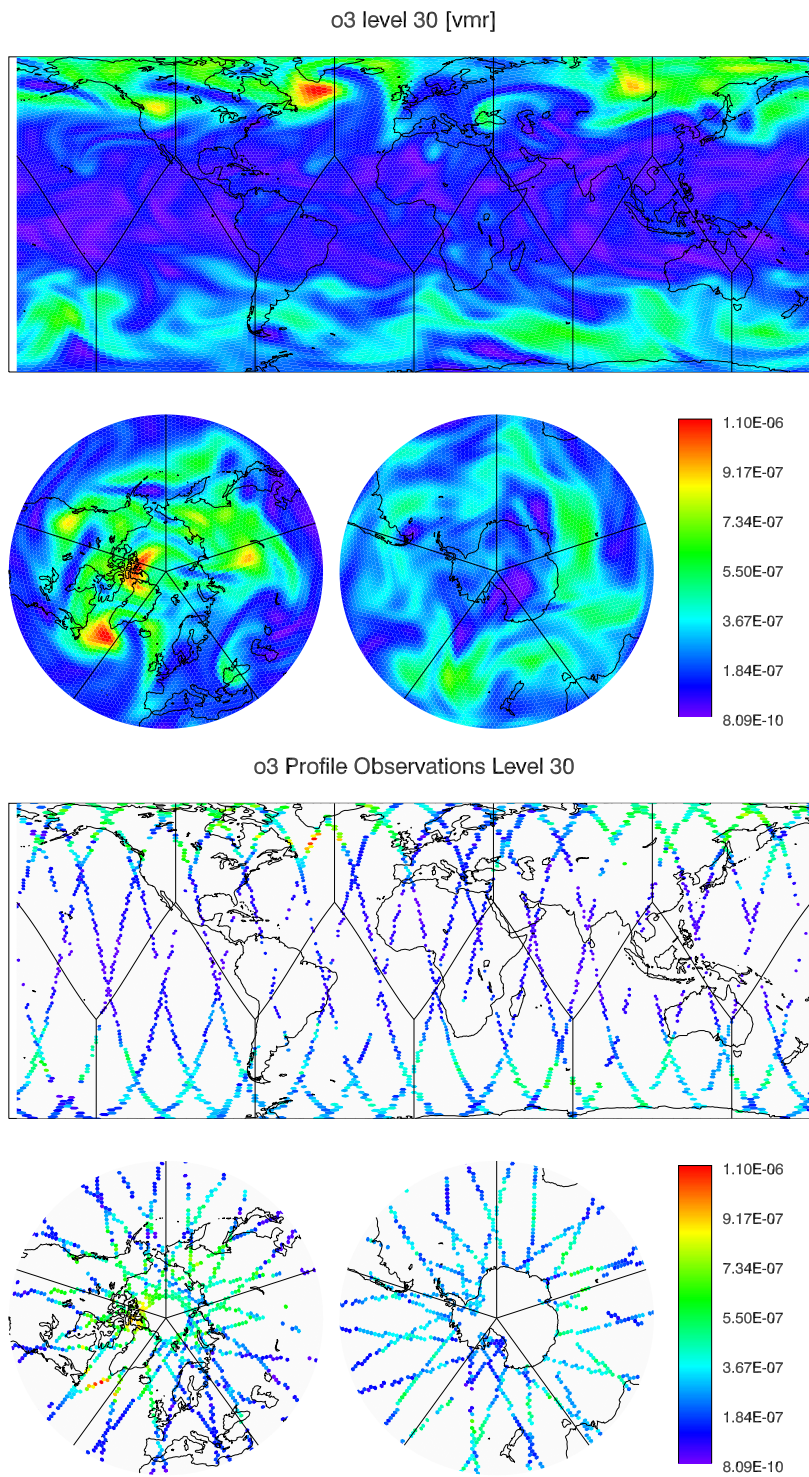


**Figure 6.17:** *SCOUT-O3-2* ozone analysis (top) and *MLS O<sub>3</sub>* observations (bottom) for 4 November 2005 at model level 30, corresponding to 138 hPa (about 14 km altitude).

### 6.5.3 The SCOUT-AMMA Campaign

The aircraft measurements from SCOUT-AMMA Campaign was assimilated, as a second test case to validate the improved assimilation system performance. The results are validated with assimilated MLS retrievals and not assimilated data from radiosondes. The assimilation results compared with the observations and the background are shown in Figures 6.18–6.19. Note, that the back-

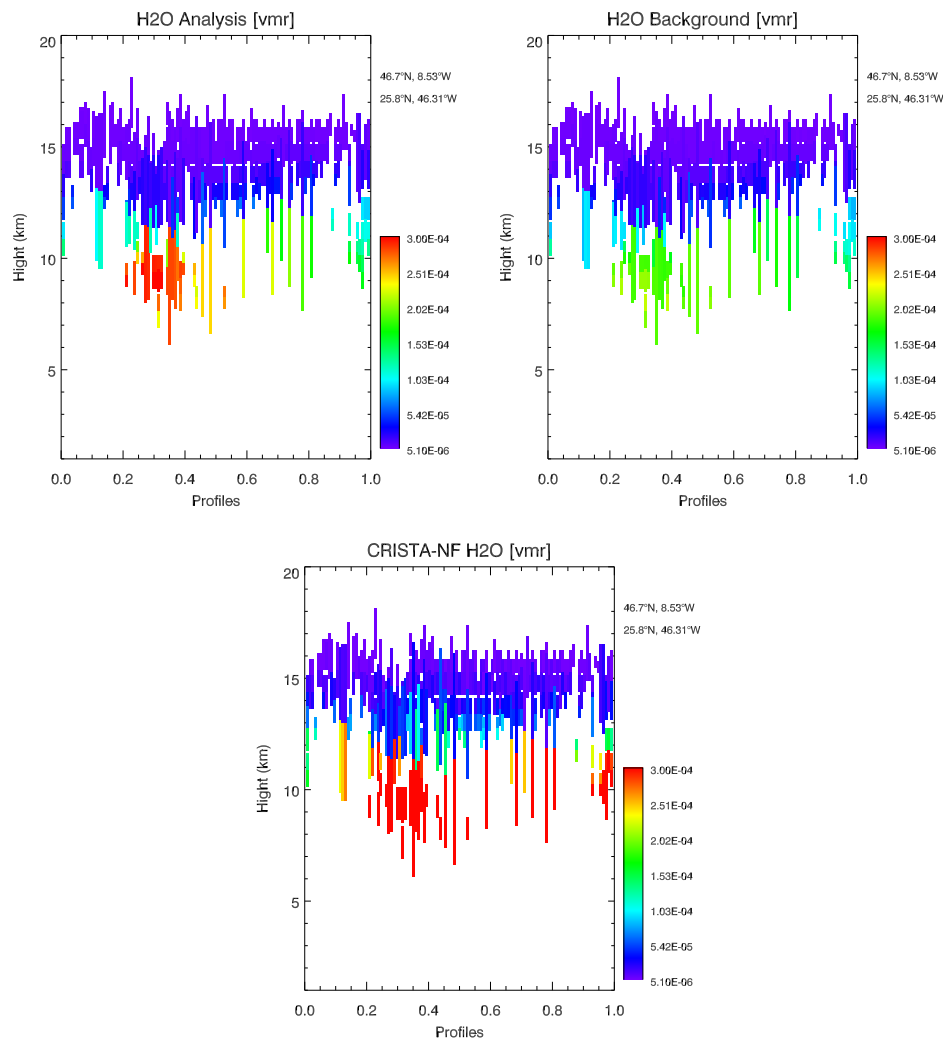


**Figure 6.18:**  $H_2O$  Profiles from 13.08.2006 along the flight route (see Figure 6.2) for configuration *SCOUT-AMMA-3*. The analysis result (top left), background values (top right) and CRISTA-NF retrievals (bottom), with same scale. Model levels together with corresponding heights and pressure are listed in Table A.1

ground here is the previous day analysis and not the *control run* as it was in

Figures of section 6.5.2. In Fig. 6.18 the SCOUT-AMMA-3 CRISTA-NF  $H_2O$  from 13 August 2006, a local flight from Ouagadougou, with corresponding background and analysis are presented. The analysis is in a good agreement with observations above 10 km altitude. The negative analysis bias in lower altitudes can be connected with the few number of assimilated observations and the relatively large observation errors, also in comparison to errors of the  $O_3$  and  $HNO_3$  together assimilated in case SCOUT-AMMA-3. This is a problem of preconditioning of species with anti-correlation in stratosphere and troposphere, with orders of magnitude of concentrations. It can be expected

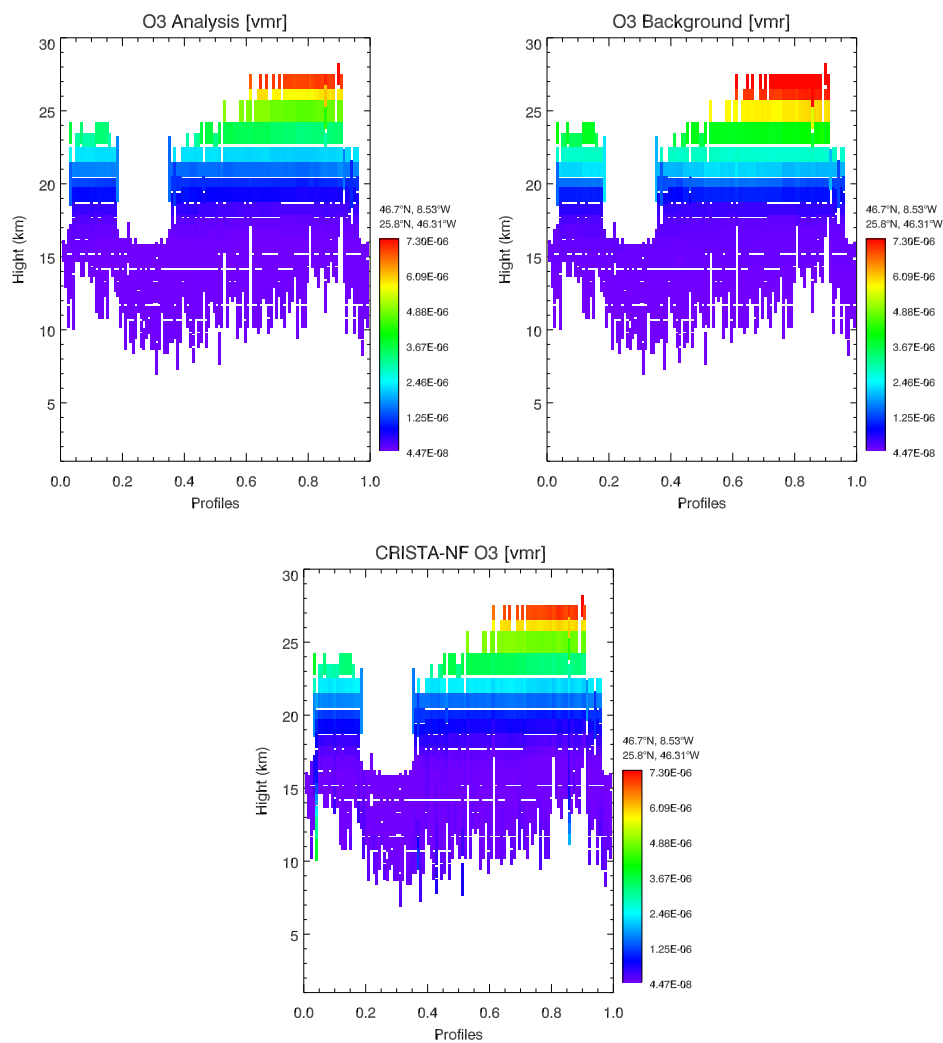


**Figure 6.19:**  $O_3$  Profiles from 13.08.2006 along the flight route for configuration SCOUT-AMMA-3. The analysis result (top left), background values (top right) and CRISTA-NF retrievals (bottom), with same scale.

that a more sophisticated estimation of the BECM parameters used in the diffusion scheme will further improve the quality of analysed water fields. The  $O_3$  analysis from 13 August 2006 is fitting perfectly the CRISTA-NF  $O_3$  observations (Fig. 6.19). The small negative bias of the background field in altitude range between 20-26 km is well corrected in analysis by 4D-Var assimilation.

In order to assess the SACADA analysis skills to assimilate the high resolution data the profiles of different species zonally averaged over five latitude bands are presented in Figures 6.20 – 6.24. The plotting conventions are described

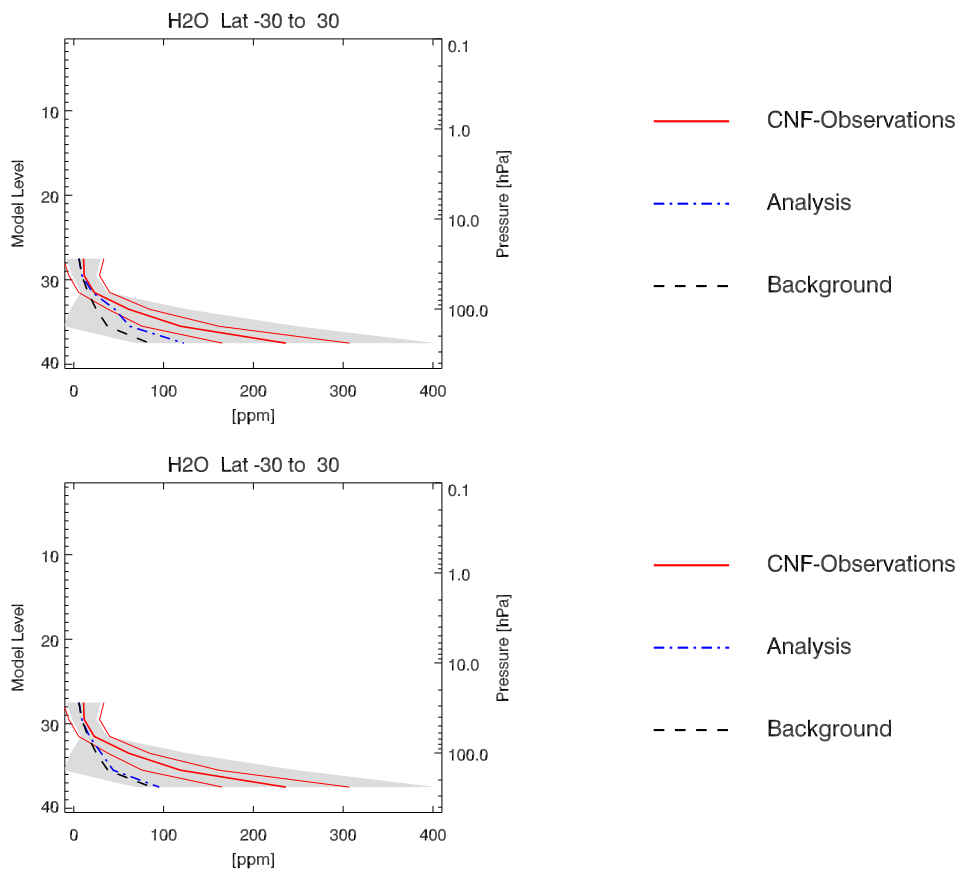


**Figure 6.20:**  $H_2O$  mean profiles from 1.08.2006 for configuration **AMMA-SCOUT-2** (top) and **AMMA-SCOUT-3** (bottom). CRISTA-NF retrieved profile values (assimilated) together with their error bars are given in red, the background values: black dashed line, the analysis values: dash-dotted blue line. The grey-shaded area indicates values within the standard deviation of observations.

in detail in the beginning of section 6.5.2. The assimilated only CRISTA-NF  $H_2O$  (top), case SCOUT-AMMA-2, and  $H_2O$  together with  $O_3$  and  $HNO_3$  (bottom), case SCOUT-AMMA-3, is shown in Fig. 6.20. It is seen, that the assimilation of only  $H_2O$  observations improves for the analysis. This is also

seen from reduction of the cost function in both cases, see Fig. 6.6 (middle) and Fig. 6.5 (bottom), respectively. Thus, in case of assimilation of  $H_2O$  together with other species more iterations in minimization loop has to be undertaken. The mean  $O_3$  analysis is in a good agreement with CRISTA-NF observations (Fig. 6.21, top). The small negative bias seen in low altitudes up to 140 hPa. The negative bias is also seen for mean CRISTA-NF  $HNO_3$  (Fig. 6.21, bottom) profile up to 180 hPa and above 40 hPa. In the range between mean model analysis is in full compliance with the mean observations.

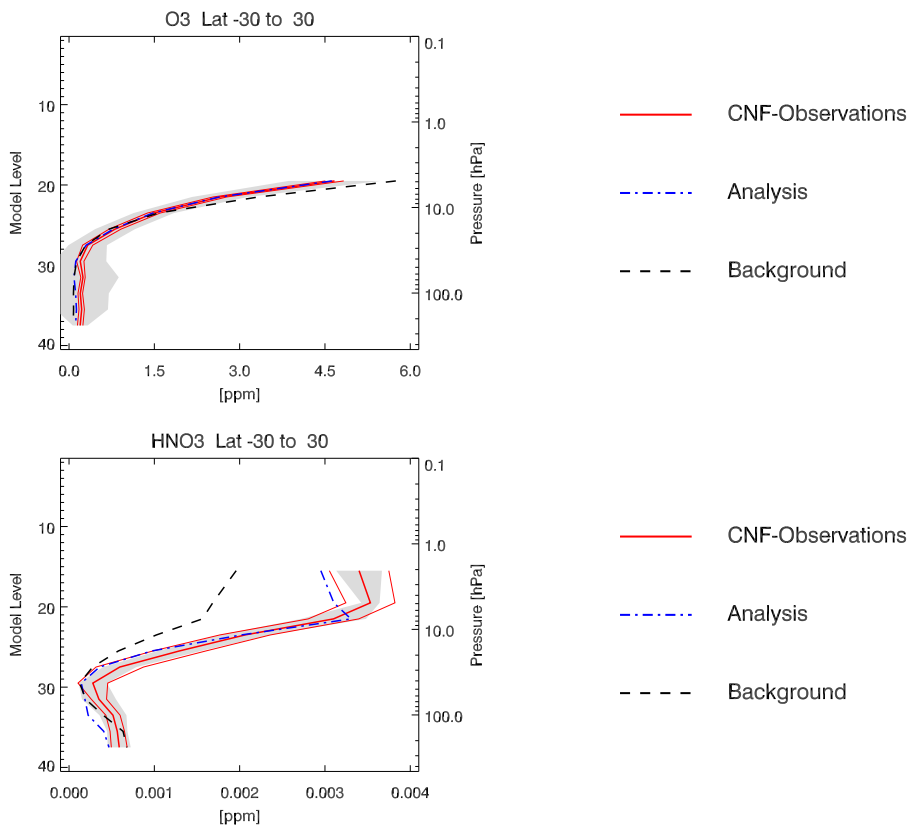


**Figure 6.21:**  $O_3$  (top) and  $HNO_3$  (bottom) mean profile values from 1 August 2006 for configuration **AMMA-SCOUT-3**. CRISTA-NF retrieved profile values (assimilated) together with their error bars are given in red, the background values: black dashed line, the analysis values: dash-dotted blue line. Plotting conventions as in Fig. 6.20

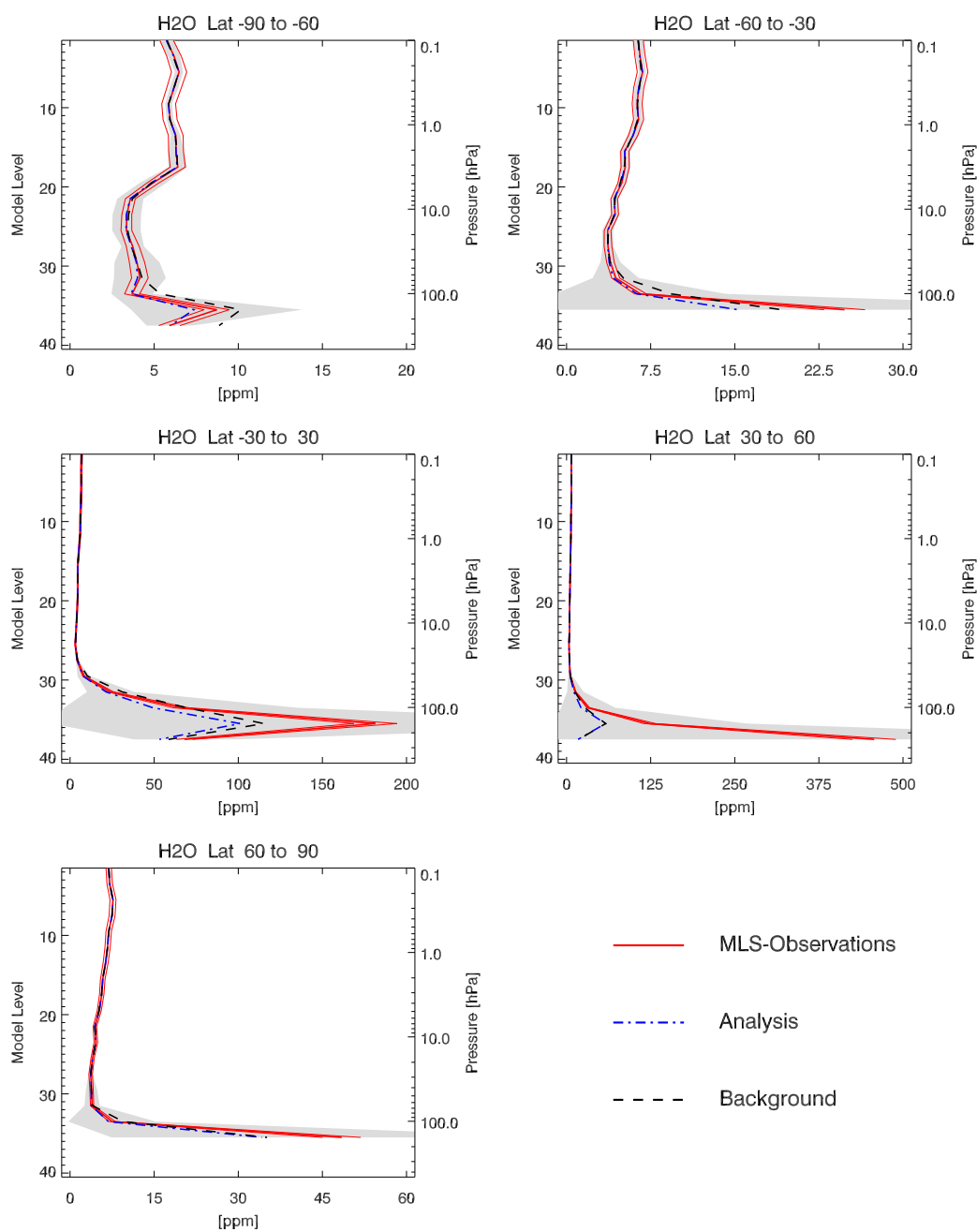


**Figure 6.22:** *MLS H<sub>2</sub>O mean profile values from 1 August 2006 for configuration AMMA-SCOUT-2. MLS retrieved profile values (assimilated) together with their error bars are given in red, the background values: black dashed line, the analysis values: dash-dotted blue line. The grey-shaded area indicates values within the standard deviation of observations.*

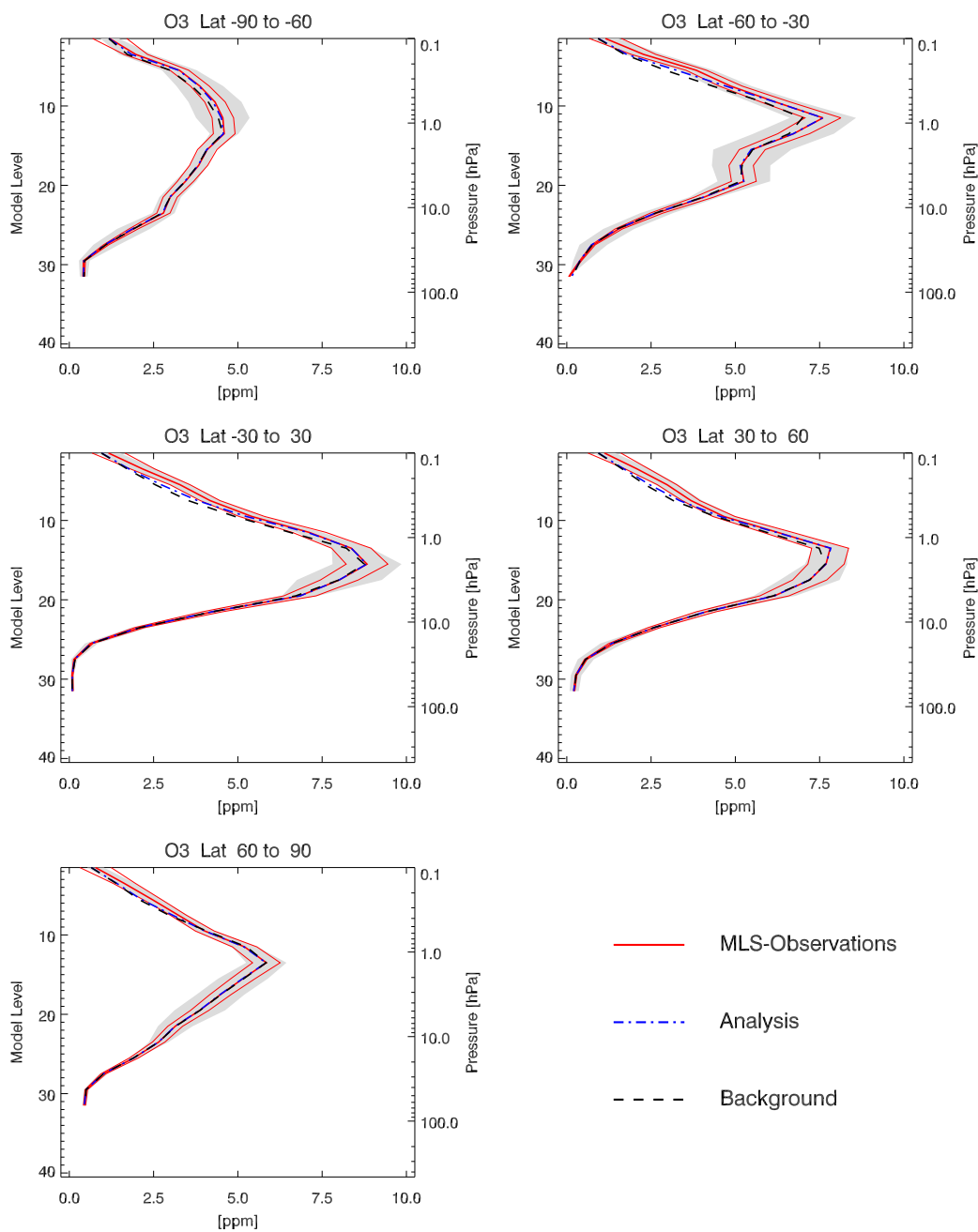


**Figure 6.23:**  $O_3$  mean profiles from 29.07.2006 for configuration **AMMA-SCOUT-3**. MLS retrieved profile values (assimilated) together with their error bars are given in red, the background values: black dashed line, the analysis values: dash-dotted blue line. The grey-shaded area indicates values within the standard deviation of observations.

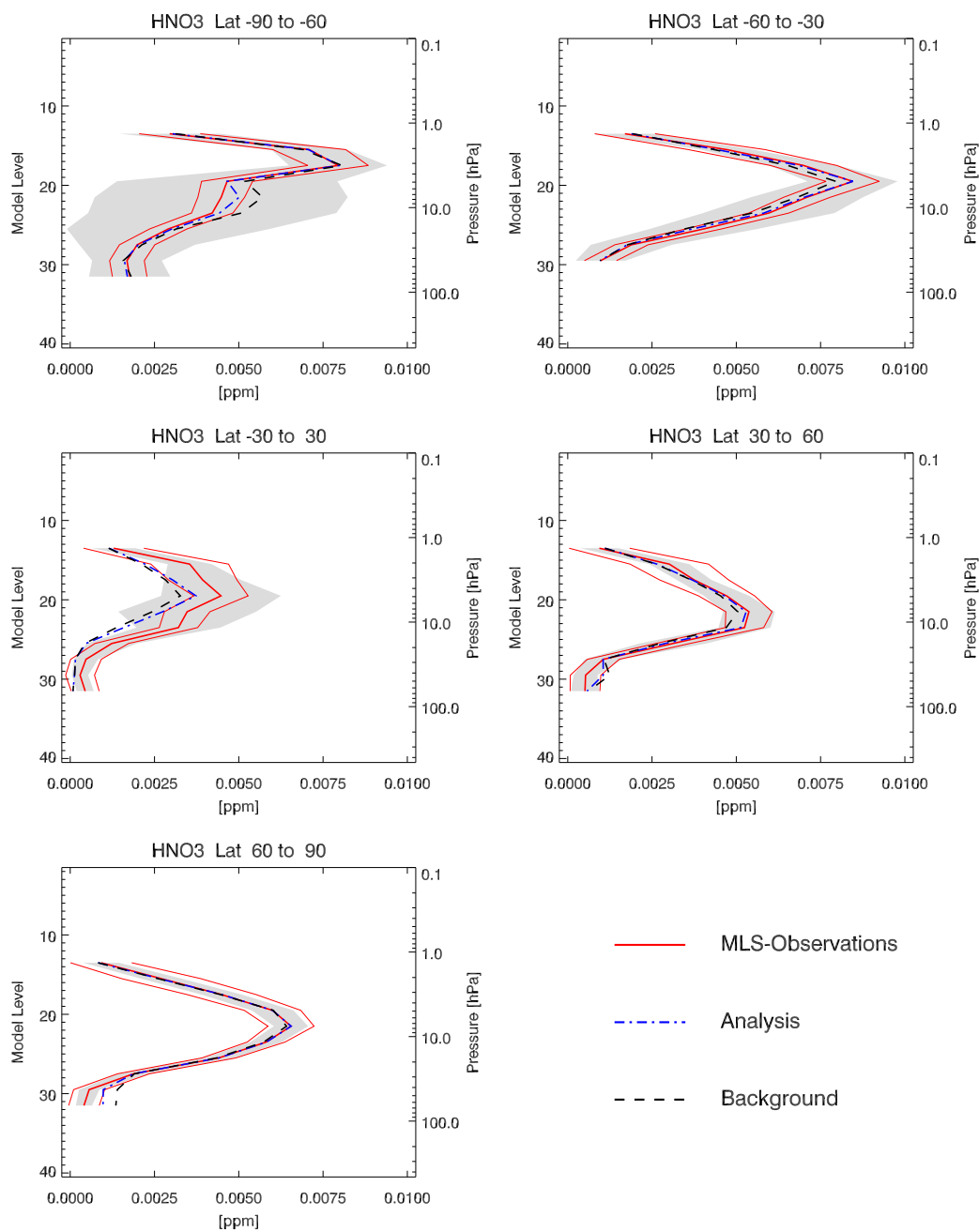


**Figure 6.24:**  $\text{HNO}_3$  mean profiles from 29.07.2006 for configuration AMMA-SCOUT-3. MLS retrieved profile values (assimilated) together with their error bars are given in red, the background values: black dashed line, the analysis values: dash-dotted blue line. The grey-shaded area indicates values within the standard deviation of observations.

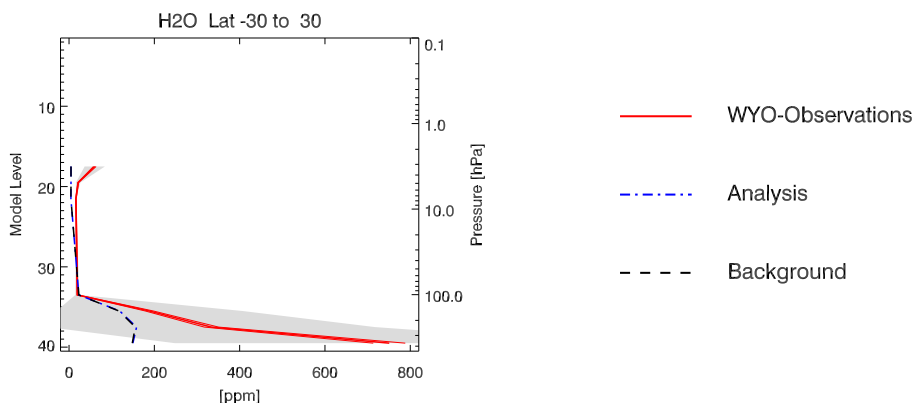


**Figure 6.25:**  $H_2O$  mean profile values from 1 August 2006 for configuration *AMMA-SCOUT-2*. Radiosonde profile values (not assimilated, Wyoming database) together with their error bars are given in red, the background values: black dashed line, the analysis values: dash-dotted blue line. The list of the Wyoming stations in Table 5.1

The mean  $H_2O$  analysis is in a good agreement with MLS observation above 180 hPa altitude (Fig. 6.22). The negative bias is seen towards high mixing ratios in low altitudes below 180 hPa, especially in tropics and mid-latitudes where the standard deviation of the observations are large. The mean  $O_3$  analysis (Fig. 6.23) show a very good compliance with both, MLS observations and the background field, which is actually the previous day analysis of the model. A minor negative bias is visible in the altitude range between 0.4hPa and 0.2 hPa in tropics and mid-latitudes. Also mean  $HNO_3$  analysis show a good agreement with MLS observations, except in the tropics (Fig. 6.24). Here, a small negative bias is seen between altitudes 20 hPa and 9 hPa, in all other heights analysis is in the range of the observation errors.

The analysis increment together with available observations on the model level 33, corresponding to 208 hPa is shown in Figures 6.27 and 6.28. The CRISTANF observations from 13th August 2006, local flight from Ouagadougou, are presented in Figure 6.27, bottom. The measurements are taken between 12:30 and 16:23 UTC. The analysis increment is at 24:00 UTC (Fig. 6.27, left). Thus, the difference between observation time and the analysis is about 8 hours. Note, that only for computational reasons the model states are saved at 12 and 24 UTC and each of the state is saved in file with size of about 220 MB. On the Fig. 6.27 is seen, that high concentrated  $H_2O$  observations over Ghana are transported to the west in this 8 hours, this is an effect of the Tropical Easterly Jet stream (TEJ), also seen on Figure 6.26. The west African jet streams are described in detail by *Okonkwo et al.* [2014].

The MLS measurements (right) and analysis increment (left) for 13 August

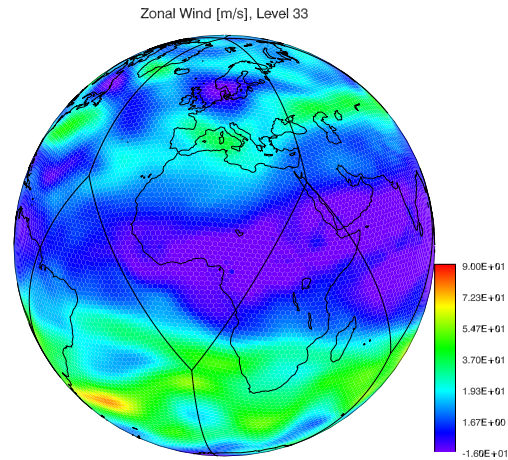


**Figure 6.26:** GME zonal wind for 13 August 2006 at model level 33, corresponding to 208 hPa (about 11.5 km altitude).

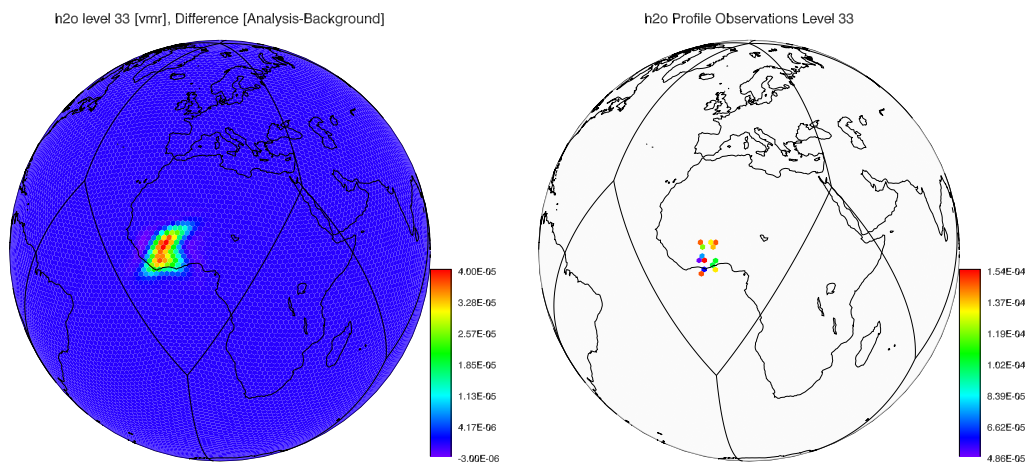


**Figure 6.27:** SCOUT-AMMA-2 water vapor analysis increment (analysis-background, left) and CRISTA-NF  $H_2O$  observations (right) for 13 August 2006 at model level 33, corresponding to 208 hPa (about 11.5 km altitude).

are shown in Figure 6.28. The MLS measurement available close to the west and east border of Ghana show a negative bias from the CRISTA-NF measurements in the same region (Fig. 6.27, bottom). The maximal discrepancy is about 40%. This can be also taken from Figure 6.29, where the analysis of the assimilated CRISTA-NF (left) and MLS (right) observations are compared. The radiosondes from Wyoming database (Figure 6.25) are measure even higher water concentrations in this region than the MLS and CRISTA-NF. On the Figure 6.29 it is seen that assimilation of CRISTA-NF observations 13 August 2006 improves the budget of the water vapor over Ghana compered

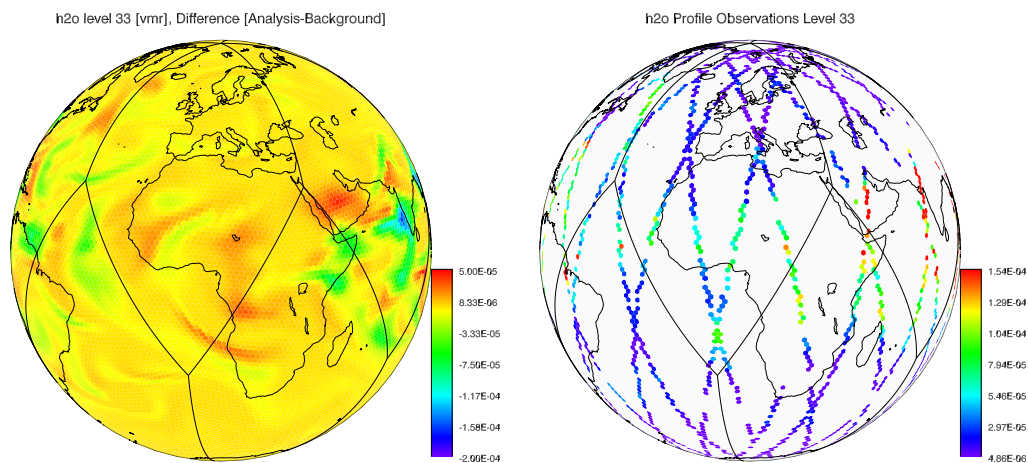


**Figure 6.28:** *SCOUT-AMMA-2* water vapor analysis increment (analysis-background, left) and *MLS*  $H_2O$  observations (right) for 13 August 2006 at model level 33, corresponding to 208 hPa (about 11.5 km altitude).

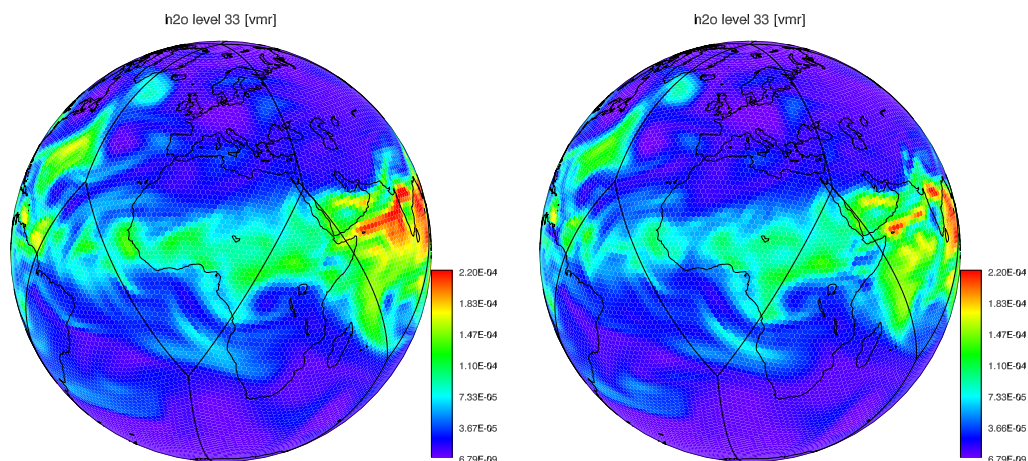


**Figure 6.29:** *SCOUT-AMMA-2*  $H_2O$  analysis of assimilated *CRISTA-NF* (left) and *MLS* (right) observations for 13 August 2006 at model level 33, corresponding to 208 hPa (about 11.5 km altitude).

to *MLS* analysis.

Some single *CRISTA-NF* profiles with its error bars (red), corresponding analysis (blue) and background (black) from 29 July 2006 and 1 August 2006 are shown in Figures 6.30 and 6.31, respectively. It is seen that the analysis is a good compliance with observations above 300 hPa. The negative bias in low altitudes is correlated with the large errors of *CRISTA-NF* water observations (up to 50%) in comparison with model background error (40%) and also with the errors of *MLS* water observations (up to 15%).

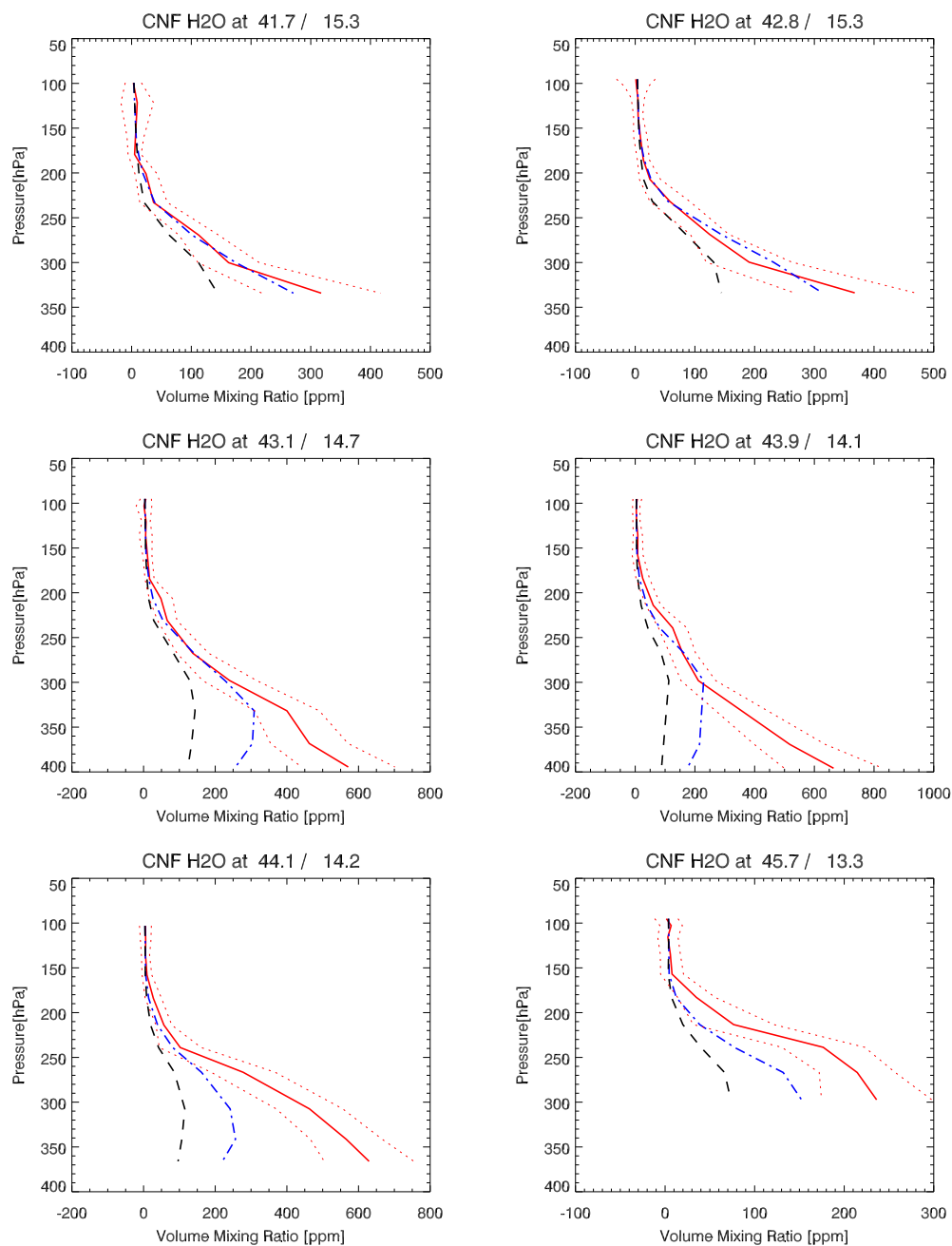


**Figure 6.30:** SCOUT-AMMA-2 H<sub>2</sub>O profile values from 29 July 2006. CRISTA-NF retrieved profile values (assimilated) together with its error bars are given in red, the background values: black dashed line, the analysis values: dash-dotted blue line. The geographical coordinates in Latitude/longitude format is seen above the profile plots.

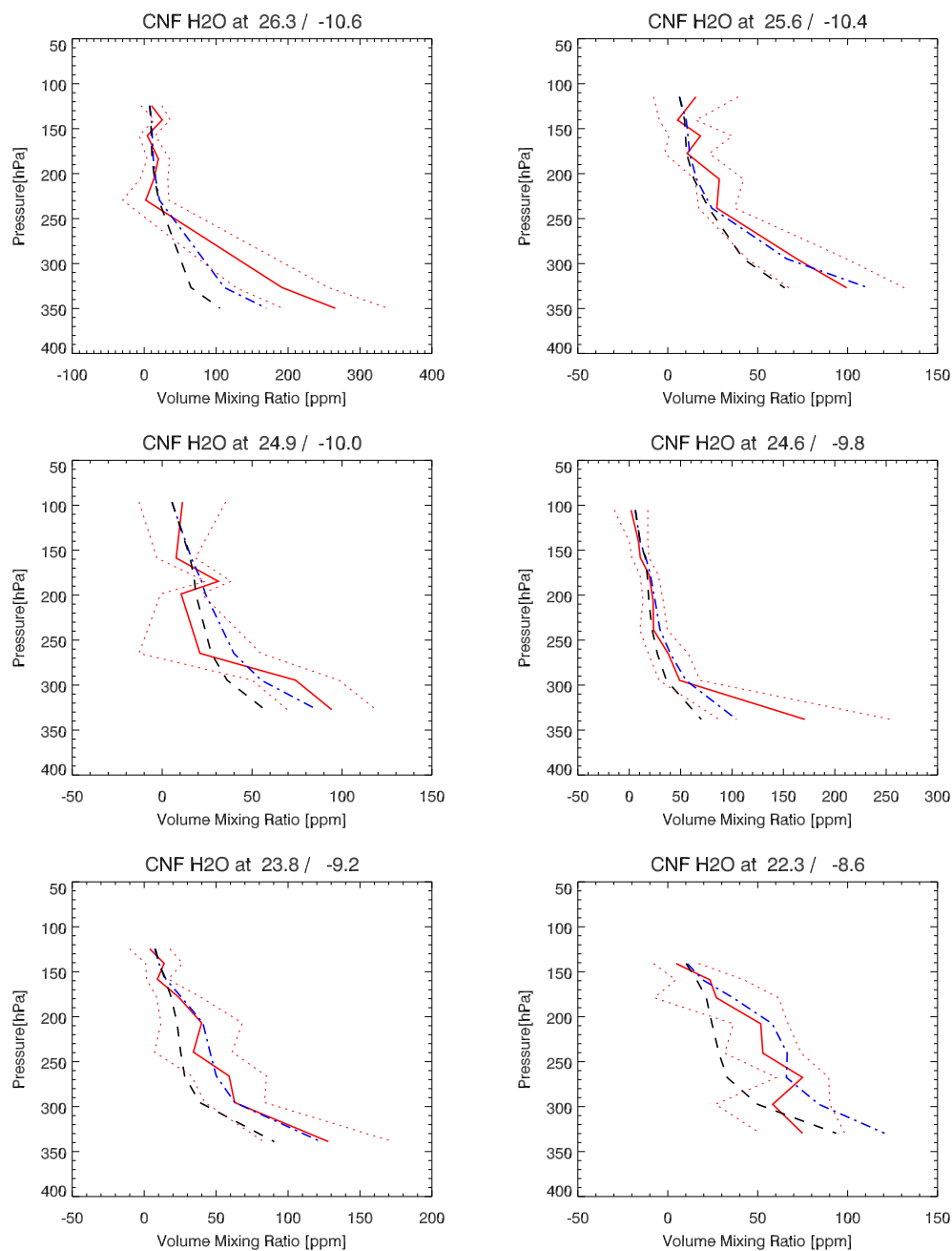


**Figure 6.31:** SCOUT-AMMA-2 H<sub>2</sub>O profile values from 1 August 2006. CRISTA-NF retrieved profile values (assimilated) together with its error bars are given in red, the background values: black dashed line, the analysis values: dash-dotted blue line. The geographical coordinates in Latitude/longitude format is seen above the profile plots.

## CHAPTER 7

---

### Summary and Conclusions

---

Aircraft measurements, highly resolving and well suited for UTLS filamental structures, are of most interest for local studies. Although, the satellite instruments are delivering an unprecedented wealth of observations of a number of stratospheric trace gases with global coverage, they are scattered and have a limited resolution in space or time. Combining these measurements and applying advanced data assimilation techniques to compare benefits from satellite and air borne data, and to analyse the chemical composition of the tropopause and lower stratosphere, was the issue of this work. Thus, improvement of the SACADA assimilation system for the assimilation of high resolution aircraft data was accomplished. For this purpose, a model grid refinement and full revision of the chemical mechanism were performed. The resolution of the horizontal grid points was increased from about 240 km to 150 km, resulting in 23 042 grid points per model levels. The vertical resolution was increased with twelve additional layers, especially in the UTLS region. Hence, the vertical separation between grid levels is now less than 1 km below 22 km altitude.

The chemistry module of SACADA was extended and revised to better represent chemical processes in the UTLS region: 15 photolysis, 24 gas phase and three heterogeneous reactions were added to the SACADA chemical mechanism. In total, a number of 197 chemical reaction of 51 stratospheric trace gases is considered by the chemistry module now. All reaction rates were updated according to the recommendations of the NASA's Jet Propulsion Laboratory. Heterogeneous reactions on PSC and aerosol surfaces are also included in

the reaction mechanism and its adjoint. The Tropospheric Ultraviolet-Visible Radiation Model, from National Center for Atmospheric Research, was adapted in order to build a look-up table of photo-dissociation frequencies for the photolysis reactions of new stratospheric chemistry mechanism on the high resolution grid. Thus, a novel global chemistry transport model with its adjoint version is the kernel of this system.

To evaluate and test improved SACADA assimilation system, two measurement campaigns, operating CRISTA-NF on board of M55 Geophysica, SCOUT-O3 and SCOUT-AMMA, over the periods November-December 2005 and July-August 2006 were studied. Retrievals of various stratospheric trace gases derived from EOS MLS spectra as well as retrievals of aircraft measurements from CRISTA-NF have been assimilated. The assimilation results have been validated with independent (not assimilated) data from HALOE and MIPAS-IMK satellite instruments, and radiosondes.

The performance of the newly extended system has been validated in various ways. Assessing the cost function evolution with  $\chi^2$ -tests show a good results of minimisation performance. It is shown that the water analysis improves, with progressing days assimilated, compared to the ECMWF operational analysis. A negative bias of assimilated water fields against retrieved profiles in the upper troposphere has been detected. The assimilation of water combined with other species led to a less improved  $H_2O$  analysis. This issue can most probably be attributed to relatively large errors of retrieved water concentrations compared to other assimilated species. This is a problem of preconditioning of species with anti-correlation in stratosphere and troposphere, with orders of magnitude of concentrations. It can be expected that a more sophisticated estimation of the BECM parameters used in the diffusion scheme will further improve the quality of analysed trace gas fields. A perfect analysis performance with respect to the assimilated ozone observations is shown. A cross validation of water and ozone profiles obtained from different measurement instruments has been performed. The results of ozone cross-validation show a very good agreement of HALOE and assimilated MLS profile values.

It can be concluded that the improved SACADA assimilation system is dealing well with high resolution aircraft measurements. To bring more clarity in the UTLS fine structures, additional and more accurate aircraft measurements is desirable.

For the future, both an further extended assimilation system and air borne measurement platforms can be combined. A great benefit for the SACADA assimilation system performance would be adapting ICON (ICOsahedral Non-hydrostatic model) grid (*Zängl* [2013]), with an option of using a high horizontal resolution and an advanced nesting technique, to the model. This is ap-

plicable, since SACADA is also based on an icosahedral-triangular Arakawa-C grid, as ICON. Further studies with SACADA, analysing the chemical composition of the tropopause and lower stratosphere with higher spatial resolution should consider two- and three-dimensional observations provided by the state of the art aircraft instrument GLORIA.



# APPENDIX A

---

## Tables

---

### A.1 Vertical grid parameters

**Table A.1:** Coefficients defining the vertical grid.  $k$  is the layer index,  $a_{f,k}$  and  $b_{f,k}$  are the coefficients defining the pressure at the centre of layer  $k$  according to (3.4.1). The coefficients  $a_k$ ,  $b_k$  define the pressure at the upper boundary and  $a_{k+1}$ ,  $b_{k+1}$  the pressure at the bottom of layer  $k$ . The last column gives the height of the centre of layer, computed from pressure according to the U.S. Standard Atmosphere from 1976.

$k$	$a_k$ [Pa]	$b_k$ [-]	$a_{f,k}$ [Pa]	$b_{f,k}$ [-]	Height [km]
1	0.000	0.0	0.1000	0.0	65.615920
2	0.200	0.0	0.2900	0.0	57.926560
3	0.380	0.0	0.4800	0.0	54.053570
4	0.580	0.0	0.6650	0.0	51.525340
5	0.750	0.0	0.8500	0.0	49.656140
6	0.950	0.0	1.0730	0.0	47.886280
7	1.196	0.0	1.3510	0.0	46.135640
8	1.506	0.0	1.7030	0.0	44.398880
9	1.900	0.0	2.1530	0.0	42.669600
10	2.406	0.0	2.7330	0.0	40.949940

$k$	$a_k$ [Pa]	$b_k$ [-]	$a_{f,k}$ [Pa]	$b_{f,k}$ [-]	Height [km]
11	3.060	0.0	3.4820	0.0	39.238820
12	3.904	0.0	4.4550	0.0	37.528760
13	5.006	0.0	5.7230	0.0	35.822980
14	6.440	0.0	7.3800	0.0	34.117200
15	8.320	0.0	9.5450	0.0	32.416760
16	10.770	0.0	12.3600	0.0	30.736620
17	13.950	0.0	16.0050	0.0	29.087450
18	18.060	0.0	20.7000	0.0	27.502370
19	23.340	0.0	26.6700	0.0	25.989910
20	30.000	0.0	33.7000	0.0	24.566120
21	37.400	0.0	40.8910	0.0	23.256610
22	44.382	0.0	48.0990	0.0	22.059250
23	51.816	0.0	56.1220	0.0	20.951610
24	60.428	0.0	65.4070	0.0	19.921950
25	70.386	0.0	76.1175	0.0	18.938220
26	81.849	0.0	88.4915	0.00000055	17.965160
27	95.134	0.00000110	102.8220	0.00000260	17.000660
28	110.510	0.00000410	117.8250	0.00146115	16.043620
29	125.140	0.00291820	132.4700	0.00542878	15.096210
30	139.800	0.00793936	144.8520	0.01375970	14.170150
31	149.903	0.01958000	153.3970	0.02852750	13.275070
32	156.892	0.03747500	159.7790	0.04848250	12.396010
33	162.666	0.05949000	163.6580	0.07369000	11.528700
34	164.650	0.08789000	163.8130	0.10494500	10.688100
35	162.976	0.12200000	160.4460	0.14172000	9.873123
36	157.916	0.16144000	153.8840	0.18357000	9.086990
37	149.853	0.20570000	144.5540	0.22994500	8.329697
38	139.255	0.25419000	132.9540	0.28021500	7.600174
39	126.653	0.30624000	119.6320	0.33369500	6.899490
40	112.612	0.36115000	105.1630	0.38967500	6.226578
41	97.714	0.41820000	90.1230	0.44744500	5.579300
42	82.532	0.47669000	75.0725	0.50629000	4.958725
43	67.613	0.53589000	60.5360	0.56548500	4.362717
44	53.459	0.59508000	46.9830	0.62432000	3.791275
45	40.507	0.65356000	34.8115	0.68207500	3.245468
46	29.116	0.71059000	24.3320	0.73800000	2.726364
47	19.548	0.76541000	15.7535	0.79129000	2.235031

---

$k$	$a_k$ [Pa]	$b_k$ [-]	$a_{f,k}$ [Pa]	$b_{f,k}$ [-]	Height [km]
48	11.959	0.81717000	9.1700	0.84106500	1.774673
49	6.381	0.86496000	4.5485	0.88634000	1.348495
50	2.716	0.90772000	1.7185	0.92596500	0.965042
51	0.721	0.94421000	0.3605	0.95860000	0.628585
52	0.000	0.97299000	0.0	0.98263500	0.351944
53	0.000	0.99228000	0.0	0.99614000	0.147934
54	0.000	1.0	-	-	-

## A.2 Reaction equations

*Table A.2: Photolysis reactions included in the model CHEM51.*

Reaction	
(R1)	$O_2+h\nu\rightarrow O(^3P)+O(^1D)$
(R2)	$O_2+h\nu\rightarrow O(^3P)+O(^3P)$
(R3)	$O_3+h\nu\rightarrow O(^1D)+O_2$
(R4)	$O_3+h\nu\rightarrow O(^3P)+O_2$
(R5)	$N_2O+h\nu\rightarrow N_2+O(^1D)$
(R6)	$NO+h\nu\rightarrow O(^3P)$
(R7)	$NO_2+h\nu\rightarrow O(^3P)+NO$
(R8)	$N_2O_5+h\nu\rightarrow NO_3+NO+O(^3P)$
(R9)	$N_2O_5+h\nu\rightarrow NO_2+NO_3$
(R10)	$HNO_3+h\nu\rightarrow OH+NO_2$
(R11)	$NO_3+h\nu\rightarrow NO_2+O(^3P)$
(R12)	$NO_3+h\nu\rightarrow NO+O_2$
(R13)	$HNO_4+h\nu\rightarrow OH+NO_3$
(R14)	$HNO_4+h\nu\rightarrow HO_2+NO_2$
(R15)	$CH_3OOH+h\nu\rightarrow CH_3O+OH$
(R16)	$CH_2O+h\nu\rightarrow H+HCO$
(R17)	$CH_2O+h\nu\rightarrow H_2+CO$
(R18)	$H_2O+h\nu\rightarrow H+OH$
(R19)	$H_2O+h\nu\rightarrow H_2+O(^1D)$
(R20)	$H_2O+h\nu\rightarrow 2H+O(^3P)$
(R21)	$H_2O_2+h\nu\rightarrow OH+OH$
(R22)	$Cl_2+h\nu\rightarrow Cl+Cl$
(R23)	$ClO+h\nu\rightarrow Cl+O(^3P)$
(R24)	$OCIO+h\nu\rightarrow O(^3P)+ClO$
(R25)	$ClOO+h\nu\rightarrow O(^3P)+ClO$
(R26)	$Cl_2O_2+h\nu\rightarrow Cl+Cl+O_2$
(R27)	$HOCl+h\nu\rightarrow Cl+OH$
(R28)	$HCl+h\nu\rightarrow Cl+H$
(R29)	$ClONO_2+h\nu\rightarrow Cl+NO_3$
(R30)	$ClONO_2+h\nu\rightarrow ClO+NO_2$
(R31)	$ClNO_2+h\nu\rightarrow Cl+NO_2$
(R32)	$BrCl+h\nu\rightarrow Br+Cl$
(R33)	$Br_2+h\nu\rightarrow Br+Br$
(R34)	$BrO+h\nu\rightarrow Br+O(^3P)$
(R35)	$HOBr+h\nu\rightarrow Br+OH$
(R36)	$BrONO_2+h\nu\rightarrow Br+NO_3$
(R37)	$BrONO_2+h\nu\rightarrow BrO+NO_2$
(R38)	$CH_3Cl+h\nu\rightarrow Cl$
(R39)	$CCl_4+h\nu\rightarrow Cl+Cl+Cl+Cl$
(R40)	$CH_3CCl_3+h\nu\rightarrow Cl+Cl+Cl$
(R41)	$CFCl_3+h\nu\rightarrow Cl+Cl+Cl$
(R42)	$CF_2Cl_2+h\nu\rightarrow Cl+Cl$

**Table A.2:** Photolysis reactions included in the model CHEM51 (continued)

Reaction	
(R43)	$\text{CF}_2\text{ClCFCl}_2 + h\nu \rightarrow \text{Cl} + \text{Cl} + \text{Cl}$
(R44)	$\text{CHF}_2\text{Cl} + h\nu \rightarrow \text{Cl}$
(R45)	$\text{CH}_3\text{Br} + h\nu \rightarrow \text{Br}$
(R46)	$\text{CF}_3\text{Br} + h\nu \rightarrow \text{Br}$
(R47)	$\text{CF}_2\text{ClBr} + h\nu \rightarrow \text{Cl} + \text{Br}$
(R48)	$\text{CH}_4 + h\nu \rightarrow \text{CH}_3 + \text{H}$
(R49)	$\text{CH}_4 + h\nu \rightarrow \text{H}_2$

**Table A.3:** Gas phase reactions that are included in the model CHEM51. Rate constants for first- and second-order reactions are given in units of  $\text{s}^{-1}$  and  $\text{molecules}^{-1}\text{cm}^3\text{s}^{-1}$ , respectively. Rate constants for third-order reactions are given as effective second-order rate constants in units of  $\text{molecules}^{-1}\text{cm}^3\text{s}^{-1}$ .  $M \in \{\text{N}_2, \text{O}_2\}$ . For third-order reactions,  $f_{\text{3rd}} = f(k_0, k_\infty)$  has to be evaluated according to Sander et al. [2011]:

$$f(k_0, k_\infty) = (k_0[M]/(1 + k_0[M]/k_\infty)) \times 0.6^{(1+(\log_{10}(k_0[M]/k_\infty))^2)^{-1}}.$$

The term products represents constituents which are not considered in the reaction scheme.

Reaction	
Bimolekular Reaktionen:	
(R1)	A1 $\text{O}(^3\text{P}) + \text{O}_3 \rightarrow \text{O}_2 + \text{O}_2$ 8.0E-12*exp(-2060.0/T)
(R2)	A2,A3 $\text{O}(^1\text{D}) + \text{O}_2 \rightarrow \text{O}(^3\text{P}) + \text{O}_2$ 3.3E-11*exp(55.0/T)
(R3)	A2,A4 $\text{O}(^1\text{D}) + \text{O}_3 \rightarrow \text{O}_2 + \text{O}_2$ 1.2E-10
(R4)	A2,A4 $\text{O}(^1\text{D}) + \text{O}_3 \rightarrow \text{O}(^3\text{P}) + \text{O}(^3\text{P}) + \text{O}_2$ 1.2E-10
(R5)	A2,A5 $\text{O}(^1\text{D}) + \text{H}_2 \rightarrow \text{OH} + \text{H}$ 1.1E-10
(R6)	A2,A6 $\text{O}(^1\text{D}) + \text{H}_2\text{O} \rightarrow \text{OH} + \text{OH}$ 1.63E-10*exp(60.0/T)
(R7)	A2,A7 $\text{O}(^1\text{D}) + \text{N}_2 \rightarrow \text{O}(^3\text{P}) + \text{N}_2$ 2.15E-11*exp(110.0/T)
(R8)	A2,A8 $\text{N}_2\text{O} + \text{O}(^1\text{D}) \rightarrow \text{N}_2 + \text{O}_2$ 4.7E-11*exp(20.0/T)
(R9)	A2,A8 $\text{N}_2\text{O} + \text{O}(^1\text{D}) \rightarrow \text{NO} + \text{NO}$ 6.7E-11*exp(20.0/T)
(R10)	A2,A11 $\text{CH}_4 + \text{O}(^1\text{D}) \rightarrow \text{OH} + \text{CH}_3$ 1.125E-10
(R11)	A2,A11 $\text{O}(^1\text{D}) + \text{CH}_4 \rightarrow \text{CH}_2\text{O} + \text{H}_2$ 1.5E-10*0.05
(R12)	A2,A12 $\text{HCl} + \text{O}(^1\text{D}) \rightarrow \text{OH} + \text{Cl}$ 1.0E-10
(R13)	A2,A12 $\text{HCl} + \text{O}(^1\text{D}) \rightarrow \text{H} + \text{ClO}$ 3.6E-11
(R14)	A2,A15 $\text{HBr} + \text{O}(^1\text{D}) \rightarrow \text{OH} + \text{Br}$ 1.5E-10*0.8
(R15)	A2,A16 $\text{Cl}_2 + \text{O}(^1\text{D}) \rightarrow \text{ClO} + \text{Cl}$ 2.7E-10
(R16)	A19 $\text{CCl}_4 + \text{O}(^1\text{D}) \rightarrow \text{ClO}$ 3.3E-10*0.86
(R17)	A19 $\text{CFCl}_3 + \text{O}(^1\text{D}) \rightarrow \text{ClO}$ 2.3E-10*0.75
(R18)	A19 $\text{CF}_2\text{Cl}_2 + \text{O}(^1\text{D}) \rightarrow \text{ClO}$ 1.4E-10*0.82
(R19)	A19,A20 $\text{CH}_3\text{Br} + \text{O}(^1\text{D}) \rightarrow \text{BrO} + \text{CH}_3$ 1.8E-10
(R20)	A19,A27 $\text{CHF}_2\text{Cl} + \text{O}(^1\text{D}) \rightarrow \text{ClO}$ 1.0E-10
(R21)	A19,A46 $\text{CF}_2\text{ClCFCl}_2 + \text{O}(^1\text{D}) \rightarrow \text{ClO}$ 2.0E-10
(R22)	A19,A30 $\text{CF}_2\text{ClBr} + \text{O}(^1\text{D}) \rightarrow \text{BrO}$ 1.5E-10

**Table A.3:** Gas phase reaction equations included in the model CHEM51 (continued)

Reaction			
(R23)	A19,A32	$\text{CF}_3\text{Br} + \text{O}(^1\text{D}) \rightarrow \text{BrO}$	1.0E-10
(R24)	B1	$\text{OH} + \text{O}(^3\text{P}) \rightarrow \text{H} + \text{O}_2$	$2.2\text{E-}11 * \exp(120.0/\text{T})$
(R25)	B2	$\text{HO}_2 + \text{O}(^3\text{P}) \rightarrow \text{OH} + \text{O}_2$	$3.0\text{E-}11 * \exp(200.0/\text{T})$
(R26)	B3	$\text{H}_2\text{O}_2 + \text{O}(^3\text{P}) \rightarrow \text{HO}_2 + \text{OH}$	$1.4\text{E-}12 * \exp(-2000.0/\text{T})$
(R27)	B4	$\text{H} + \text{O}_3 \rightarrow \text{OH} + \text{O}_2$	$1.4\text{E-}10 * \exp(-470.0/\text{T})$
(R28)	B5	$\text{H} + \text{HO}_2 \rightarrow \text{OH} + \text{OH}$	7.2E-11
(R29)	B5	$\text{H} + \text{HO}_2 \rightarrow \text{H}_2 + \text{O}_2$	6.9E-12
(R30)	B5	$\text{H} + \text{HO}_2 \rightarrow \text{H}_2\text{O} + \text{O}(^3\text{P})$	1.6E-12
(R31)	B6	$\text{OH} + \text{O}_3 \rightarrow \text{HO}_2 + \text{O}_2$	$1.7\text{E-}12 * \exp(-940.0/\text{T})$
(R32)	B7	$\text{OH} + \text{H}_2 \rightarrow \text{H}_2\text{O} + \text{H}$	$2.8\text{E-}12 * \exp(-1800.0/\text{T})$
(R33)	B9	$\text{OH} + \text{OH} \rightarrow \text{H}_2\text{O} + \text{O}(^3\text{P})$	1.8E-12
(R34)	B10	$\text{OH} + \text{HO}_2 \rightarrow \text{H}_2\text{O} + \text{O}_2$	$4.8\text{E-}11 * \exp(250.0/\text{T})$
(R35)	B11	$\text{OH} + \text{H}_2\text{O}_2 \rightarrow \text{H}_2\text{O} + \text{HO}_2$	1.8E-12
(R36)	B12	$\text{HO}_2 + \text{O}_3 \rightarrow \text{OH} + \text{O}_2 + \text{O}_2$	$1.0\text{E-}14 * \exp(-490.0/\text{T})$
(R37)	B13	$\text{HO}_2 + \text{HO}_2 \rightarrow \text{H}_2\text{O}_2 + \text{O}_2$	$3.5\text{E-}13 * \exp(430.0/\text{TEMP}) +$ $1.7\text{E-}33 * \exp(1000.0/\text{TEMP}) * \text{cair}$
(R38)	C1	$\text{NO}_2 + \text{O}(^3\text{P}) \rightarrow \text{NO} + \text{O}_2$	$5.1\text{E-}12 * \exp(210.0/\text{T})$
(R39)	C2	$\text{NO}_3 + \text{O}(^3\text{P}) \rightarrow \text{NO}_2 + \text{O}_2$	1.0E-11
(R40)	C6	$\text{NO}_2 + \text{H} \rightarrow \text{OH} + \text{NO}$	$4.0\text{E-}10 * \exp(-340.0/\text{T})$
(R41)	C7	$\text{NO}_3 + \text{OH} \rightarrow \text{NO}_2 + \text{HO}_2$	2.2E-11
(R42)	C9	$\text{HNO}_3 + \text{OH} \rightarrow \text{NO}_3 + \text{H}_2\text{O}$	$f_{\text{HNO3}}(2.4\text{E-}14, 460.0, 2.7\text{E-}17,$ $2199.0, 6.5\text{E-}34, 1335.0)$
(R43)	C10	$\text{HNO}_4 + \text{OH} \rightarrow \text{NO}_2 + \text{H}_2\text{O} + \text{O}_2$	$1.3\text{E-}12 * \exp(380.0/\text{T})$
(R44)	C12	$\text{NO} + \text{HO}_2 \rightarrow \text{OH} + \text{NO}_2$	$3.5\text{E-}12 * \exp(250.0/\text{T})$
(R45)	C14	$\text{NO}_3 + \text{HO}_2 \rightarrow \text{HNO}_3 + \text{O}_2$	$3.5\text{E-}12 * 0.2$
(R46)	C14	$\text{HO}_2 + \text{NO}_3 \rightarrow \text{OH} + \text{NO}_2 + \text{O}_2$	$3.5\text{E-}12 * 0.8$
(R47)	C20	$\text{NO} + \text{O}_3 \rightarrow \text{NO}_2 + \text{O}_2$	$3.0\text{E-}12 * \exp(-1500.0/\text{T})$
(R48)	C21	$\text{NO} + \text{NO}_3 \rightarrow \text{NO}_2 + \text{NO}_2$	$1.5\text{E-}11 * \exp(170.0/\text{T})$
(R49)	C22	$\text{NO}_2 + \text{O}_3 \rightarrow \text{NO}_3 + \text{O}_2$	$1.2\text{E-}13 * \exp(-2450.0/\text{T})$
(R50)	C23	$\text{NO}_2 + \text{NO}_3 \rightarrow \text{NO} + \text{NO}_2 + \text{O}_2$	$4.5\text{E-}14 * \exp(-1260.0/\text{T})$
(R51)	C24	$\text{NO}_3 + \text{NO}_3 \rightarrow \text{NO}_2 + \text{NO}_2 + \text{O}_2$	$8.5\text{E-}13 * \exp(-2450.0/\text{T})$
(R52)	D4	$\text{CH}_2\text{O} + \text{O}(^3\text{P}) \rightarrow \text{OH} + \text{HCO}$	$3.4\text{E-}11 * \exp(-1600.0/\text{T})$
(R53)	D11	$\text{CH}_4 + \text{OH} \rightarrow \text{H}_2\text{O} + \text{CH}_3$	$2.45\text{E-}12 * \exp(-1775.0/\text{T})$
(R54)	D14	$\text{CH}_2\text{O} + \text{OH} \rightarrow \text{H}_2\text{O} + \text{HCO}$	$5.5\text{E-}12 * \exp(125.0/\text{T})$
(R55)	D16	$\text{CH}_3\text{OOH} + \text{OH} \rightarrow \text{CH}_3\text{O}_2 + \text{H}_2\text{O}$	$3.8\text{E-}12 * \exp(200/\text{T}) * 0.7$
(R56)	D16	$\text{CH}_3\text{OOH} + \text{OH} \rightarrow \text{CH}_2\text{O} + \text{OH} + \text{H}_2\text{O}$	$3.8\text{E-}12 * \exp(200/\text{T}) * 0.3$
(R57)	D35	$\text{CH}_3\text{O}_2 + \text{HO}_2 \rightarrow \text{CH}_3\text{OOH} + \text{O}_2$	$4.1\text{E-}13 * \exp(750.0/\text{T})$
(R58)	D44	$\text{HCO} + \text{O}_2 \rightarrow \text{CO} + \text{HO}_2$	5.2E-12
(R59)	D46	$\text{CH}_3\text{O} + \text{O}_2 \rightarrow \text{CH}_2\text{O} + \text{HO}_2$	$3.9\text{E-}14 * \exp(-900.0/\text{T})$
(R60)	D51	$\text{CH}_3\text{O}_2 + \text{NO} \rightarrow \text{CH}_3\text{O} + \text{NO}_2$	$2.8\text{E-}12 * \exp(300.0/\text{T})$
(R61)	F1	$\text{ClO} + \text{O}(^3\text{P}) \rightarrow \text{Cl} + \text{O}_2$	$2.8\text{E-}11 * \exp(85.0/\text{T})$
(R62)	F2	$\text{OClO} + \text{O}(^3\text{P}) \rightarrow \text{ClO} + \text{O}_2$	$2.4\text{E-}12 * \exp(-960.0/\text{T})$
(R63)	F4	$\text{HCl} + \text{O}(^3\text{P}) \rightarrow \text{OH} + \text{Cl}$	$1.0\text{E-}11 * \exp(-3300.0/\text{T})$
(R64)	F5	$\text{HOCl} + \text{O}(^3\text{P}) \rightarrow \text{ClO} + \text{OH}$	1.7E-13
(R65)	F6	$\text{ClONO}_2 + \text{O}(^3\text{P}) \rightarrow \text{ClO} + \text{NO}_3$	$2.9\text{E-}12 * \exp(-800.0/\text{T})$

**Table A.3:** Gas phase reaction equations included in the model CHEM51 (continued)

Reaction			
(R66)	F7	$\text{OCIO} + \text{O}_3 \rightarrow \text{O}_2 + \text{O}_2 + \text{ClO}$	$2.1\text{E-}12^* \exp(-4700.0/\text{T})$
(R67)	F9	$\text{Cl}_2 + \text{OH} \rightarrow \text{HOCl} + \text{Cl}$	$1.4\text{E-}12^* \exp(-900.0/\text{T})$
(R68)	F10	$\text{ClO} + \text{OH} \rightarrow \text{Cl} + \text{HO}_2$	$7.4\text{E-}12^* \exp(270.0/\text{T})$
(R69)	F10	$\text{ClO} + \text{OH} \rightarrow \text{HCl} + \text{O}_2$	$6.0\text{E-}13^* \exp(230.0/\text{T})$
(R70)	F11	$\text{OCIO} + \text{OH} \rightarrow \text{HOCl} + \text{O}_2$	$4.5\text{E-}13^* \exp(800.0/\text{T})$
(R71)	F12	$\text{HCl} + \text{OH} \rightarrow \text{Cl} + \text{H}_2\text{O}$	$2.6\text{E-}12^* \exp(-350.0/\text{T})$
(R72)	F13	$\text{HOCl} + \text{OH} \rightarrow \text{ClO} + \text{H}_2\text{O}$	$3.0\text{E-}12^* \exp(-500.0/\text{T})$
(R73)	F14	$\text{ClNO}_2 + \text{OH} \rightarrow \text{HOCl} + \text{NO}_2$	$2.4\text{E-}12^* \exp(-1250.0/\text{T})$
(R74)	F15	$\text{ClONO}_2 + \text{OH} \rightarrow \text{HOCl} + \text{NO}_3$	$1.2\text{E-}12^* \exp(-330.0/\text{T})$
(R75)	F16	$\text{CH}_3\text{Cl} + \text{OH} \rightarrow \text{H}_2\text{O}$	$2.4\text{E-}12^* \exp(-1250.0/\text{T})$
(R76)	F22	$\text{CHF}_2\text{Cl} + \text{OH} \rightarrow \text{H}_2\text{O}$	$1.05\text{E-}12^* \exp(-1600.0/\text{T})$
(R77)	F26	$\text{CH}_3\text{CCl}_3 + \text{OH} \rightarrow \text{H}_2\text{O}$	$1.64\text{E-}12^* \exp(-1520.0/\text{T})$
(R78)	F45	$\text{Cl} + \text{HO}_2 \rightarrow \text{HCl} + \text{O}_2$	$1.8\text{E-}11^* \exp(170.0/\text{T})$
(R79)	F45	$\text{Cl} + \text{HO}_2 \rightarrow \text{OH} + \text{ClO}$	$4.1\text{E-}11^* \exp(-450.0/\text{T})$
(R80)	F46	$\text{ClO} + \text{HO}_2 \rightarrow \text{HOCl} + \text{O}_2$	$2.7\text{E-}12^* \exp(220.0/\text{T})$
(R81)	F48	$\text{OCIO} + \text{NO} \rightarrow \text{ClO} + \text{NO}_2$	$2.5\text{E-}12^* \exp(-600.0/\text{T})$
(R82)	F52	$\text{Cl} + \text{O}_3 \rightarrow \text{ClO} + \text{O}_2$	$2.3\text{E-}11^* \exp(-200.0/\text{T})$
(R83)	F53	$\text{Cl} + \text{H}_2 \rightarrow \text{HCl} + \text{H}$	$3.05\text{E-}11^* \exp(-2270.0/\text{T})$
(R84)	F54	$\text{Cl} + \text{H}_2\text{O}_2 \rightarrow \text{HCl} + \text{HO}_2$	$1.1\text{E-}11^* \exp(-980.0/\text{T})$
(R85)	F55	$\text{Cl} + \text{NO}_3 \rightarrow \text{ClO} + \text{NO}_2$	$2.4\text{E-}11$
(R86)	F59	$\text{Cl} + \text{CH}_4 \rightarrow \text{HCl} + \text{CH}_3$	$7.3\text{E-}12^* \exp(-1280.0/\text{T})$
(R87)	F61	$\text{CH}_2\text{O} + \text{Cl} \rightarrow \text{HCl} + \text{HCO}$	$8.1\text{E-}11^* \exp(-30.0/\text{T})$
(R88)	F79	$\text{Cl} + \text{OCIO} \rightarrow \text{ClO} + \text{ClO}$	$3.4\text{E-}11^* \exp(160.0/\text{T})$
(R89)	F80	$\text{Cl} + \text{ClOO} \rightarrow \text{Cl}_2 + \text{O}_2$	$2.3\text{E-}10$
(R90)	F80	$\text{Cl} + \text{ClOO} \rightarrow \text{ClO} + \text{ClO}$	$1.2\text{E-}11$
(R91)	F82	$\text{Cl} + \text{Cl}_2\text{O}_2 \rightarrow \text{Cl}_2 + \text{ClOO}$	$1.0\text{E-}10$
(R92)	F83	$\text{Cl} + \text{HOCl} \rightarrow \text{Cl}_2 + \text{OH}$	$2.5\text{E-}12^* \exp(-130/\text{T}) * 0.58$
(R93)	F83	$\text{Cl} + \text{HOCl} \rightarrow \text{HCl} + \text{ClO}$	$2.5\text{E-}12^* \exp(-130/\text{T}) * 0.15$
(R94)	F85	$\text{Cl} + \text{ClONO}_2 \rightarrow \text{Cl}_2 + \text{NO}_3$	$6.5\text{E-}12^* \exp(135.0/\text{T})$
(R95)	F111	$\text{ClO} + \text{NO} \rightarrow \text{Cl} + \text{NO}_2$	$6.4\text{E-}12^* \exp(290.0/\text{T})$
(R96)	F112	$\text{ClO} + \text{NO}_3 \rightarrow \text{ClOO} + \text{NO}_2$	$4.7\text{E-}13$
(R97)	F117	$\text{CH}_3\text{O}_2 + \text{ClO} \rightarrow \text{CH}_3\text{O} + \text{Cl} + \text{O}_2$	$3.3\text{E-}12^* \exp(-115.0/\text{T})$
(R98)	F118	$\text{ClO} + \text{ClO} \rightarrow \text{Cl} + \text{OCIO}$	$3.5\text{E-}13^* \exp(-1370.0/\text{T})$
(R99)	F118	$\text{ClO} + \text{ClO} \rightarrow \text{Cl}_2 + \text{O}_2$	$1.0\text{E-}12^* \exp(-1590.0/\text{T})$
(R100)	F118	$\text{ClO} + \text{ClO} \rightarrow \text{Cl} + \text{ClOO}$	$3.0\text{E-}11^* \exp(-2450.0/\text{T})$
(R101)	G1	$\text{BrO} + \text{O}(^3\text{P}) \rightarrow \text{Br} + \text{O}_2$	$1.9\text{E-}11^* \exp(230.0/\text{T})$
(R102)	G2	$\text{HBr} + \text{O}(^3\text{P}) \rightarrow \text{Br} + \text{OH}$	$5.8\text{E-}12^* \exp(-1500.0/\text{T})$
(R103)	G3	$\text{HOBr} + \text{O}(^3\text{P}) \rightarrow \text{OH} + \text{BrO}$	$1.2\text{E-}10^* \exp(-430.0/\text{T})$
(R104)	G3	$\text{CH}_3\text{Br} + \text{OH} \rightarrow \text{H}_2\text{O}$	$2.35\text{E-}12^* \exp(-1300.0/\text{T})$
(R105)	G5	$\text{Br}_2 + \text{OH} \rightarrow \text{HOBr} + \text{Br}$	$2.1\text{E-}11^* \exp(240.0/\text{T})$
(R106)	G6	$\text{BrO} + \text{OH} \rightarrow \text{Br} + \text{HO}_2$	$1.7\text{E-}11^* \exp(250.0/\text{T})$
(R107)	G7	$\text{HBr} + \text{OH} \rightarrow \text{Br} + \text{H}_2\text{O}$	$5.5\text{E-}12^* \exp(200.0/\text{T})$
(R108)	G24	$\text{Br} + \text{HO}_2 \rightarrow \text{HBr} + \text{O}_2$	$4.8\text{E-}12^* \exp(-310.0/\text{T})$
(R109)	G25	$\text{BrO} + \text{HO}_2 \rightarrow \text{HOBr} + \text{O}_2$	$4.5\text{E-}12^* \exp(460.0/\text{T})$
(R110)	G31	$\text{Br} + \text{O}_3 \rightarrow \text{BrO} + \text{O}_2$	$1.7\text{E-}11^* \exp(-800.0/\text{T})$

**Table A.3:** Gas phase reaction equations included in the model CHEM51 (continued)

Reaction			
(R111)	G34	$\text{CH}_2\text{O} + \text{Br} \rightarrow \text{HBr} + \text{HCO}$	$1.7\text{E-}11 * \exp(-800.0/\text{T})$
(R112)	G35	$\text{Br} + \text{OCIO} \rightarrow \text{BrO} + \text{ClO}$	$2.6\text{E-}11 * \exp(-1300.0/\text{T})$
(R113)	G39	$\text{BrO} + \text{NO} \rightarrow \text{Br} + \text{NO}_2$	$8.8\text{E-}12 * \exp(260.0/\text{T})$
(R114)	G41	$\text{BrO} + \text{ClO} \rightarrow \text{Br} + \text{OCIO}$	$9.5\text{E-}13 * \exp(550.0/\text{T})$
(R115)	G41	$\text{BrO} + \text{ClO} \rightarrow \text{Br} + \text{ClOO}$	$2.3\text{E-}12 * \exp(260.0/\text{T})$
(R116)	G41	$\text{BrO} + \text{ClO} \rightarrow \text{BrCl} + \text{O}_2$	$4.1\text{E-}13 * \exp(290.0/\text{T})$
(R117)	G42	$\text{BrO} + \text{BrO} \rightarrow \text{Br} + \text{Br} + \text{O}_2$	$2.4\text{E-}12 * \exp(40.0/\text{T})$
(R118)	G42	$\text{BrO} + \text{BrO} \rightarrow \text{Br}_2 + \text{O}_2$	$2.8\text{E-}14 * \exp(860.0/\text{T})$
Termolekular Reaktionen:			
(R1)	A1	$\text{O}(^3\text{P}) + \text{O}_2 \rightarrow \text{O}_3$	$6.0\text{E-}34 * (\text{T}/300)^{-2.4} * \text{cair}$
(R2)	A2	$\text{N}_2 + \text{O}(^1\text{D}) \rightarrow \text{N}_2\text{O}$	$2.8\text{E-}36 * (\text{T}/300)^{-0.9} * \text{cair}$
(R3)	B1	$\text{H} + \text{O}_2 \rightarrow \text{HO}_2$	f_3rd(4.4E-32,-1.3,4.7E-11,-0.2)
(R4)	B2	$\text{OH} + \text{OH} \rightarrow \text{H}_2\text{O}_2$	f_3rd(6.9E-31,-1.0,2.6E-11,0.0)
(R5)	C1	$\text{NO} + \text{O}(^3\text{P}) \rightarrow \text{NO}_2$	f_3rd(9.0E-32,-1.5,3.0E-11,0.0)
(R6)	C2	$\text{NO}_2 + \text{O}(^3\text{P}) \rightarrow \text{NO}_3$	f_3rd(2.5E-31,-1.8,2.2E-11,-0.7)
(R7)	C4	$\text{NO}_2 + \text{OH} \rightarrow \text{HNO}_3$	f_3rd(1.8E-30,-3.0,2.8E-11,0.0)
(R8)	C5	$\text{NO}_2 + \text{HO}_2 \rightarrow \text{HNO}_4$	f_3rd(2.0E-31,-3.4,2.9E-12,-1.1)
(R9)	C6	$\text{NO}_2 + \text{NO}_3 \rightarrow \text{N}_2\text{O}_5$	f_3rd(2.0E-30,-4.4,1.4E-12,-0.7)
(R10)	T3-5	$\text{N}_2\text{O}_5 \rightarrow \text{NO}_3 + \text{NO}_2$	f_3rd(2.0E-30,-4.4,1.4E-12,-0.7) / (2.7E-27 * exp(11000.0/T))
(R11)	T3-2	$\text{HNO}_4 \rightarrow \text{HO}_2 + \text{NO}_2$	f_3rd(1.8E-31,-3.2,4.7E-12,-1.4) / (2.1E-27 * exp(10900.0/T))
(R12)	D1	$\text{CO} + \text{OH} \rightarrow \text{H}$	fca_3rd(1.5E-13,0.6,2.1E+9,6.1)
(R13)	D2	$\text{CH}_3 + \text{O}_2 \rightarrow \text{CH}_3\text{O}_2$	f_3rd(4.0E-31,-3.6,1.2E-12,1.1)
(R14)	F1	$\text{Cl} + \text{O}_2 \rightarrow \text{ClOO}$	f_3rd(2.2E-33,-3.1,1.8E-10,0.0)
(R15)	T3-14	$\text{ClOO} \rightarrow \text{Cl} + \text{O}_2$	f_3rd(2.2E-33,-3.1,1.8E-10,0.0) / (6.6E-25 * exp(2502.0/T))
(R16)	F4	$\text{Cl} + \text{NO}_2 \rightarrow \text{ClNO}_2$	f_3rd(1.8E-31,-2.0,1.0E-10,-1.0)
(R17)	F8	$\text{ClO} + \text{NO}_2 \rightarrow \text{ClONO}_2$	f_3rd(1.8E-31,-3.4,1.5E-11,-1.9)
(R18)	F10	$\text{ClO} + \text{ClO} \rightarrow \text{Cl}_2\text{O}_2$	f_3rd(1.6E-32,-4.5,2.0E-12,-2.4)
(R19)	T3-14	$\text{Cl}_2\text{O}_2 \rightarrow \text{ClO} + \text{ClO}$	f_3rd(1.6E-32,-4.5,2.0E-12,-2.4) / (9.3E-28 * exp(8835.0/T))
(R20)	G2	$\text{BrO} + \text{NO}_2 \rightarrow \text{BrONO}_2$	f_3rd(5.2E-31,-3.2,6.9E-12,-2.9)

*Table A.4: Heterogeneous reactions included in the model CHEM51.*

---

Reaction	
(R50)	$\text{BrONO}_2 + \text{H}_2\text{O}(\text{c}) \rightarrow \text{HOBr} + \text{HNO}_3$
(R51)	$\text{N}_2\text{O}_5 + \text{H}_2\text{O}(\text{c}) \rightarrow \text{HNO}_3 + \text{HNO}_3$
(R52)	$\text{ClONO}_2 + \text{H}_2\text{O}(\text{c}) \rightarrow \text{HNO}_3 + \text{HOCl}$
(R53)	$\text{ClONO}_2 + \text{HCl}(\text{c}) \rightarrow \text{Cl}_2 + \text{HNO}_3$
(R54)	$\text{HOCl} + \text{HCl}(\text{c}) \rightarrow \text{Cl}_2 + \text{H}_2\text{O}$
(R55)	$\text{N}_2\text{O}_5 + \text{HCl}(\text{c}) \rightarrow \text{HNO}_3 + \text{products}$
(R56)	$\text{HOBr} + \text{HCl}(\text{c}) \rightarrow \text{BrCl} + \text{H}_2\text{O}$
(R57)	$\text{ClONO}_2 + \text{HBr}(\text{c}) \rightarrow \text{BrCl} + \text{HNO}_3$
(R58)	$\text{HOCl} + \text{HBr}(\text{c}) \rightarrow \text{BrCl} + \text{H}_2\text{O}$
(R59)	$\text{BrONO}_2 + \text{HCl}(\text{c}) \rightarrow \text{BrCl} + \text{HNO}_3$

---



---

## Bibliography

---

- Baldwin, M. P. and T. J. Dunkerton**, Propagation of the arctic oscillation from the stratosphere to the troposphere, *Journal of Geophysical Research: Atmospheres*, *104*, (D24), 30937–30946, 1999.
- Baron, P. et al.**, Observation of horizontal winds in the middle-atmosphere between 30°S and 55°N during the northern winter 2009–2010, *Atmos. Chem. Phys.*, *13*, 6049–6064, 2013.
- Brasseur, G., M. H. Hitchman, S. Walters, M. Dymek, E. Falise and M. Pirre**, An interactive chemical dynamical radiative two-dimensional model of the middle atmosphere, *J. Geophys. Res.*, *95*, 5639–5655, 1995.
- Brunner, D., P. Siegmund, P. T. May, L. Chappel, C. Schiller, R. Müller, T. Peter, S. Fueglistaler, A. R. MacKenzie, A. Fixa, H. Schlager, G. Allen, A. M. Fjaeraa, M. Streibel and N. R. P. Harris**, The scout-o3 darwin aircraft campaign: rationale and meteorology, *Atmos. Chem. Phys.*, *9*, 93–117, 2009.
- Cairo, F., J. P. Pommereau, K. S. Law, H. Schlager, A. Garnier, F. Fierli, M. Ern, M. Streibel, S. Arabas, S. Borrmann, J. J. Berthelie, C. Blom, T. Christensen, F. D’Amato, G. D. Donfrancesco, T. Deshler, A. Diedhiou, G. Durry, O. Engelsen, F. Goutail, N. R. P. Harris, E. R. T. Kerstel, S. Khaykin, P. Konopka, A. Kylling, N. Larsen, T. Lebel, X. Liu, A. R. MacKenzie, J. Nielsen, A. Oulanowski, D. J. Parker, J. Pelon, J. Polcher, J. A. Pyle, F. Ravegnani, E. D. Rivière, A. D. Robinson, T. Röckmann,**

- C. Schiller, F. S. es, L. Stefanutti, F. Stroh, L. Some, P. Siegmund, N. Sitnikov, J. P. Vernier, C. M. Volk, C. Voigt, M. von Hobe, S. Viciani and V. Yushkov, An introduction to the scout-amma stratospheric aircraft, balloons and sondes campaign invest africa, august 2006: rationale and roadmap, *Atmos. Chem. Phys.*, 10, 2237–2256, 2010.
- Chao, W. C. and L. P. Chang, Development of a four-dimensional variational analysis system using the adjoint method at GLA Part I: Dynamics, *Month. Weath. Rev.*, 120, (8), 1661–1673, 1992.
- Daley, R., *Atmospheric data analysis*, 2, Cambridge university press, 1993.
- Dall’Amico, M., P. A. Stott, A. A. Scaife, L. J. Gray, K. H. Rosenlof and A. Y. Karpechko, Impact of stratospheric variability on tropospheric climate change, *Climate dynamics*, 34, (2-3), 399–417, 2010.
- Danielsen, M. F., A Dehydration Mechanism for the Stratosphere, *Geophys. Res. Lett.*, 9, (6), 605–608, 1982.
- Dee, D. P. and A. M. Da Silva, The choice of variable for atmospheric moisture analysis, *Monthly weather review*, 131, (1), 155–171, 2003.
- Denman, K. L. et al., Couplings Between Changes in the Climate System and Biogeochemistry, in *Climate Change 2007: The Physical Science Basis*, edited by S. D. Solomon et al., Cambridge Univ. Press, 2007.
- Dessler, A. E., *Chemistry and Physics of Stratospheric Ozone*, Academic Press, New York, 2000.
- Elbern, H., H. Schmidt, O. Talagrand and A. Ebel, 4D-variational data assimilation with an adjoint air quality model for emission analysis, *Environ. Model. and Software*, 15, 539–548, 2000.
- Elbern, H., J. Schwinger and R. Botchorishvili, Chemical state estimation for the middle atmosphere by four-dimensional variational data assimilation: System configuration, *J. Geophys. Res.*, 115, (D06302), 2010.
- Eskes, H., A. Segers and P. van Velthoven, Ozone forecasts of the stratospheric polar vortex-splitting event in September 2002, *J. Atmosph. Sci.*, 62, 812–821, 2004.
- Fischer, H. et al., MIPAS: An instrument for atmospheric and climate research, *Atmos. Chem. Phys.*, 8, 2151–2188, 2008.

- Fueglistaler, S., H. Wernli and T. Peter**, Tropical troposphere-to-stratosphere transport inferred from trajectory calculations, *J. Geophys. Res.*, *109*, (D3), 2004.
- Geer, A. J., C. Peubey, R. N. Bannister, R. Brugge, D. R. Jackson, W. A. Lahoz, S. Migliorini, A. O'Neill and R. Swinbank**, Assimilation of stratospheric ozone from MIPAS into a global general-circulation model: The September 2002 vortex split, *Q. J. R. Meteorol. Soc.*, *132*, 231–257, 2006.
- Gettelman, A. and P. M. de F. Forster**, A Climatology of the Tropical Tropopause Layer, *J. Meteor. Soc. Japan*, *80*, (4B), 911–924, 2002.
- Giering, R.**, *Tangent linear and Adjoint Model Compiler, Users manual TAMC Version 5.2*, September 1999.
- Giering, R. and T. Kaminski**, Recipes for adjoint code construction, *ACM Trans. Mathematical Software*, *24*, (4), 437–474, 1998.
- Grell, G. A., R. Knoche, S. E. Peckham and S. A. McKeen**, Online versus offline air quality modeling on cloud-resolving scales, *Geophysical Research Letters*, *31*, (16), 2004.
- Gropp, W., E. Lusk, N. Doss and A. Skjellum**, A high-performance, portable implementation of the MPI message passing interface standard, *Parallel Computing*, *22*, (6), 789–828, 1996.
- Hall, N. M. J. and P. Peyrillé**, Dynamics of the West African monsoon, *J. Phys. IV France*, *139*, 2006.
- Hascoët, L. and V. Pascual**, TAPENADE 2.1 user's guide, Technical Report 0300, Institut National de Recherche en Informatique et en Automatique, September 2004.
- Hoffmann, L. and M. Riese**, Quantitative transport studies based on trace gas assimilation, *Adv. Space Res.*, *33*, 1068–1072, 2004.
- Hoffmann, L., K. Weigel, R. Spang, S. Schroeder, K. Arndt, C. Lehmann, M. Kaufmann, M. Ern, P. Preusse, F. Stroh and M. Riese**, CRISTA-NF measurements of water vapor during the SCOUT-O3 Tropical Aircraft Campaign, *Advances in Space Research*, *43*, 74–81, 2009.

- Holton, J. R., P. H. Haynes, M. E. McIntyre, A. R. Douglass and R. B. R. L. Pfister, Stratosphere–Troposphere Exchange, *Rev. Geophys.*, *33*, 403–439, 1995.
- Jacobson, M. Z., Control of fossil-fuel particulate black carbon and organic matter, possibly the most effective method of slowing global warming, *Journal of Geophysical Research: Atmospheres*, *107*, (D19), 2002.
- Janicot, S., C. D. Thorncroft, A. Ali, N. Asencio, G. J. Berry, O. Bock, B. Bourlés, G. Caniaux, F. Chauvin, A. Deme, L. Ker-goat, J.-P. Lafore, C. Lavaysse, T. Lebel, B. Marticoréna, F. Mounier, P. Nédélec, J.-L. Redelsperger, F. Ravegnani, C. E. Reeves, R. Roca, P. D. Rosnay, H. Schlager, B. Sultan, M. Tomasi-ni and A. Ulanovsky, Large-scale overview of the summer monsoon over West Africa during the AMMA field experiment in 2006, *Ann. Geophys.*, *26*, 2008.
- Kalnay, E., *Atmospheric Modeling, Data Assimilation and Predictability*, Cambridge Univ. Press, 2003.
- Keenan, T. D. and R. E. Carbone, A preliminary morphology of precipitation systems in tropical northern australia, *J. Roy. Meteor. Soc.*, *118*, 283–326, 1992.
- Lahoz, W. and Q. Errera, Constituent assimilation, in *Data Assimilation*, 449–490, Springer, 2010.
- Lahoz, W. A., Q. Errera, R. Swinbank and D. Fonteyn, Data assimilation of stratospheric constituents: a review, *Atmos. Chem. Phys.*, *7*, 5745–5773, 2007.
- Lawrence, M. G., Ø. Hov, M. Beekmann, J. Brandt, H. Elbern, H. Eskes, H. Feichter and M. Takigawa, The chemical weather, *Environmental Chemistry*, *2*, (1), 6–8, 2005.
- Lohmann, U. and J. Feichter, Global indirect aerosol effects: A review, *Atmos. Chem. Phys.*, *5*, 715–737, 2005.
- Mahlman, J., Dynamics of transport processes in the upper troposphere, *Science*, *276*, (5315), 1079–1083, 1997.
- Majewski, D., D. Liermann, P. Prohl, B. Ritter, M. Buchhold, T. Hanisch, G. Paul, W. Wergen and J. Baumgardner, The operational global icosahedral-hexagonal gridpoint model GME: Description and high-resolution tests, *Month. Weath. Rev.*, *130*, 319–338, 2001a.

- Majewski, D., A. Müller and B. Ritter**, *Kurze Beschreibung des Global-Modells GME und seiner Datenbanken auf dem Datenserver (DAS) des DWD*, Deutscher Wetterdienst, 2001b.
- McMichael, A. J. and R. E. Woodruff**, *Climate change and human health*, Springer, 2005.
- McRae, G. J., W. R. Goodin and J. H. Seinfeld**, Numerical solution of the atmospheric diffusion equation for chemically reacting flows, *J. Comp. Phys.*, 45, 1–42, 1982.
- Murcray, D. G., T. G. Kyle, F. H. Murcray and W. J. Williams**, Nitric Acid and Nitric Oxide in the Lower Stratosphere, *Nature*, 218, (78), 1968.
- Nathaniel, J. et al.**, MLS Version 1.5 Level 2 data quality and description document, Jpl publication, Jet Propulsion Laboratory, Juli 2005.
- Nazaryan, H., M. P. McCormick and J. M. Russel III**, New studies of SAGE II and HALOE ozone profile and long-term change comparisons, *J. Geophys. Res.*, 110, (D09305), 2005.
- Offermann, D., K.-U. Grossmann, P. Barthol, P. Knieling, M. Riese and R. Trant**, Cryogenic infrared spectrometers and telescopes for the atmosphere (CRISTA) experiment and middle atmosphere variability, *J. Geophys. Res.*, 104, (D13), 16,311–16,325, 1999.
- Okonkwo, C., B. Demoz and S. Tesfai**, Characterization of West African Jet Streams and Their Association to ENSO Events and Rainfall in ERA-Interim 1979–2011, *Advances in Meteorology.*, 2014, 2014.
- Persson, A.**, User guide to ecmwf forecast products, ECMWF, European Centre for Medium-range Weather Forecasts, 2001.
- Pichler, H.**, *Dynamik der Atmosphäre*, Spektrum, 3. Auflage, 1997.
- Ramanathan, V. and Y. Feng**, Air pollution, greenhouse gases and climate change: Global and regional perspectives, *Atmospheric Environment*, 43, (1), 37–50, 2009.
- Randel, W. J. and E. J. Jensen**, Physical processes in the tropical tropopause layer and their roles in a changing climate, *Nature Geoscience*, 6, (3), 169–176, 2013.

- Riese, M., F. Ploeger, A. Rap, B. Vogel, P. Konopka, M. Dameris and P. Forster, Impact of uncertainties in atmospheric mixing on simulated utls composition and related radiative effects, *Journal of Geophysical Research: Atmospheres*, 117, (D16), 2012.
- Riese, M., H. Oelhaf, P. Preusse, J. Blank, M. Ern, F. Friedl-Vallon, H. Fischer, T. Guggenmoser, M. Höpfner, P. Hoor et al., Gimballed limb observer for radiance imaging of the atmosphere (gloria) scientific objectives, *Atmospheric measurement techniques*, 7, (7), 1915–1928, 2014.
- Riishøjgaard, L. P., A direct way of specifying flow-dependent background error correlations for meteorological analysis systems, *Tellus*, 50A, 42–57, 1998.
- Rosenfeld, D., Suppression of rain and snow by urban and industrial air pollution, *Science*, 287, (5459), 1793–1796, 2000.
- Sander, S. P. et al., Chemical kinetics and photochemical data for use in atmospheric studies, JPL Publication 02-25, Jet Propulsion Laboratory, Februar 2003.
- Sander, S. P., J. Abbatt, J. R. Barker, J. B. Burkholder, R. R. Friedl, D. M. Golden, R. E. Huie, C. E. Kolb, M. J. Kurylo, G. K. Moortgat, V. L. Orkin and P. H. Wine, Chemical kinetics and photochemical data for use in atmospheric studies, Evaluation No. 17, JPL Publication 10-6, Jet Propulsion Laboratory, Juni 2011.
- Sandu, A., D. N. Daescu and G. R. Carmichael, Direct and adjoint sensitivity analysis of chemical kinetic systems with KPP: Part I – Theory and software tools, *Atmos. Environ.*, 37, 5083–5096, 2003.
- Sandu, A., W. Liao, G. R. Carmichael, D. K. Henze and J. H. Seinfeld, Inverse modeling of aerosol dynamics using adjoints: Theoretical and numerical considerations, *Aerosol Sci. Technol.*, 39, (8), 677–694, 2005.
- Schroeder, S. E., A. Kullmann, P. Preusse, F. Stroh, K. Weigel, M. Ern, P. Knieling, F. Olschewski, R. Spang and M. Riese, Radiance calibration of CRISTA-NF, *Advances in Space Research.*, 43, 1910–1917, 2009.
- Schwinger, J., *Four-Dimensional Variational Data Assimilation for Estimation of the Atmospheric Chemical State from the Tropopause to the Lower Mesosphere*, Ph.D. Thesis, Institut für Geophysik und Meteorologie der Universität zu Köln, 2006.

- Seinfeld, J. H. and S. N. Pandis**, *Atmospheric chemistry and physics: from air pollution to climate change*, Wiley-Interscience, 2006.
- Simmons, A. J. and D. M. Burridge**, An energy and angular-momentum conserving vertical finite-difference scheme and hybrid vertical coordinates, *Month. Weath. Rev.*, *109*, 758–766, 1981.
- Solomon, S.**, The mystery of the antarctic ozone hole, *Reviews of Geophysics*, *26*, (1), 131–148, 1988.
- Stefanutti, L., L. Sokolov, S. Balestri, A. R. MacKenzie and V. Khatatov**, The M-55 Geophysica as a Platform for the Air-borne Polar Experiment, *J. Atmos. Ocean. Tech.*, *16*, 1999.
- Talagrand, O.**, Assimilation of observations, an introduction, *J. Meteor. Soc. Japan*, *75*, (1B), 191–209, 1997.
- Talagrand, O.**, A posteriori evaluation and verification of analysis and assimilation algorithms, in *Proceedings of the Workshop on Diagnosis of Data Assimilation Systems*, European Centre for Medium-range Weather Forecasts Reading, England, 2-4 November, 1998.
- Talagrand, O. and P. Courtier**, Variational assimilation of meteorological observations with the adjoint vorticity equation. I: Theory, *Q. J. R. Meteorol. Soc.*, *113*, 1311–1328, 1987.
- Thompson, D. W. and S. Solomon**, Interpretation of recent southern hemisphere climate change, *Science*, *296*, (5569), 895–899, 2002.
- Toon, O. B., P. Hamill, R. P. Turco and J. Pinto**, Condensation of HNO<sub>3</sub> and HCl in the winter polar stratospheres, *Geophys. Res. Lett.*, *13*, 1284–1287, 1986.
- Verwer, J. G., E. J. Spee, J. G. Blom and W. Hundsdorfer**, A second order rosenbrock method applied to photochemical dispersion problems, Technical Report MAS R9717, Centrum voor Wiskunde en Informatica, 1997.
- von Clarmann, T., M. Höpfner, S. Kellmann, A. Linden, S. Chauhan, B. Funke, U. Grabowski, N. Glatthor, M. Kiefer, T. Schieferdecker, G. P. Stiller and S. Versick**, Retrieval of temperature, H<sub>2</sub>O, O<sub>3</sub>, HNO<sub>3</sub>, CH<sub>4</sub>, N<sub>2</sub>O, ClONO<sub>2</sub> and ClO from MIPAS reduced resolution nominal mode limb emission measurements, *Atmos. Meas. Tech.*, *2*, 159–175, 2009.

- Waters, J. W. et al.**, An Overview of the EOS MLS Experiment, *California Institute of Technology*, 1437–1455, 2004.
- Weaver, A. and P. Courtier**, Correlation modelling on the sphere using a generalized diffusion equation, *Q. J. R. Meteorol. Soc.*, *127*, 1815–1846, 2001.
- Weigel, K.**, *Infrared limb-emission observations of the upper troposphere, lower stratosphere with high spatial resolution*, Ph.D. Thesis, Faculty of Mathematics and Natural Sciences, University of Wuppertal, 2006.
- Weigel, K., M. Riese, L. Hoffmann, S. Hofer, C. Kalicinsky, P. Knieling, F. Olschewski, P. Preusse, R. Spang, F. Stroh and C. M. Volk**, CRISTA-NF measurements during the AMMA-SCOUT-O3 aircraft campaign, *Atmos. Meas. Tech.*, *3*, 1437–1455, 2010.
- World Meteorological Organization**, Scientific assessment of ozone depletion: 2006, technical report, WMO, 2006.
- Zängl, G.**, ICON: The Icosahedral Nonhydrostatic Modelling Framework of DWD and MPI-M, in *Seminar on Numerical Methods for Atmosphere and Ocean Modelling*, ECMWF, European Centre for Medium-range Weather Forecasts, 2013.

---

## Acknowledgements

---

I would like to express my special appreciation and thanks to my supervisor PD Dr. Hendrik Elbern, you have been a tremendous mentor for me from my very first steps in Germany and in science. I would like to thank you for encouraging my research and for allowing me to grow as a research scientist. I acknowledge the essential meliorations of this manuscript by your proof-reading.

I kindly thank Prof. Dr. Andreas Wahner for agreeing to act as a referee for this thesis.

I am especially grateful to Dr. Jörg Schwinger for being always available for questions and for helping me through the jungle of SACADA.

Considerable computational resources have been used to accomplish this work and I want to thank those, who provided and maintained them. A part of the case studies has been computed at the ZAIK/RRZK cluster Clio. I gratefully acknowledge the computing time granted by the John von Neumann Institute for Computing (NIC) and provided on the supercomputer JUROPA at Jülich Supercomputing Centre (JSC).

This work would not have been possible without support from a number of groups, persons and institutions. I want to thank Dr. Katja Weigel, Dr. Lars Hoffmann and Dr. Reinhold Spang for providing the CRISTA-NF retrievals for this study. MLS profiles have been obtained from the NASA's California Institute of Technology. MIPAS retrievals were provided by T. von Clarmann and the IMK-group at Forschungszentrum Karlsruhe. The HALOE trace gas profiles have been supplied by Hampton University, Virginia and the NASA Langley Research Center.

The AMMA-SCOUT-O3 measurement campaign was facilitated by the European Commission and the EC Integrated Project SCOUT-O3 (505390-GOCE-CT-2004) and AMMA. Based on a French initiative, AMMA was built by an international scientific group and is currently funded by a large number of agencies, especially from France, the United Kingdom, the United States, and Africa. It has been the beneficiary of a major financial contribution from the European Communities Sixth Framework Research Program.

I owe special thanks to Anne Caroline Lange, Johannes Klimpt, Tamari Janelidze, Philipp Franke, Dr. Zoi Paschalidi, Dr. Luise Fröhlich and Dr. Isabel Ribeiro for their offer to contribute in ameliorating this manuscript by their comments, suggestions and translating skills.

I would like to thank especially my past and present colleagues in RIU. Thanks to Prof. Dr. A. Ebel and his wife Barbara for their wonderful events, where I was allowed to present with my family. Many thanks to Dr. Michael Memmesheimer for his care and support. Thanks to everyone being “halb eins in der Mensa”, where I was able to learn German with fun.

I would like to express my gratitude to Prof. Ramaz Botchorishvili and his wonderful wife Nana for their trust and showing me the way how to apply for PhD position in Germany.

I also want to thank Prof. Dr. Alfons Goris and his amazing wife Brigitte for beautiful Christmas Eves in their family.

My very special thanks go to my dearest friends Nadine Goris, Dr. Tamara Gigolashvili and Manana Geliashvili Gust for their emotional support.

I want to thank my parents Manana Getashvili and Ivane Kasradze for their support during all the years.

Finally, I want to thank my husband, Vakhtang Shaverdashvili, who has believed in me, supporting me and for being a wonderful father for our children, Mariam and Martha.

## Erklärung

Ich versichere, dass ich die von mir vorgelegte Dissertation selbständig angefertigt, die benutzten Quellen und Hilfsmittel vollständig angegeben und die Stellen der Arbeit –einschließlich Tabellen, Karten und Abbildungen–, die anderen Werken im Wortlaut oder dem Sinn nach entnommen sind, in jedem Einzelfall als Entlehnung kenntlich gemacht habe; dass diese Dissertation noch keiner anderen Fakultät oder Universität zur Prüfung vorgelegen hat; dass sie –abgesehen von unten angegebenen Teilpublikationen– noch nicht veröffentlicht worden ist sowie, dass ich eine solche Veröffentlichung vor Abschluss des Promotionsverfahrens nicht vornehmen werde. Die Bestimmungen der Promotionsordnung sind mir bekannt. Die von mir vorgelegte Dissertation ist von PD. Dr. H. Elbern betreut worden.

### Teilpublikationen:

**H. Elbern, A. Strunk, L. Nieradzik, N. Goris, J. Schwinger, K. Kasradze**, IMACCO: Virtual Institute for Inverse Modelling of the Atmospheric Chemical Composition, *Proceeding of the 5th John-von-Neuman Institute for Computing Symposium*, Jülich, 24.-25.02.2010, ed: / G. Münster, D. Wolf, M. Kremer (2010). - S. 297 - 304 (2010)